

---

OBSERVABILITY OF SUDDEN AEROSOL INJECTIONS  
BY ENSEMBLE-BASED FOUR-DIMENSIONAL  
ASSIMILATION  
OF REMOTE SENSING DATA

---

I N A U G U R A L – D I S S E R T A T I O N  
ZUR  
ERLANGUNG DES DOKTORGRADES  
DER MATHEMATISCH–NATURWISSENSCHAFTLICHEN FAKULTÄT  
DER UNIVERSITÄT ZU KÖLN

vorgelegt von

Anne Caroline Lange

aus Aachen

JÜLICH, 2018

Berichterstatter: PD Dr. Hendrik Elbern  
Prof. Dr. Yaping Shao

Tag der mündlichen Prüfung: 02.03.2018

*Die theoretische Vernunft erkennt, „was da ist“,  
die praktische Vernunft hingegen erschließt, „was da sein soll“.*

nach Immanuel Kant [1724–1804]



# Abstract

For sudden, often hazardous aerosol injections such as volcanic eruptions, wild fires, and mineral dust uplifts, uncertainties of emission source parameters impose the characterizing impediment for skillful numerical simulations. Large amounts of accidentally emitted aerosols can infer serious impacts on health, climate, environment, and economy. This highlights the societal need for reliable forecasts of released particulate matter. Data assimilation and inverse modeling methods incorporate the knowledge gained from both numerical modeling and observations. Applying spatio-temporal assimilation techniques, the combination of the atmospheric dynamics with observations induces constraints with potentially advantageous effects on the simulations. Furthermore, ensemble-based analyses provide valuable information about the skill of the forecast results. However, predictions remain uncertain in regions, where observational information is restricted. Confining factors are manifold and include the inaccessibility of observational infrastructure, limitations of measurement configurations or retrieval feasibility, as well as obstructing meteorological conditions, such as clouds, which may strongly restrict remote sensing of aerosols. The research field of observability investigates the impact of utilized observations, thus focusing on observation network optimization and information quantity specification.

Taking the most challenging case of volcanic eruption as prototype example for sudden aerosol injections, the research described in this thesis develops and investigates new methodologies to assess the impact of observations on the analysis. The emphasis is placed on assimilation-based analyses applying both initial value and emission factor optimization for volcanic ash dispersion predictions. As observational input, two entirely different satellite-borne remote sensing principles are exploited: firstly, vertically integrated SEVIRI (Spinning Enhanced Visible and Infrared Imager) volcanic ash column mass loadings and secondly, vertically resolved CALIOP (Cloud-Aerosol Lidar with Orthogonal Polarization) particle extinction coefficient profiles. For the assimilation within the EURAD-IM (European Air pollution Dispersion-Inverse Model) system, appropriate observation operators and their adjoint realizations are constructed. The basic theoretical principles of observability in case of volcanic ash column mass loading observations are deduced from the viewpoint of the Kolmogorov-Sinai entropy. The practical analyses are presented for the Eyjafjallajökull eruption event in April 2010. Ensemble versions of both the four dimensional variational (4D-var) data assimilation technique and the particle smoother approach are implemented and processed, able to identify regions of high and low uncertainty in the dispersion simulation results. The analyses reveal a considerable constraining impact of SEVIRI

retrievals to the ash dispersion, while CALIOP retrievals append information only on a very local scale. It is not possible to make a statement on the difference of the resulting quality of the various ensemble simulations due to the following reasons: firstly, the differences of the assimilation approaches of 4D-var and particle smoother algorithms and secondly, the evaluation of the single Eyjafjallajökull scenario only. The variable degree of reliability is shown as a consequence of cloud cover dependent observability from space for both quasi-continuous SEVIRI data and sparse CALIOP overpasses.

# Kurzzusammenfassung

Im Falle unerwarteter und häufig auch gefährlicher Aerosolemissionen wie beispielsweise Vulkanausbrüche, Waldbrände und Mineralstaubaufwirbelungen führen deren unsichere Quellparameterabschätzungen zu charakteristischen Schwierigkeiten bei der Erstellung geeigneter numerischer Simulationen. Große Mengen plötzlich emittierter Aerosole können ernsthafte Folgen für Gesundheit, Klima, Umwelt und Wirtschaft nach sich ziehen. Daraus ergibt sich die gesellschaftliche Notwendigkeit, verlässliche Ausbreitungsvorhersagen von freigesetzten Partikelansammlungen in der Atmosphäre bereitzustellen. Methoden der Datenassimilation und inversen Modellierung verbinden die Erkenntnisse, die sowohl aus numerischer Modellierung als auch aus Beobachtungen gewonnen werden. Die Anwendung raum-zeitlicher Assimilationstechniken nutzt die Verbindung von atmosphärischer Dynamik mit unterschiedlichsten Beobachtungen. Daraus können sich Korrekturen ergeben, die potentiell vorteilhafte Effekte auf die Simulationen verursachen. Darüber hinaus erbringen ensemblebasierte Analysen wertvolle Informationen über die Güte der Vorhersageergebnisse. Diese Prognosen bleiben jedoch unsicher für Regionen, in denen Beobachtungsinformationen eingeschränkt verfügbar sind. Begrenzende Faktoren gibt es viele. Zum Beispiel: Unzugänglichkeiten für Beobachtungsinfrastrukturen, Einschränkungen bei Messkonfigurationen oder eingeschränkte Retrievalumsetzbarkeiten sowie störende meteorologische Bedingungen. Zu letzteren zählen insbesondere Wolken, die Fernerkundungsbeobachtungen von Aerosolen stark behindern. Das Forschungsgebiet der Beobachtbarkeit untersucht den Einfluss von Beobachtungen und konzentriert sich dabei auf die Optimierung von Beobachtungsnetzwerken und auf die Ermittlung des zugehörigen Informationsumfangs.

In Anwendung einer vulkanischen Eruption als besonders anspruchsvoller Prototyp für plötzliche Aerosolereignisse entwickelt und untersucht die in dieser Arbeit beschriebene Forschung neue Methodiken, den Einfluss von Beobachtungen auf die Analyse zu bewerten. Dabei liegt der Schwerpunkt auf assimilationsbasierten Analysen unter Verwendung von Anfangswert- und Emissionsfaktoroptimierung für Vulkanasche-Ausbreitungsvorhersagen. Als Beobachtungs-Dateneingabe werden zwei völlig verschiedene Satelliten gestützte Fernerkundungsprinzipien genutzt: einerseits vertikal integrierte SEVIRI (Spinning Enhanced Visible and Infrared Imager) Vulkanaschemassen in einer definierten Säule, andererseits vertikal aufgelöste CALIOP (Cloud-Aerosol Lidar with Orthogonal Polarization) Partikelextinktionskoeffizientenprofile. Für die Assimilation im EURAD-IM-System (European Air pollution Dispersion-Inverse Model) werden entsprechende Beobachtungsoperatoren und deren

adjungierte Versionen entwickelt. Die theoretischen Grundsätze der Beobachtbarkeit im Falle von Beobachtungen von Vulkanasche-Massesäulen sind aus der Perspektive der Kolmogorov-Sinai-Entropie abgeleitet. Die praktischen Analysen werden für das Eyjafjallajökull-Ausbruchereignis im April 2010 aufgezeigt. Ensembleversionen einerseits mit vier-dimensionaler variationeller (4D-var) Datenassimilationstechnik und andererseits mit „particle smoother“-Ansatz werden implementiert und ausgeführt. Durch die Simulationsergebnisse lassen sich Regionen identifizieren, die hohe bzw. niedrige Unsicherheiten der Partikelausbreitung aufzeigen. Die vorgenommenen Analysen weisen eine deutlich beschränkende Wirkung der SEVIRI-Retrieval auf die Ascheausbreitung auf, während die CALIOP-Retrieval gewisse Informationen auf sehr lokalen Skalen beitragen. Wegen der unterschiedlichen Assimilationsansätze von 4D-var gegenüber „particle smoother“-Algorithmen kann auf Basis des einzigen Eyjafjallajökull-Szenarios keine Aussage über die Unterschiede der Ergebnisqualität von den Ensemblesimulationen getroffen werden. Der variable Grad der Verlässlichkeit resultiert aus der bewölkungsabhängigen Beobachtbarkeit aus dem Weltall sowohl seitens der quasi-kontinuierlichen SEVIRI-Daten als auch der vereinzelt CALIOP-Überflüge.

# Contents

Abstract	v
Kurzzusammenfassung	vii
List of Figures	xi
List of Tables	xv
Acronyms	xvii
<b>1 Introduction</b>	<b>1</b>
<b>2 Observability of sudden aerosol injections</b>	<b>7</b>
2.1 Observability . . . . .	7
2.1.1 Observability in atmospheric applications . . . . .	8
2.1.2 Analyzing observability . . . . .	10
2.2 Monitoring aerosols . . . . .	15
2.3 Special aerosol events . . . . .	18
<b>3 Data Assimilation</b>	<b>21</b>
3.1 Four dimensional variational data assimilation . . . . .	21
3.2 Ensemble data assimilation via particle smoother . . . . .	24
<b>4 Observations</b>	<b>27</b>
4.1 SEVIRI . . . . .	27
4.1.1 Instrumentation and measurement configuration . . . . .	27
4.1.2 Volcanic ash mass loading retrieval . . . . .	29
4.1.3 Advantages and disadvantages . . . . .	31
4.2 CALIOP . . . . .	32
4.2.1 Instrumentation and measurement configuration . . . . .	32
4.2.2 Aerosol extinction coefficient retrieval . . . . .	34
4.2.3 Advantages and disadvantages . . . . .	36
<b>5 Modelling system</b>	<b>39</b>
5.1 EURAD-IM . . . . .	39
5.2 ESIAS-Chem . . . . .	43

---

<b>6</b>	<b>Developments</b>	<b>45</b>
6.1	Model domain . . . . .	45
6.2	The SEVIRI observation operator . . . . .	46
6.3	The CALIOP observation operator . . . . .	47
6.4	Observability analysis with ESIAS . . . . .	49
<b>7</b>	<b>Observability Analyses</b>	<b>51</b>
7.1	General experiment setup . . . . .	52
7.1.1	Aerosol scenario . . . . .	52
7.1.2	Meteorological conditions . . . . .	53
7.1.3	Ensemble generation . . . . .	55
7.1.4	Error assessment . . . . .	57
7.2	4D-var ensemble using SEVIRI retrievals . . . . .	58
7.3	4D-var ensemble using SEVIRI and CALIOP retrievals . . . . .	68
7.4	ESIAS-chem ensemble using SEVIRI retrievals . . . . .	75
<b>8</b>	<b>Conclusion and Outlook</b>	<b>83</b>
	<b>General Acknowledgments</b>	<b>87</b>
<b>A</b>	<b>Appendix</b>	<b>89</b>
A.1	Supplements to the 4D-var ensemble analysis using SEVIRI retrievals	89
A.2	Supplements to the 4D-var ensemble analysis using SEVIRI and CALIOP retrievals . . . . .	93
A.3	Supplements to the ESIAS-chem ensemble analysis using SEVIRI retrievals . . . . .	98
	<b>Bibliography</b>	<b>99</b>
	<b>Personal Acknowledgments</b>	<b>117</b>

# List of Figures

2.1	Illustration of the Kolmogorov-Sinai entropy . . . . .	11
4.1	Artist's view of Meteosat Second Generation in space . . . . .	28
4.2	MSG-SEVIRI's total field of view and area of retrieved volcanic ash data set . . . . .	31
4.3	Artist's view of CALIPSO in space . . . . .	33
5.1	Flow chart of the EURAD-IM model system . . . . .	40
6.1	Model domain and vertical grid resolution . . . . .	46
7.1	Explosive eruption of the Eyjafjallajökull on 16 April 2010 . . . . .	52
7.2	Meteorological situation in Europe during the Eyjafjallajökull eruption	53
7.3	Cloud cover above Europe during the Eyjafjallajökull eruption illustrated by MODIS natural color images from 14–17 April 2010 . . . . .	54
7.4	Volcanic ash emission profiles of the 4D-var ensemble . . . . .	56
7.5	MSG-SEVIRI volcanic ash column mass loading retrievals of the Eyjafjallajökull 2010 ash plume on 15–17 April . . . . .	58
7.6	Comparison of PM <sub>10</sub> time series of the 4D-var ensemble first guesses and analyses (based on SEVIRI data) with independent observations at Schneefernerhaus on 17 April 2010 . . . . .	59
7.7	Horizontal volcanic ash distribution above Europe on 16 April at 13 UTC, as retrieved from SEVIRI observations, EM-1 background field, EM-1 analysis field applying 4D-var assimilation of SEVIRI data, and the analysis increment . . . . .	60
7.8	Vertical volcanic ash distribution over Leipzig on 16 April at 13 UTC: Concentration profiles of the background and analysis fields (based on SEVIRI data) of the 4D-var ensemble, as well as the lidar retrieved mean backscatter coefficient profiles of the Leipzig EARLINET station	62
7.9	Volcanic ash column mass loadings at the EARLINET station in Leipzig on 16 April at 13 UTC: background and analysis (based on SEVIRI data) of the 4D-var ensemble, the analysis ensemble mean, SEVIRI pixels and their mean, and lidar derived mass loading equivalent	63
7.10	Iterative evolution of normalized cost function for the nine members of the 4D-var ensemble, based on the assimilation of SEVIRI data . . . . .	64

7.11	Spaghetti plots of $1.0 \text{ g m}^{-2}$ mass isopleths for all nine 4D-var ensemble members: first guess and analysis (based on SEVIRI data) are depicted on 15 April at 12 UTC, 16 April at 12 UTC, and 17 April at 04 UTC .	65
7.12	Spaghetti plots of $0.2 \text{ mg m}^{-3}$ and $2.0 \text{ mg m}^{-3}$ volcanic ash concentration isopleths as vertical cross section for all nine 4D-var ensemble members: first guess and analysis (based on SEVIRI data) on 16 April at 12 UTC . . . . .	67
7.13	CALIPSO ground tracks of all available overpasses in the model domain on 15–17 April . . . . .	69
7.14	Comparison of $\text{PM}_{10}$ time series of the 4D-var ensemble first guesses and analyses (based on SEVIRI and CALIOP data) with independent observations at Schneefernerhaus on 17 April 2010 . . . . .	69
7.15	Horizontal volcanic ash distribution above Europe on 16 April at 13 UTC: EM-1 background field, EM-1 analysis field applying 4D-var assimilation of SEVIRI and CALIOP data, and the analysis increment	70
7.16	Vertical volcanic ash distribution over Leipzig on 16 April at 13 UTC: Concentration profiles of the analysis shown in Figure 7.8 and of the analysis applying combined SEVIRI and CALIOP retrievals, as well as the mass equivalent derived from the lidar profile of the Leipzig EARLINET station . . . . .	71
7.17	Volcanic ash column mass loadings at the EARLINET station in Leipzig on 16 April at 13 UTC: analysis ensemble mean (based on SEVIRI data), analysis ensemble mean (based on SEVIRI and CALIOP data), SEVIRI observation mean, and lidar derived mass loading equivalent . . . . .	71
7.18	Spaghetti plots of $1.0 \text{ g m}^{-2}$ mass isopleths for all nine 4D-var ensemble members: first guess and analysis (based on SEVIRI and CALIOP data) are depicted on 15 April at 12 UTC, 16 April at 12 UTC, and 17 April at 04 UTC . . . . .	73
7.19	Comparison of assimilated CALIOP particle extinction retrievals with spaghetti plots of $0.2 \text{ mg m}^{-3}$ volcanic ash concentration isopleths as vertical cross section along the 16 April 01:20 UTC CALIPSO overpass. The mass isopleths are depicted for the first guess, the analysis (based on SEVIRI data), and the analysis (based on SEVIRI and CALIOP data) on 16 April at 01 UTC . . . . .	74
7.20	Spaghetti plots of $1.0 \text{ g m}^{-2}$ volcanic ash column mass loadings for the PS ensemble analysis with 60 ensemble members on 15 April at 12 UTC, 16 April at 12 UTC, and 17 April at 04 UTC . . . . .	76
7.21	MSG-SEVIRI volcanic ash column mass loading retrievals on 16 April at 00 UTC . . . . .	77
7.22	Spaghetti plots of $1.0 \text{ g m}^{-2}$ volcanic ash column mass loadings of with 60 ensemble members on 16 April at 00 UTC: the PS ensemble analysis based on the assimilation of all available SEVIRI data and SEVIRI retrievals higher than $0.45 \text{ g m}^{-2}$ . . . . .	78

7.23	Ensemble mean and ensemble spread for the PS ensemble analyses SEVIRI-1 and SEVIRI-2 on 16 April at 00 UTC . . . . .	78
7.24	Comparison of PM <sub>10</sub> observations with the PS ensemble analysis SEVIRI-2 of volcanic ash concentrations at Schneefernerhaus on 17 April 2010 . . . . .	79
7.25	Analyzed volcanic ash emission profiles of PS ensemble member 30 between 14 April at 06 UTC to 15 April at 12 UTC . . . . .	80
A.1	Horizontal ash distribution above Europe on 16 April at 13 UTC as displayed in Figure 7.7 but for EM-2 (analysis based on SEVIRI data)	89
A.2	Horizontal ash distribution above Europe on 16 April at 13 UTC as displayed in Figure 7.7 but for EM-3 (analysis based on SEVIRI data)	90
A.3	Horizontal ash distribution above Europe on 16 April at 13 UTC as displayed in Figure 7.7 but for EM-4 (analysis based on SEVIRI data)	90
A.4	Horizontal ash distribution above Europe on 16 April at 13 UTC as displayed in Figure 7.7 but for EM-5 (analysis based on SEVIRI data)	91
A.5	Horizontal ash distribution above Europe on 16 April at 13 UTC as displayed in Figure 7.7 but for EM-6 (analysis based on SEVIRI data)	91
A.6	Horizontal ash distribution above Europe on 16 April at 13 UTC as displayed in Figure 7.7 but for EM-7 (analysis based on SEVIRI data)	92
A.7	Horizontal ash distribution above Europe on 16 April at 13 UTC as displayed in Figure 7.7 but for EM-8 (analysis based on SEVIRI data)	92
A.8	Horizontal ash distribution above Europe on 16 April at 13 UTC as displayed in Figure 7.7 but for EM-9 (analysis based on SEVIRI data)	93
A.9	Horizontal ash distribution above Europe on 16 April at 13 UTC as displayed in Figure 7.15 but for EM-2 (analysis based on SEVIRI and CALIOP data) . . . . .	93
A.10	Horizontal ash distribution above Europe on 16 April at 13 UTC as displayed in Figure 7.15 but for EM-3 (analysis based on SEVIRI and CALIOP data) . . . . .	94
A.11	Horizontal ash distribution above Europe on 16 April at 13 UTC as displayed in Figure 7.15 but for EM-4 (analysis based on SEVIRI and CALIOP data) . . . . .	94
A.12	Horizontal ash distribution above Europe on 16 April at 13 UTC as displayed in Figure 7.15 but for EM-5 (analysis based on SEVIRI and CALIOP data) . . . . .	94
A.13	Horizontal ash distribution above Europe on 16 April at 13 UTC as displayed in Figure 7.15 but for EM-6 (analysis based on SEVIRI and CALIOP data) . . . . .	95
A.14	Horizontal ash distribution above Europe on 16 April at 13 UTC as displayed in Figure 7.15 but for EM-7 (analysis based on SEVIRI and CALIOP data) . . . . .	95
A.15	Horizontal ash distribution above Europe on 16 April at 13 UTC as displayed in Figure 7.15 but for EM-8 (analysis based on SEVIRI and CALIOP data) . . . . .	95

---

A.16 Horizontal ash distribution above Europe on 16 April at 13 UTC as displayed in Figure 7.15 but for EM-9 (analysis based on SEVIRI and CALIOP data) . . . . .	96
A.17 Iterative evolution of normalized cost function for the nine members of the 4D-var ensemble, based on the assimilation of SEVIRI and CALIOP data . . . . .	96
A.18 Spaghetti plots of $0.2 \text{ mg m}^{-3}$ and $2.0 \text{ mg m}^{-3}$ volcanic ash concentration isopleths as vertical cross section for all nine 4D-var ensemble members: first guess and analysis (based on SEVIRI and CALIOP data) on 16 April at 12 UTC . . . . .	97
A.19 Spaghetti plots of $1.0 \text{ g m}^{-2}$ volcanic ash column mass loadings for the PS ensemble analysis SEVIRI-2 with 60 ensemble members on 15 April at 12 UTC, 16 April at 12 UTC, and 17 April at 04 UTC . . . .	98
A.20 Comparison of $\text{PM}_{10}$ observations with the PS ensemble analysis SEVIRI-1 of volcanic ash concentrations at Schneefernerhaus on 17 April 2010 . . . . .	98

# List of Tables

4.1	Characteristics of SEVIRI's spectral channels . . . . .	28
5.1	Trimodal log-normal representation in MADE . . . . .	42



# Acronyms

<b>AOD</b>	Aerosol Optical Depth
<b>ARW</b>	Advanced Research WRF
<b>A-train</b>	Afternoon Train
<b>BLUE</b>	Best Linear Unbiased Estimation
<b>CALIOP</b>	Cloud-Aerosol Lidar with Orthogonal Polarization
<b>CALIPSO</b>	Cloud-Aerosol Lidar and Infrared Pathfinder Satellite Observation
<b>CATS</b>	Cloud-Aerosol Transport System
<b>CCN</b>	Cloud Condensation Nuclei
<b>CNES</b>	Centre National d'Études Spatiales
<b>CTM</b>	Chemistry Transport Model
<b>EARLINET</b>	European Aerosol Research Lidar Network
<b>EarthCARE</b>	Earth Clouds, Aerosols and Radiation Explorer
<b>ECMWF</b>	European Centre for Medium-Range Weather Forecasts
<b>EEM</b>	EURAD Emission Model
<b>EM</b>	Ensemble Member
<b>EMEP</b>	European Monitoring and Evaluation Programme
<b>ESA</b>	European Space Agency
<b>ESIAS</b>	Ensemble for Stochastic Integration of Atmospheric Simulations
<b>ESIAS-chem</b>	Ensemble for Stochastic Integration of Atmospheric Simulations – Atmospheric Chemistry
<b>ESIAS-met</b>	Ensemble for Stochastic Integration of Atmospheric Simulations – Meteorology
<b>EUMETSAT</b>	European Organisation for the Exploitation of Meteorological Satellites
<b>EURAD-IM</b>	European Air pollution Dispersion–Inverse Model
<b>EUROCONTROL</b>	European Organisation for the Safety of Air Navigation
<b>FASTEX</b>	Fronts and Atlantic Storm Track Experiment
<b>FLEXPART</b>	Flexible Particle dispersion model
<b>4D-var</b>	Four Dimensional Variational data assimilation
<b>FSO</b>	Forecast Sensitivity of Observations

---

<b>GOME-2</b>	Global Ozone Monitoring Experiment-2
<b>GMAO</b>	Global Modeling and Assimilation Office
<b>HERA</b>	Hybrid Extinction Retrieval Algorithm
<b>IAGOS</b>	In-Service Aircraft for a Global Observing System
<b>IASI</b>	Infrared Atmospheric Sounding Interferometer
<b>IFS</b>	Integrated Forecasting System
<b>IIR</b>	Imaging Infrared Radiometer
<b>IN</b>	Ice Nuclei
<b>IPCC</b>	Intergovernmental Panel on Climate Change
<b>KSE</b>	Kolmogorov-Sinai Entropy
<b>L-BFGS</b>	Limited-memory Broyden-Fletcher-Goldfarb-Shenno algorithm
<b>LETKF</b>	Localized Ensemble Transform Kalman Filter
<b>Lidar</b>	Light Detection and Ranging
<b>LOTOS-EUROS</b>	Long Term Ozone Simulation – European Ozone Simulation
<b>MADE</b>	Modal Aerosol Dynamics model for Europe
<b>MISR</b>	Multi-angle Imaging Spectroradiometer
<b>MODIS</b>	Moderate Resolution Imaging Spectroradiometer
<b>MSG</b>	Meteosat Second Generation
<b>NAME</b>	Numerical Atmospheric dispersion Modeling Environment
<b>NASA</b>	National Aeronautics and Space Administration
<b>NetCDF</b>	Network Common Data Form
<b>NWP</b>	Numerical Weather Prediction
<b>OMI</b>	Ozone Monitoring Instrument
<b>OSEs</b>	Observing System Experiments
<b>OSSE</b>	Observing System Simulation Experiment
<b>PAN</b>	Peroxyacetyl Nitrate
<b>PDF</b>	Probability Density Function
<b>PS</b>	Particle Smoother
<b>Radar</b>	Radio Detection and Ranging
<b>SCA</b>	Scene Classification Algorithm
<b>SEVIRI</b>	Spinning Enhanced Visible and Infrared Imager
<b>SIBYL</b>	Selective, Iterated Boundary Location
<b>SORGAM</b>	Secondary Organic Aerosol Model
<b>SVA</b>	Singular Vector Analysis
<b>VOCs</b>	Volatile Organic Compounds
<b>WFC</b>	Wide Field Camera
<b>WMO</b>	World Meteorological Organization
<b>WRF</b>	Weather Research and Forecasting Model
<b>WRF-Chem</b>	Weather Research and Forecasting model coupled to Chemistry

# 1 | Introduction

The Earth's atmosphere transports and transforms many different aerosols originating from natural and anthropogenic emission sources, which are often dependent on hardly predictable processes. Special aerosol events include for instance wildfires, mineral dust storms, or accidental aerosol releases resulting from damage of industrial plants or reactors. Their sudden appearance in combination with their potential hazards is the reason that skillful predictions of the succeeding aerosol dispersion are indispensable. However, the assessment of meaningful predictions has a major associated challenge: emission parameters and observability, which analyzes the impact of observations on the value of the forecast in a probabilistic manner, must first be adequately quantified. This work particularly focuses on sudden aerosol events, which are characterized by the release of enormous amounts of special aerosol emissions that can cause hazardous outcomes for humans' health (*Pöschl* [2005]), and that can negatively affect society (e. g. *Chester* [2005]) and the environment (e. g. *Thordarson and Self* [2003]).

To simulate the aerosol dispersion, numerical models are used. They primarily rest on theoretical knowledge of the atmosphere system. This knowledge generally encompasses the meteorological fields as a basis for the main dynamic terms of advection, dispersion, and deposition. In case of sudden aerosol injections, dispersion models often rely on poorly known emission source describing input parameters, including emission location, emission start and end time, emission mass rate and composition, plume height, and particle size distribution. Consequently, the sum of all these uncertainties involved in the input estimations can lead to large forecast inaccuracies, such that hazard assessments might fail with fatal consequences.

The eruption of the Icelandic volcano Eyjafjallajökull in April and May 2010 can be considered as a prototype exceptional aerosol event. This incident caused a wide-reaching closure of the European air space. The temporary air traffic shutdown resulted in global economical losses of 4.7 billion US-Dollars (*Oxford Economics* [2010]). The decision to keep airplanes grounded during the volcanic ash dispersion above Europe was mainly based on simulation results of ash dispersion models. Thus in 2010, it was debated if dispersion models even approximate the true atmospheric state, and how reliable these dispersion forecasts are. Explosive volcanic eruptions are aerosol events that are particularly challenging to predict, since their emissions behave in an erratic manner. This is especially momentous because the emission plume height can change drastically within short periods over hundreds to thousands of meters altitude, and the mass eruption rate can vary from kilograms to several

tons of particulate matter per second. This thesis emphasizes the examination of volcanic aerosol events being selected as a paradigm, since it comprises these special challenges. For most considerations related to volcanic eruptions scenarios, analogical characteristics and methods can be identified for other sudden aerosol events.

To estimate the source term of volcanic ash emissions, two approaches are common. With heuristic emission modules, which rest on statistical analyses of historical eruptions, the total mass emission of the fine ash fraction can be roughly derived from emission plume height information (*Mastin et al.* [2009]; *Suzuki et al.* [1983]). The other procedure includes additional information on the eruption plume's characteristics caused by the prevailing meteorological conditions (*Woodhouse et al.* [2013]; *Folch et al.* [2016]).

Observations obtained from a wide range of different sensors can contribute valuable information about the aerosol scenario. Ground-based observations performed near the emission source can directly explore many important source parameters. Cameras observing within the infrared spectral range enable the derivation of microphysical quantities of the ash particles within the eruption plume (*Prata and Bernardo* [2009]). Ultraviolet cameras detect sulfur dioxide contained in the plume, such that the precursor amount of sulfate aerosol can be retrieved (*Burton et al.* [2015]). However, recent studies like *Burton* [2016] also apply ultraviolet imaging for volcanic ash monitoring. *Stohl et al.* [2011] used webcam observations to estimate the eruption column top heights of the 2010 Eyjafjallajökull eruption. Weather radar (radio detection and ranging) instruments are capable of capturing volcanic ash plume heights within their detection area during the normal operation of the system, as realized by *Arason et al.* [2011].

Since volcanic eruptions often occur in remote regions on Earth, where such observational infrastructure is not readily available, observations of volcanic clouds in places remote to the emission source can provide important information about the scenario. Accordingly, *Flentje et al.* [2010] performed among other observations in situ measurements of particle number concentrations of the volcanic ash that initially arrived in Southern Germany two and a half days after the eruption start of the Eyjafjallajökull. Aircraft based measurements performed on specially equipped research airplanes obtain a unique insight into the transported ash cloud (e. g. *Schumann et al.* [2011]). Remote sensing instruments are able to capture a broader picture of the volcanic ash cloud, retrieving ash characteristics from their spectral signature. With lidar (light detection and ranging) measurements, spectral and vertically resolved optical properties of the transported ash were obtained in central Europe during the Icelandic eruption in 2010, and attempts to retrieve the mass concentration within the ash clouds were carried out for instance by *Ansmann et al.* [2011] and *Gasteiger et al.* [2011]. The organization of ground-based instruments in networks is advantageous to attain the four dimensional distributions of volcanic clouds, as realized by *Pappalardo et al.* [2013] in the framework of EARLINET (European Aerosol Research Lidar Network).

Satellite sensors generally observe the horizontal distribution and extension of vol-

canic ash clouds. Here, also infrared instrumentations are primarily favorable to derive ash optical properties and estimates of mass loadings. This has been carried out by e. g. *Prata and Prata* [2012] using SEVIRI (Spinning Enhanced Visible and Infrared Imager) data and *Dubuisson et al.* [2014], who applied their retrieval algorithm to analyze near simultaneously infrared measurements from SEVIRI, MODIS (Moderate Resolution Imaging Spectroradiometer), and IASI (Infrared Atmospheric Sounding Interferometer). Volcanic ash AOD (aerosol optical depth) and microphysical properties observed by MISR (Multi-angle Imaging Spectroradiometer) even indicate aging processes of the ash plume during its transport (*Kahn and Limbacher* [2012]). Space borne lidar instruments, such as CALIOP (Cloud-Aerosol Lidar with Orthogonal Polarization) or CATS (Cloud-Aerosol Transport System) allow for the determination of the ash cloud height and thickness in addition to optical properties (*Winker et al.* [2012]), but the assessment is restricted to the re-visitation times and narrow swath of the lidar beam. A full overview of volcanic emission monitoring from space is provided by *Thomas and Watson* [2010].

In principle, observations are subject to limitations that must be considered. In particular, remote sensing retrievals are restricted to cloud clear areas. Furthermore, the discrimination of different aerosol species, and the retrieval of one certain aerosol type are challenging. Vertically integrated measurement quantities are restricted in the way that the three dimensional dispersion within the atmosphere cannot be identified. Consequently, all these limitations add up to initial measurement uncertainties.

The combination of volcanic ash transport and dispersion models with observations can be accomplished by the comparison of model results with measurements or retrievals. For instance, *Webley et al.* [2012] validated their WRF-Chem (Weather Research and Forecasting model coupled to Chemistry) ash dispersion simulation by means of different observational data from satellite and ground-based platforms. Another approach to connect models with observations is by inverse modeling and data assimilation. Thus, models can be well constrained in terms of adjusting model states, or in an enhanced way with respect to initial value or emission factor optimization (*Elbern et al.* [2007], Chap. 2 of *Zehner* [2010]). This leads to more reliable and more accurate dispersion forecasts, such that the scenario, the associated mechanisms, and subsequent hazards can be assessed. A review of how observations of airborne ash from space are exploited by volcanic ash dispersion modelers is given by *Wilkins et al.* [2016a].

*Wilkins et al.* [2016c] presented their results of the volcanic ash transport connected with the 2011 Grímsvötn eruption in Iceland using the novel technique of data insertion. Further related studies with a focus on the Eyjafjallajökull eruption are given by *Wilkins et al.* [2014; 2016b]. They initialized NAME (Numerical Atmospheric dispersion Modeling Environment) with SEVIRI ash cloud heights and column ash mass loadings retrieved with the algorithm of *Francis et al.* [2012]. Later on, they updated the model state using this retrieved data in addition to probabilistic estimates of ash, cloud, and clear sky classifications described by *Mackie and Watson* [2014]. Assuming an ash layer thickness of 1.0 km and applying satellite retrieved ash cloud heights was demonstrated as most beneficial with respect to the ash transport, while

ash concentrations were predominantly under-predicted. Further, the dynamical system evolution of the model was not appropriately considered. The method can not be applied before retrieved remote sensing data for the initialization is provided. In that work, the estimation of actual emissions was neglected, as well as observation and model errors.

*Eckhardt et al.* [2008] and *Kristiansen et al.* [2010] developed an analytical inversion method in FLEXPART (FLEXible PARTicle dispersion model) to estimate vertical profiles of sulfur dioxide emissions and tested it on the basis of the 2007 Jebel at Tair and the 2008 Kasatochi eruption, respectively. Using satellite-borne total column retrievals, the vertical wind shear of horizontal winds was exploited to extract the emission heights. *Stohl et al.* [2011] improved this method by extracting vertically and temporally resolved a posteriori emissions, as a linear combination of the best fitting a priori emission scenarios. Model errors derived from the difference of two different meteorological input data sets, and observation errors were taken into account to determine the ash emissions of the Eyjafjallajökull eruption. *Kristiansen et al.* [2012] and *Steensen et al.* [2017] applied further configurations, alternatively testing the algorithm with NAME and EMEP (European Monitoring and Evaluation Programme) dispersion models, respectively. Furthermore, *Steensen et al.* [2017] explored how different satellite data and uncertainty assumptions affect the volcanic ash emission estimates. To quantify the uncertainties of volcanic ash emissions, *Kristiansen et al.* [2012] advise an ensemble approach.

Since in the year 2010 the ECMWF's (European Centre for Medium-Range Weather Forecasts) IFS (Integrated Forecast System) did not contain a volcanic ash aerosol variable, *Benedetti et al.* [2011] initialized the volcanic emissions applying the emissions from *Stohl et al.* [2011] to the sulfate, black carbon and dust variables. The four dimensional variational (4D-var) analysis of MODIS AOD constrained the volcanic ash plume, especially in regions remote to the source. Regarding volcanic sulfur dioxide emissions, *Flemming and Inness* [2013] suggest to combine emission parameter initialization with 4D-var assimilation, both on the basis of satellite retrievals. The initialization was based on an ensemble of test tracers injected in different heights to estimate the plume height for the assimilation. Among other methods, the 4D-var approach provides the best linear unbiased estimate (BLUE, *Talagrand* [1997]) as optimality criterion, such that the results consider the uncertainties of the model as well as the observations.

*Lu et al.* [2016] set up an ensemble, where each member was assigned to a specific emission profile. With an adjoint-free trajectory based 4D-var method, the best emission estimation resulted from the weighted ensemble mean. The weights were determined by cost function minimization considering synthetic observations of ash column mass loadings in identical twin experiments. Yet, analysis uncertainty assessments were not provided in the article.

*Fu et al.* [2016] and *Fu et al.* [2017] assimilated aircraft based measurements and SEVIRI ash column mass loadings, respectively, obtained during the Eyjafjallajökull eruption. They applied an Ensemble-Kalman Filter to the stochastic version of the LOTOS-EUROS (Long Term Ozone Simulation – European Ozone Simulation)

model. Thereby, they improved the estimation of the volcanic ash state and argued that the aviation advice could be improved. Nonetheless, this is only justifiable for forecast regions downwind of the assimilated observations and later forecast times.

To assess the hazards associated with volcanic ash clouds, probabilistic methods estimating the forecast uncertainties are applied. For instance, *Denlinger et al.* [2012] performed a Bayesian analysis to determine initial conditions and uncertainties with satellite and ground-based observations. In this way, the posterior probability could be derived and proofed as robust, while Gaussian distributed uncertainties were considered.

All these studies demonstrate that inverse modeling and data assimilation overcome the limits of simple forward modeling. Therefore, model calculations are beneficially constrained by the observational data. However, the question where and to what extend observations reduce uncertainties is not directly answered, but of high practical interest. Flight route planning in aviation is a striking, yet by far not the only example. Evaluation of improvements regarding analysis quality as a product of observation configurations and data assimilation is the main subject in the research topic of observability (*Majumdar* [2016]). Interests in this research field include the optimization of observation networks, the evaluation of the quality gain in the analysis due to individual or types of observations, and the appraisal to what extend the analysis can be influenced by observations. A detailed literature review of meteorological and atmospheric chemistry related studies is provided in Chapter 2.1.1. Regarding special aerosol events, targeted observations can be expected to contribute valuable information about the scenario. Additional information can be gained from the dynamics of the system, such as when taking advantage of the vertical wind shear to estimate the horizontal distribution. However, it has rarely been evaluated which simulated temporal and spatial concentration patterns are actually controlled by observations. This might be an important aspect in consideration of a strong basis for decision making.

This work aims to develop and validate observability methodologies, which identify those areas in the analysis that are well constrained by the information content provided by observations. A related objective is to assess the limits of observability in the analyses obtained. These objectives are pursued with the application of two competing approaches:

- The analysis uncertainty is assessed with an ensemble setup of EURAD-IM (European Air pollution Dispersion – Inverse Model, *Elbern et al.* [2007]) using the 4D-var data assimilation technique in terms of initial value optimization.
- An ensemble of major size defined with ESIAS-chem (Ensemble for Stochastic Integration of Atmospheric Simulations – atmospheric chemistry part, *Franke* [2018]) is processed to perform emission factor optimization by means of non-linear particle smoother data assimilation.

These approaches are combined with the employment of two fundamentally different satellite-borne observation principles. On the one hand, SEVIRI retrievals of total ash column mass loadings are used, which are confined to capture the horizontal ash

distribution only. On the other hand, CALIOP retrieved profiles of aerosol extinction coefficients contribute with sparse, but precise vertically resolved data.

This thesis is organized as follows: in the subsequent Chapter 2, a detailed insight into the research field of observability is given. Thereby, particular attention is given to the theory of obtaining the observability of exclusively horizontally resolved observation data. Further, aerosol monitoring and the challenges of sudden aerosol injection dispersion modeling are discussed in Section 2.2 and Section 2.3, respectively. Chapter 3 introduces the concept of data assimilation, particularly focusing on the applied methods of the 4D-var approach and ensemble-based particle smoother. The aim of Chapter 4 is to introduce the observation systems of CALIOP and SEVIRI including the retrieval description and a discussion of their skills. Chapter 5 describes the modeling system of EURAD-IM as well as the ensemble environment of ESIAS. In the sequel, Chapter 6 presents the main developments achieved, to properly assimilate the selected remote sensing data and to evaluate the ensemble analysis in terms of observability. In Chapter 7, at first the selected aerosol scenario of the 2010 Eyjafjallajökull eruption and the experiments' setups are explained, before all performed experiments are analyzed and their results are summarized. The observability of SEVIRI data is investigated with both data assimilation techniques, while the additive information gain due to CALIOP data is at first examined with the 4D-var ensemble. Finally, conclusions are drawn in Chapter 8 and a perspective with suggestions for further investigations and improvements is given.

## 2 | Observability of sudden aerosol injections

Within this chapter, the theoretical approach to the term of observability is introduced. Applications in atmospheric research are reviewed and analysis theories and techniques related to the question of this thesis are discussed. The subsequent exposition gives a closer insight to the subject of aerosol monitoring. The definition of sudden aerosol injections, the presentation of different scenario types, their characteristics, and their special role in model predictions is of further concern.

### 2.1 Observability

Observability is a technical term, which originates from control theory, and has application in many different areas. For example, it is used to find the optimal sensor placement in chemical processing plants (*Brewer et al.* [2007]), to analyze navigation systems (*Batista et al.* [2011]), for water resource planning (*Xun-Gui et al.* [2012]), and in many other industrial applications. Observability describes the ability to estimate the state of a system through observations. A dynamic system is called observable if its state  $\mathbf{x}(t)$  can be uniquely determined by the inputs and the measurements  $\mathbf{y}(t)$  for all times  $t > 0$ . *Nakamura and Potthast* [2015] introduced a general definition of observability in inverse modeling: applying a linear model  $\mathbf{M}$  and observations  $y_i = H\mathbf{M}^i\mathbf{x}_0$  for  $i = 0, \dots, N$ , the linear problem can be written as

$$\begin{pmatrix} y_0 \\ y_1 \\ \vdots \\ y_N \end{pmatrix} = H \begin{pmatrix} \mathbf{M}^0 \\ \mathbf{M}^1 \\ \vdots \\ \mathbf{M}^N \end{pmatrix} \mathbf{x}_0 =: A\mathbf{x}_0 . \quad (2.1)$$

Here,  $\mathbf{x}_0$  describes the initial system state,  $H$  is the observation operator that maps the model state into observation space, and  $\mathbf{M}^i$  is the composition of  $\mathbf{M}$  defined by  $\mathbf{M}^0 = \mathbf{I}$ ,  $\mathbf{M}^i = \mathbf{M} \circ \mathbf{M}^{i-1}$ . By this definition,  $\mathbf{I}$  denotes the identity matrix. Accordingly, observability of  $\mathbf{x}_0$  is given for the observations  $y_i$ , if the operator  $A$  is injective.

In the following section, atmospheric studies on observability analysis are first summarized to give an overview on the current research status. Subsequently, analysis techniques are introduced with a focus on the investigation of initial value and emission factor optimization during sudden aerosol events.

### 2.1.1 Observability in atmospheric applications

In atmospheric sciences, observability studies are performed in the context of targeted observations. According to *Majumdar* [2016], the question to be investigated with respect to targeted observations is "Where and when should one deploy and assimilate observations, in order to improve a numerical forecast of a weather event that is important to society?". Optimized configurations of available observation capabilities and the adaptive selection of measured parameters lead to decreased uncertainties, and a reduction of the relative forecast error (*Buizza et al.* [2007]). However, if initial values and other input variables are ineligibly chosen, the forecast system can react very sensitively and result in rapidly growing forecast errors. Through data assimilation, observations can constrain the considered input parameters. Targeting observations must consequently be placed into these areas, where analysis errors reinforce large forecast errors.

The earliest application to numerical weather prediction (NWP) was provided by *Lorenz* [1965], who investigated the predictability of an idealized atmospheric model determining the largest error growth due to the choice of initial conditions. Within the last decades, several field campaigns have been performed relating to the issue of targeting observations. *Langland* [2005] described successes and limitations of targeting observations experienced from the FASTEX<sup>1</sup> in 1997. Here, the life cycle of typical Atlantic mid-latitude cyclones was explored, which is important to the short range European weather forecast (*Joly et al.* [1999]). Many other campaigns followed, including NORPEX<sup>2</sup> (*Langland et al.* [1999]) in 1998, and WSR99 and WSR00<sup>3</sup> (*Szunyogh et al.* [2002]) in 1999 and 2000, respectively. From 2003 to 2014, different campaigns were conducted in the framework of THORPEX<sup>4</sup> (e. g. *Majumdar et al.* [2011], *Fourrié et al.* [2006], *Bielli et al.* [2012]) by WMO (World Meteorological Organization). For all analyses, mathematical techniques were developed to identify the targeted regions, where the assimilation of observations yields to the largest forecast improvements. The impact of targeted observations was generally small but positive, and it was found that the impact is dependent on the region, the season, and the observation system (*Buizza et al.* [2007]). Considering the characteristics of the applied data assimilation system, *Baker and Daley* [2000] directly obtained the forecast sensitivity to the observations and to the background field.

To evaluate the impact of assimilating targeted observations and to assess the value of observational networks, observing system experiments (OSEs) were executed from the late 1990s. By adding single components of the observational data to the analysis, or by removing observational subsets, the forecast quality changes. Thus, the targeted observation impact can be rated, comparing the forecast results with a control experiment that includes all observations. The study of *Bouttier and Kelly* [2001], for example, investigated the impacts of observing systems composed of different satellite observations, radiosondes, aircraft, and drifting buoys on the ECMWF

---

<sup>1</sup>Fronts and Atlantic Storm Track EXperiment

<sup>2</sup>NORth-Pacific EXperiment

<sup>3</sup>Winter Storm Reconnaissance programs

<sup>4</sup>The Observing system Research and Predictability EXperiment

forecast system. In contrast to these real data experiments, observation system sensitivity can also be studied by observing system simulation experiments (OSSEs), where "synthetic" observations that are artificially generated, are assimilated. OSSEs relate to observing systems of potential networks or satellite missions for strategic planning of observations to provide most improvements to the respective forecast (*Hoffman and Atlas* [2016]). Thus, strategic planning of appropriately designed observation platforms can be ensured. For instance, *King et al.* [2015] developed a method finding optimal sensor locations and maximized the partial observability of the dynamical system. These methods are suitable for stationary observation platforms. The forecast sensitivity to observations (FSO) method investigates which observation types or systems contribute beneficial information content most efficiently to the forecasting system. Here, the adjoint of the data assimilation system is utilized to measure the contribution of different observation subsets to the reduction in the forecast error, averaged over a certain period (e. g. *Langland and Baker* [2004], *Cardinali* [2009], *Gelaro et al.* [2010]). Based on ensemble data assimilation, *Kalnay et al.* [2012] and *Sommer and Weissmann* [2016] implemented a localized ensemble transform Kalman filter (LETKF, *Hunt et al.* [2007]) to approximate the observation impact. Hereby, targeted observations effectively constrain forecast uncertainties and the probability density function (PDF) can be optimized.

For all observability studies, it should be mentioned that the results are strongly dependent on different factors including the model applied, the forecast horizon, the analysis region, and the data assimilation scheme. Variational and ensemble-based assimilation appears to be most beneficial with regards to observability assessments. However, forecast improvements shown by the evaluation of one variable do not necessarily imply improvements of other predicted variables. Accordingly, the interpretation of observability analyses is challenging and rarely generalizable (*Majumdar* [2016]).

In the research area of air quality and atmospheric chemistry, the observability problem is less examined and rather novel. One of the first studies is performed by *Khattatov et al.* [1999], who applied a variational assimilation method and an extended Kalman filter to photochemistry. They determined that the linear combination of initial concentrations of a few long-lived atmospheric constituents is sufficient to additionally forecast a larger number of short-lived species. *Sandu* [2006] first studied targeted observations in terms of atmospheric chemistry and determined the optimal placement of measuring sensors to minimize forecast uncertainties. Also focusing on sensor placement, *Liao et al.* [2006] applied singular vectors for the analysis of East Asian air pollution and considered stiff chemical interactions between the constituents. *Goris and Elbern* [2013] examined the most sensitive chemical compound within a certain time window and stated strategies for measurement configurations. Adapting singular vector analysis (SVA), the targeted variables were described by the chemical initial values and emissions. Thereby, they used a chemical box model to analyze the formation of ozone ( $O_3$ ) and peroxyacetyl nitrate (PAN) dependent on individual volatile organic compounds (VOCs). As extended work, *Goris and Elbern* [2015] implemented the SVA algorithms in EURAD-IM and identified, which chemical compounds must be preferably observed at the optimal

observation placement. In the framework of the zeppelin campaign ZEPTEP-2<sup>5</sup>, they enlarged the number of considered atmospheric compounds, looking at O<sub>3</sub>, NO<sub>x</sub> (nitrogen oxides), HCHO (formaldehyde), CO (carbon monoxide), HONO (nitrous acid), and OH (hydroxyl). As another aspect in atmospheric chemistry, *Wu et al.* [2017] identified the sensitivity of the observation network configurations with respect to initial value and emission rate optimization. The authors performed this study by combining ensemble Kalman filter and smoother with singular value decomposition, after clarifying issues on the formal existence and convergence of optimal observation locations on a finite time horizon (*Wu et al.* [2016]).

In a related context to sudden substance releases into the atmosphere, targeting observations appropriate to a nuclear power plant accident were investigated by *Abida and Bocquet* [2009]. Using sequential data assimilation, the information content of mobile observation stations appeared to be more efficient for the source term estimation, in contrast to locally fixed measurements. Examining the information content about aerosol physical and chemical properties, *Kahnert* [2009] obtained the observability of size-dependent aerosol compositions by "synthetic" remote sensing observations. The analysis showed that the assimilation of AOD, and vertical profiles of backscatter and extinction coefficients significantly improves the background estimate and the total mass mixing ratio, while the size-resolved aerosol composition cannot be derived sufficiently well.

## 2.1.2 Analyzing observability

There are many different approaches to investigate observability. In this section, the aim is to describe approaches that focus on the identification of system state sensitivities to observation impacts. For a deterministic atmospheric chemistry forecast, the discrete temporal evolution of the system state  $\mathbf{x} \in \mathbb{R}^n$  can be described by

$$\mathbf{x}(t_{i+1}) = M\mathbf{x}(t_i) + \mathbf{e}(t_i), \quad (2.2)$$

considering a time interval  $[t_0, t_1, \dots, t_N]$  after a fixed initial state  $\mathbf{x}(t_0)$ . Here,  $M$  is the nonlinear model operator including prognostic equations, and  $\mathbf{e}$  denotes the vector of emissions. The state variable  $\mathbf{x}(t)$  is controlled by the initial state  $\mathbf{x}(t_0)$  and the emission rates  $\mathbf{e}(t_i)$ ,  $t_i \in [t_0, t_N]$ . The system is constrained by the assumption that the model error is set to zero. Generalizing all  $m$  observations at time  $t_i$  to an observation vector  $\mathbf{y}(t_i) \in \mathbb{R}^m$ , the observation system can be written as

$$\mathbf{y}(t_i) = H\mathbf{x}(t_i) + \boldsymbol{\epsilon}(t_i) . \quad (2.3)$$

Here,  $H$  is the nonlinear forward observation operator that maps  $\mathbf{x}(t_i)$  from model space into observation space, and  $\boldsymbol{\epsilon}$  denotes the observation error.

For volcanic ash dispersion forecasts, only at a few locations is the ash height directly observable by lidars or ceilometers. Large areas, especially over sea, are exclusively observed by passive satellite sensors like SEVIRI, only giving evidence of horizontal ash cloud extension, if not occluded by clouds. In the following discussion, this

---

<sup>5</sup>ZEPpelin based Tropospheric photochemical chemistry expERiment-2

situation is taken as the standard situation to expose observability, which is finally indicated by ensemble runs and presented in spaghetti plots. This is described in three steps, starting from the theory of Kolmogorov-Sinai entropy, the Lyapunov exponents, and finally arriving at the spaghetti plots.

To introduce the concept of quantitative information gain by a stream of observations, the idea of the Kolmogorov-Sinai entropy (KSE) is introduced following *Argyris et al.* [2010]. KSE considers the dynamic evolution of the system and measures the information that is gained during every discrete time step with observations. The accuracy of the observations defines a partition of the phase space with  $L$  possible system states. Let these partitions be termed  $X_k^{(1)}, X_k^{(2)}, \dots, X_k^{(L)}$ . At first, observations  $\mathbf{y}_0 = \{y_0^{(i)}; i = 1, \dots, L\}$  are accomplished at the initial time step  $t_0$  within  $X_0^{(i)}$ . This allows a certain localization of the initial condition in phase space. On fixed time intervals  $\Delta t$ , the mapping of  $\mathbf{y}_0$  within  $X_1^{(i)}, X_2^{(i)}, \dots$  is observed as  $\mathbf{y}_1, \mathbf{y}_2, \dots$ . Here, the upper index is assigned to the phase space partition  $i \in [1, 2, \dots, L]$ , the lower index designates the time step  $t_k := k$  with  $k \in [0, 1, 2, \dots, N]$ . The mapping is defined as  $\mathbf{M}_{\Delta t} : X_k^{(i)} \rightarrow X_{k+1}^{(i)}, \mathbf{y}_k \mapsto \mathbf{y}_{k+1}$ . Since the system develops according to deterministic laws, the inverse images of the partitions  $Y_{0,k}^{(i)} = \mathbf{M}_{-k\Delta t}(X_k^{(i)})$  can be arithmetically determined. Every observation  $\mathbf{y}_k$  provides additional information about the situation of the initial observation  $\mathbf{y}_0$ , which must be placed in the intersection of  $X_0^{(i)} \cap Y_{0,k}^{(i)}$ .

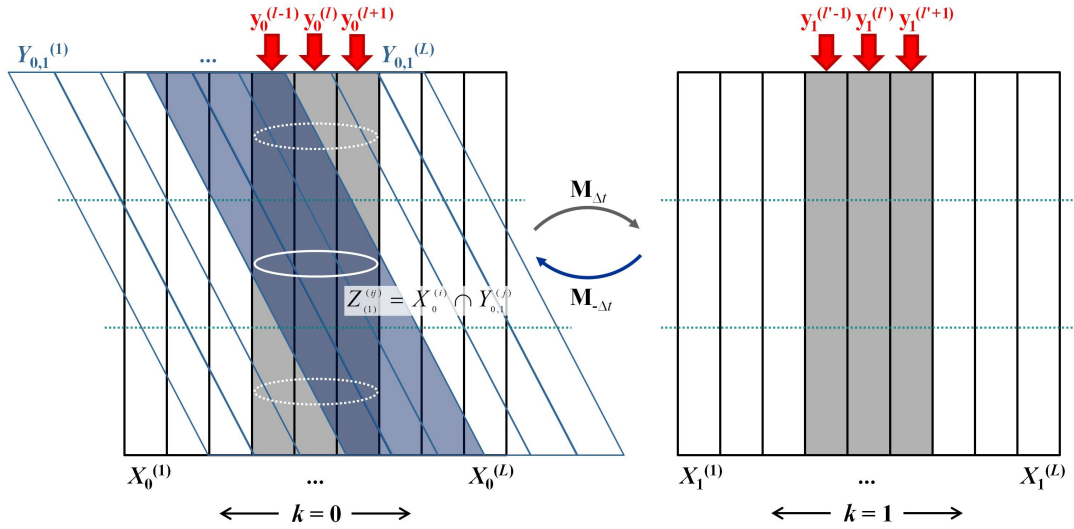


**Figure 2.1:** Illustration of the Kolmogorov-Sinai entropy for the first time step  $k = 0, 1$ .  $X_k^{(i)}$  denotes the different partitions of the pseudo-phase space,  $y_k^{(l)}$  defines the observations, here column mass loadings.  $l$  and  $l'$  state the indices of observed ash containing partitions, and  $\mathbf{M}_{\Delta t}$  and  $\mathbf{M}_{-\Delta t}$  describe the deterministic forward model and the backward in time model, respectively. The inverse image  $Y_{0,1}^{(j)}$  is depicted in blue. Assuming a horizontally layered structure of the ash, the white ellipses denote possible realizations of the location of the observed quantity, whereas the dotted horizontal lines indicate additional background knowledge about the partitions.

Figure 2.1 illustrates schematically the KSE for the first time step. In this work, the aim is to interrelate the theory of KSE with the information content that can be gained from volcanic ash column mass loadings from SEVIRI, which are only horizontally resolved observations. Hence, Figure 2.1 shows the different partitions of the pseudo-phase space  $X_k^{(i)}$  arranged within columns next to each other (white and grey), at time step  $k = 0$  on the left, and on the right at  $k = 1$  after applying the forward model  $\mathbf{M}_{\Delta t}$ . The accuracy of the partitions can be seen as analogous to the horizontal resolution of the satellite retrieval. The grey columns picture the partitions, which include observations  $\mathbf{y}_k$  of volcanic ash content, whereas the white columns are observed to have no mass load of the observed variable. Running the backward model  $\mathbf{M}_{-\Delta t}$  starting from the phase space partitions at  $k = 1$ , the inverse images  $Y_{0,1}^{(i)}$  are depicted in blue at  $k = 0$ . Within the example of volcanic ash column mass loads, the deformation of the vertical columns are taken to be caused by vertical wind shear. Looking now at the information content attained by the observations, the shaded columns all include once observed volcanic ash mass, the empty columns contain the information that no ash was observed. For a comprehensive description of the KSE, see *Argyris et al.* [2010].

To evaluate the information gain, the initial system state is examined. Now, let  $X_0$  be the complete set of the partitions  $X_0^{(i)}$  and  $Y_{0,1}$  be the set of all backward pictures  $Y_{0,1}^{(i)}$ , such that

$$X_0 = \{X_0^{(i)}; i = 1, \dots, L\}, \text{ and} \quad (2.4)$$

$$Y_{0,1} = \mathbf{M}_{-\Delta t}X_1 = \{Y_{0,1}^{(i)}; Y_{0,1}^{(i)} = \mathbf{M}_{-\Delta t}X_1^{(i)}; i = 1, \dots, L\}. \quad (2.5)$$

The intersection of all possible subsets of  $X_0$  and  $Y_{0,1}$  is called first refinement of partitioning and it is defined as

$$Z_{(1)} := X_0 \wedge Y_{0,1} := \{Z_{(1)}^{(ij)}; Z_{(1)}^{(ij)} = X_0^{(i)} \cap Y_{0,1}^{(j)}, \text{ with } i, j = 1, \dots, L\}. \quad (2.6)$$

The refinement enables a more precise localization of the initial state. Regarding the probability  $p(Z_{(1)}^{(ij)})$ , that a certain system state can be captured within a cell of the first partitioning refinement, the information gain is then given by

$$I(Z_{(1)}) = - \sum_{i,j=1}^L p(Z_{(1)}^{(ij)}) \ln \left( p(Z_{(1)}^{(ij)}) \right). \quad (2.7)$$

Proceeding with the application example of Figure 2.1, the information content of the volcanic ash position gained from the observations can be analyzed as follows: the areas, where white columns of  $X_0^{(i)}$  are overlaid by empty columns of  $Y_{0,1}^{(j)}$ , have an absolute likelihood to not contain any ash, as neither at  $k = 0$  nor at  $k = 1$  was any ash observed. The sections that show shaded areas of  $X_0^{(i)}$  or  $Y_{0,1}^{(j)}$  overlapping empty columns of  $Y_{0,1}^{(j)}$  or  $X_0^{(i)}$ , respectively, are equally probable to contain volcanic ash. Subsequently, the regions characterized by the intersection of two shaded partitions have the highest likelihood to contain volcanic ash. Upon the hypothesis that the horizontally dotted lines display the boundaries of vertical model layers and the white ellipses describe different ensemble member realizations of the ash cloud, it becomes

clear that the intermediate layer is most probable to comprise the ash cloud. Thus, the location of the volcanic ash can be constrained from the full vertical column extension to the area, which is indicated by manifold observations.

Forward and backward integration over more than one time interval  $\Delta t$  results in an increased refinement. The  $k$ -th refinement is accordingly denoted as

$$Z_{(k)} := X_0 \wedge \mathbf{M}_{-\Delta t} X_1 \wedge \mathbf{M}_{-2\Delta t} X_2 \wedge \dots \wedge \mathbf{M}_{-k\Delta t} X_k, \quad (2.8)$$

with the result that the total information gain of  $k$  refinements can be calculated as  $I(Z_{(k)})$ . Longer integration times allow for better separation of the quantities in the dynamical system, such that regions of high probability emerge to be localized more precisely. In this way, correlations between the individual measurements can be identified, as the likelihood for a particular observation value depends on previous observation values. Finally, the KSE  $h(\mu)$  is defined as the least upper bound of the average information gain per time unit, which is evoked by the dynamical system, with

$$h(\mu) = \sup_{X, \Delta t} \left( \lim_{k \rightarrow \infty} \frac{I(Z_{(k)})}{k\Delta t} \right). \quad (2.9)$$

Hereby, the supremum refers to all possible partitions of the phase space  $X$  and additionally to all considered time increments  $\Delta t$ . Parameter  $\mu$  describes an invariant natural probability measure, since  $I(Z_{(k)})$  is determined using probability density functions. In conclusion, the KSE measures the information gain per time unit one can achieve, applying a series of sequentially taken observations in combination with a model, which well characterizes the dynamical system. For regular attractors  $h(\mu) = 0$ , for strange attractors  $h(\mu)$  generally is  $> 0$ , whereas for random and chaotic systems  $h(\mu) \rightarrow \infty$  for  $k \rightarrow \infty$ . Due to the supremum, the computation of  $h(\mu)$  is hardly achievable. Therefore, the KSE is rather utilized for a theoretical or qualitative characterization of the dynamical system.

*Pesin* [1977] investigated a connection between the KSE and Lyapunov exponents, so that  $h(\mu)$  is numerically computable. Lyapunov exponents provide information about the stability of given trajectories in phase space, exploiting the exponential divergence or convergence of neighboring trajectories. According to *Argyris et al.* [2010], the maximal Lyapunov exponent is defined as

$$\alpha(\tilde{\mathbf{x}}_0) = \lim_{k \rightarrow \infty} \sup \frac{1}{k} \ln \left( \frac{|\tilde{\mathbf{x}}_k|}{|\tilde{\mathbf{x}}_0|} \right), \quad (2.10)$$

where  $\tilde{\mathbf{x}}_0$  describes the initial perturbation of the state vector  $\mathbf{x}$  and  $\tilde{\mathbf{x}}_k$  denotes the resulting perturbation of the reference trajectory after  $k$  time steps. Since CTMs are based on initial values that hardly match the true atmospheric state exactly, the initial deviations represent the initial value errors and uncertainties. If at least one  $\alpha_i > 0$ , the model described system is called unstable, whereas negative Lyapunov exponents characterize stability and a well predictable system. As a result, it is possible to conclude how sensitive the system is to small perturbations of the initial conditions. Within a certain accuracy of observations, two initial states might not be distinguishable, although their trajectories are clearly diverse after a finite time

interval. Hence, the dynamical system acts as an information source.

*Pesin* [1977] found that for  $n$ -dimensional systems, Lyapunov exponents and the KSE of a subset  $V$  of the phase space are connected on certain conditions by

$$h(\mu) = \int_V \sum^+ \alpha_i(\mathbf{x}) \mu(\mathbf{x}) d\mathbf{x}. \quad (2.11)$$

Here, the index  $+$  symbolizes that the sum only consists of positive Lyapunov exponents.

The concept of finding the most unstable initial perturbation, is considered in the theory of singular value decomposition. The emission term  $\mathbf{e}$  of Eq. (2.2) is neglected, such that the model solution only depends on the initial condition with  $\mathbf{x}(t) = M[\mathbf{x}(t_0)]$ . Adding small perturbations and applying a first-order Taylor series approximation, the model integration results in

$$M[\mathbf{x}(t_0) + \tilde{\mathbf{x}}(t_0)] = M[\mathbf{x}(t_0)] + \frac{\partial M}{\partial \mathbf{x}} \tilde{\mathbf{x}}(t_0) + O[\tilde{\mathbf{x}}(t_0)^2]. \quad (2.12)$$

Following *Kalnay* [2003], let the matrix  $\mathbf{L}(t_0, t) = \partial M / \partial \mathbf{x}$  be the propagator of the tangent linear model. It is linearized at a reference trajectory  $\mathbf{x}(t)$ , which is the solution of the nonlinear model, and does not depend on  $\tilde{\mathbf{x}}(t)$ , although it propagates the initial uncertainty to a final perturbation. Assuming the initial perturbation to be sufficiently small to evolve linearly, quadratic and higher order terms of Eq. (2.12) can be neglected. The evolution of the initial perturbation between  $t_0$  and  $t$  can be written as

$$\tilde{\mathbf{x}}(t) = \mathbf{L}(t_0, t) \tilde{\mathbf{x}}(t_0). \quad (2.13)$$

The model's adjoint is equivalent to the transpose of the tangent linear model  $\mathbf{L}^T$  and propagates the system backward in time. Singular value decomposition denotes that for the matrix  $\mathbf{L}$ , there exist two orthogonal matrices  $\mathbf{U}$  and  $\mathbf{V}$  such that

$$\mathbf{U}^T \mathbf{L} \mathbf{V} = \mathbf{S}. \quad (2.14)$$

Here,  $\mathbf{U} \mathbf{U}^T = \mathbf{I}$  and  $\mathbf{V} \mathbf{V}^T = \mathbf{I}$ , where  $\mathbf{I}$  is the identity matrix, and  $\mathbf{S}$  is a diagonal matrix with the singular values  $\sigma_i$  of  $\mathbf{L}$  as diagonal elements. The singular vectors  $\mathbf{u}_i$  and  $\mathbf{v}_i$  are the column vectors of  $\mathbf{U}$  and  $\mathbf{V}$  and it can be derived that

$$\mathbf{L}^T \mathbf{L} \mathbf{v}_i = \sigma_i \mathbf{L}^T \mathbf{u}_i = \sigma_i^2 \mathbf{v}_i. \quad (2.15)$$

*Kalnay* [2003] declare  $\mathbf{v}_i$  to be the initial and  $\mathbf{u}_i$  to be the final singular vectors. The  $\mathbf{v}_i$  vectors can be determined as the eigenvectors of  $\mathbf{L} \mathbf{L}^T$  and the squared singular values  $\sigma_i^2$  concur with the eigenvalues  $\lambda_i$  of  $\mathbf{L} \mathbf{L}^T$ . Since  $\mathbf{v}_i$  and  $\mathbf{u}_i$  span orthonormal bases in the  $n$ -dimensional tangent linear space, they facilitate the identification of the modes, which mainly determine the linearized evolution of the system. Even if the treated system is described by differential equations with infinite degrees of freedom, the dynamic can be described by a finite number of modes by lower dimensional attractors. Accordingly, instabilities within the tangent linear model can be diagnosed as each initial singular vector component expands or contracts

by the extent equal to the singular value. The direction in the phase space of the perturbation is indicated by the rotation of the evolved final singular vector. The behavior of the adjoint model can be analyzed likewise, with interchanged initial and final singular vectors. Hence, in a time interval  $[t_0, t]$ , the direction of maximum error growth is given by the first initial singular vector  $\mathbf{v}_1$  and the associated largest singular value  $\sigma_1$ .

In practise, stochastic forecasts are performed to estimate the skill of the prediction. Thereby, several model forecasts are produced for one joint analysis, each involving different perturbations, which are introduced in the initial conditions, in the parameterizations, or in the models themselves. The visualization of a single contour line for every ensemble member provides guidance on the reliability of the forecast (*Kalnay [2003]*): convergent contours display an agreement in the intensity and location of the event, implying a well predictable event, whereas strongly divergent contour lines symbolize large uncertainties in the event prediction. The latter case involves low dimensionality in perturbation space, as perturbations follow the same basis shape. A further benefit of the interpretation of these so-called spaghetti plots is the derivation of information about the necessity of adaptive or targeting observations. This is accomplished by tracing the areas of large uncertainty backward in time so that regions can be identified, where supplementary observations lead in particular to improved forecasts.

In this work, a new approach to the interpretation of spaghetti plots is enforced, finding the connection to the observability of the considered event. Therefore, ensemble analysis runs are evaluated by spaghetti plots. A small ensemble spread in the analysis indicates that the considered state variable is well observed in the way that the analysis is well constrained by the observations, while regions holding large ensemble spreads are characterized by none or inadequate observations, presuming that the model ensemble members have similar stability in this sub-domain. The ensemble spread supplies information about the system's dynamics, with the result that in the space of the ensemble members, the ensemble spread points in the direction of the initial singular vector using the linear approximation. Hereby, a connection with the theoretical approach of the KSE or rather with the more practicable information gain attempt of *Pesin [1977]* is established.

## 2.2 Monitoring aerosols

Aerosols are liquid and solid particulates in the atmosphere, originating from either natural sources, such as wind-driven elevation of soil materials or emissions due to geological and vegetational processes, or from anthropogenic sources, such as transportational, industrial, and combustion emissions. They appear with a very large spatio-temporal variety: their size, number, and chemical composition depend on diverse factors including the location, emissions, chemical and physical processes, and meteorological conditions.

Aerosols play a major role influencing the earth system in many respects. Due to the direct interaction of the particles with the solar and terrestrial radiation, the

atmosphere's energy budget changes. This interaction by scattering and absorption describes the so-called direct aerosol effect. According to *Boucher et al.* [2013] (in the Fifth Assessment Report of the Intergovernmental Panel on Climate Change – IPCC), the anthropogenic effective radiative forcing due to aerosol-radiation interactions is appraised to amount to  $-0.45 \text{ Wm}^{-2}$ . Furthermore, aerosols act as cloud condensation nuclei (CCN) and ice nuclei (IN). The clouds formed thereafter imply changes in the radiative budget and the redistribution of latent heat. These impacts are formerly known as indirect aerosol effects. The various processes influencing the climate budget are still not completely understood and are a topic of recent research. In the latest IPCC report, the total effective radiative forcing including direct and indirect aerosol effects is assessed to be  $-0.9 \text{ Wm}^{-2}$  with large uncertainties (*Boucher et al.* [2013]). Wind blown aerosols, which are deposited, for example on snow, can decrease the albedo and accelerate melting processes. Another influence of aerosols on earth system is given by the interactions of particles and gases in atmospheric chemistry. If aerosols are not directly emitted, they can be formed by gas-to-particle conversion processes (secondary aerosols), as for instance sulfate aerosols and sulfuric acid droplets result from the reaction of gaseous sulfur dioxide and with water and hydroxyl radicals. In the atmosphere, aerosols can pass through different processes, such as coagulation, meaning the encounter of different particles, condensation, describing the transition from gas phase to liquid phase on aerosol surfaces, and other chemical reactions. Even the biogeochemical cycle in the Earth's system is influenced by aerosols, as for example the iron that is contained in mineral dust serves as nutrients to the oceanic ecosystem (*Martin and Fitzwater* [1988]). In the same way, aerosols can influence vegetation on land positively. In contrast, photosynthesis and other plantal processes can be impaired due to aerosol induced attenuated radiation. Human life can also be affected by aerosols. Inhalation of aerosols and their deposition in the respiratory tract may induce health risks (*Shiraiwa et al.* [2012]). Further, daily life can be influenced, if large amounts of aerosols impact on surfaces of constructions or means of transportation (e. g. *Prata and Rose* [2015]).

Atmospheric monitoring connects all research fields regarding atmospheric processes and their impacts (*Lahoz et al.* [2012]). The fields of aerosol measurements and aerosol modeling are shortly presented in the following paragraphs, since their evaluation mainly supports reasonable decision making and risk management.

Aerosols are observed from all different monitoring platforms, namely from ground-based stations, on the ocean mainly from ship-based platforms, and from balloons, aircraft, and satellites. Ground-based measurements are restricted point measurements and might only be representative on a very local scale. On that account, they are generally composed in observation network infrastructures to achieve larger coverage and organized operation. Sophisticated ground-based, ship, balloon and aircraft borne data are typically only available on a campaign basis. But recently, there have been attempts for implementation of routine measurements, such as the In-Service Aircraft for a Global Observing System (IAGOS, *Petzold et al.* [2015]) on airplanes. Observations from space have the advantage to provide operational measurements on global scale for polar-orbiting satellites and reduced hemispheric

scale for geostationary satellites.

Observation techniques are distinguished between in situ and remote sensing measurements. In situ observations refer to the measurement of aerosols directly at their location, either taken on the ground or from aircraft. This is of great advantage to receive precise information about the aerosol characteristics, such as for instance particle size, number, or composition. In contrast to the gaseous components of the atmosphere, aerosols are not fully described with reference to their concentration. Accordingly, there are many different observation quantities, which characterize aerosols, like mass and number concentrations, size spectrum, shape, internal structures and chemical composition, and optical and physical properties (e. g. *Minikin et al.* [2012]).

Remote sensing measurements correspond to observations obtained from distance. The instrumentation can be installed on ground, boats, aircraft, and satellites. Remote sensing instruments detect the spectral signatures of the aerosols within a certain wavelength mask. Sensors, that record the reflected, absorbed and scattered radiation originating from the sun or the Earth's surface, are named passive instruments. They are distinguished from active sensors that emit a well defined energy into the atmosphere and detect the reflected and backscattered signal. Observing from distance gives a broader picture of the aerosol conditions in the atmosphere with remote sensors compared to in situ measurements. Hence, typical remote sensing aerosol products are the spatial distribution, both horizontally and vertically, the temporal variation, the fraction of fine and coarse particle modes, and a large variety of the spectral characteristics (e. g. *Lee et al.* [2009]). With additional post-processing of the data products, many other aerosol quantities can be retrieved. Nevertheless, the retrieval of aerosol remote sensing data is an ill-posed problem because the number of properties to ideally describe the aerosols in the atmosphere is much larger than the number of parameters that can be derived from the measurements. Further, remote sensing is impaired by the influence of molecular scattering, gas absorption, and surface reflection. For aerosol observations, the presence of clouds inhibits the detection of aerosol signatures, either due to overwhelming cloud reflection using passive sensors or as a result of signal extinction in the case of active remote sensing. Aerosol models simulate the chemical and microphysical properties of the particles and their spatio-temporal distribution (e. g. *Hendricks et al.* [2012]). Since the simulations allow for the collection of consistent information about atmospheric conditions where observations are not available, aerosol scenarios for past and future conditions may also be studied. The scales of aerosol models differ from global scale (e. g. the ECMWF Integrated Forecasting System – IFS, *Morcrette et al.* [2009]) with a resolution of up to hundreds of kilometers to local scales (e. g. the Modal Aerosol Dynamics model for Europe – MADE, *Ackermann et al.* [1998]) with resolutions down to a few meters.

The aerosol properties to be modeled generally include the mass concentration, the size distribution, the chemical composition, the shape, and the solubility and mixing state. The properties vary from model to model and the list can be extended by many aerosol characteristics. Since modeled aerosol sizes generally range from a few

nanometers to more than ten micrometers, they are implemented within a modal aerosol scheme or by size bins. The set of simulated aerosol species is individual for each aerosol module, but the main constituents are sulfate, nitrate, ammonium, black and organic carbon, mineral dust, sea salt and water. To describe the dynamics of aerosols, a selection of the physical and chemical processes is realized in the numerical code of the models. By way of example, advection, diffusion, and sedimentation describe the transportation processes of aerosols within the atmosphere. Coagulation, condensation, evaporation, nucleation, and aerosol-cloud interactions determine conversion processes and emissions and deposition depict the sources and sinks, respectively. To estimate the influences of aerosols on the energy budget, an associated radiative transfer module processing the aerosol-radiation interactions must be linked.

Inverse modeling and data assimilation are important contributions to aerosol monitoring. Aerosol models suffer from uncertain initial conditions and insufficient knowledge about the emission sources. Therefore, the observational information helps to overcome these weaknesses by using assimilation algorithms that accomplish initial value and emission factor optimization.

## 2.3 Special aerosol events

The term of special aerosol events involves all scenarios that emerge with low probability, and where large amounts of particulate matter are suddenly injected into the atmosphere. Such emission events have in common that they occur unexpectedly, the emitted substances do not constitute of ordinary everyday aerosol, and the events are hardly predictable. Thus, special aerosol events are rarely respected in generic air quality forecasts, unless additional information about the scenario contributes to the modeling system. But to appraise the consequences and hazards of the injected pollutants, chemistry transport models are sustained by additional information about the scenario to simulate the pollutants' dispersion.

This added information is often affected by very large errors of the emission parameters: in many occasions, the emission location and the inception of the aerosol injection are not exactly known. Especially problematic is the assignment of the injection height and the amount of emitted material. In a similar manner, the composition and size distribution of the aerosols is not fully determinable. Consequently, the numerical evaluation of the vertical and horizontal distribution, the transport, physical and chemical processes within the atmosphere, as well as sink processes such as sedimentation and deposition cannot be absolutely precise, if the emission parameters have large uncertainties. Hence, the quality of the aerosol forecast is impaired.

The assessment of these parameters by measurements is often hardly realizable. If there are observation instruments nearby, it is still challenging to capture the full extension of the scenario. In many cases, special events even take place in remote regions of the globe, where close observations are barely available. In this case the appraisal of the scenario and its emissions is performed by data assimilation of

observations, which are obtained in places remote to the emission source. In this way, comprehension of the scenario, the associated processes and hazards can be gained. In the following section, the main types of sudden aerosol injections are described and their relevance on consideration interest is discussed:

### **Volcanic eruptions**

Volcanic eruptions occur in many different eruption styles. Explosive or so-called hydromagmatic eruptions characterize the style by which huge amounts of volcanic particles and gases can be injected into the atmosphere. These eruptions are provoked by the encounter of hot magma with water. The full set of erupted material is termed tephra, whereas the aerosol portion characterized by particle diameters  $\leq 2$  mm is called volcanic ash (*Cashman and Rust* [2016]). The ash is composed of crystals and glassy fragments of mainly basalt, andesite, or rhyolite, which differ in terms of silicon dioxide ( $\text{SiO}_2$ ) percentage. Another important volcanic aerosol is sulfate, which is formed during transport from emitted sulfur dioxide.

Volcanic aerosol emissions are of special interest to be monitored, because they have a strong impact on climate (e. g. *Robock* [2000]), vegetation (e. g. *Grattan and Pyatt* [1994]), and on health (e. g. *Hansell et al.* [2006]). Aviation can be affected during volcanic eruptions, since the aircraft turbines operate within the temperature ranges of the melting point of volcanic ash. Subsequent engine failures can be very hazardous, so that air traffic control centers advise the airplanes to stay grounded (*Prata and Rose* [2015]).

### **Mineral dust uplifts**

Mineral dust raising is generally induced by aeolian erosion of the ground in arid and semi-arid regions. Also human activities can provoke the uplift of dust. In total, about 2000 Mt dust are annually emitted into the atmosphere (*Shao et al.* [2011]). Mineral dust appears in different chemical compositions (*Formenti et al.* [2003]), which are represented by the varying portions of sand, silt, and clay in chemistry transport models (e. g. *Tegen and Fung* [1994]).

In some parts of the world, mineral dust regularly affects the air quality in the planetary boundary layer (e. g. *Prospero* [1999]). Certain atmospheric chemistry processes as well as cloud formation are triggered by the presence of mineral dust particles (*Bauer et al.* [2004]). On regional to global scales, mineral dust even influences the Earth system: it changes the radiative balance (*Sokolik and Toon* [1999]) and interacts with bio-geochemical processes such as the carbon cycle (*Shao et al.* [2011]). The impact on human health (e. g. *Griffin and Kellogg* [2004]) is significant even in places remote to the desert region due to the long distance transport.

### **Wildfire emissions**

Wildfires include all kind of vegetation fires such as forest fires, bush fires, peat fires, or grass fires. They can arise due to deliberate and accidental arson, or they can be set on fire naturally by lightning. The pollutants released by wildfires include many greenhouse gases (carbon dioxide, methane, nitrous oxide etc.) and particulate matter, mainly consisting of black and organic carbon (*Andreae and Merlet* [2001]).

Wildfires are generally dangerous, as they actively destroy parts of the ecosystem. The released smoke strongly contributes to air pollution and impacts the climate system in terms of radiation and atmospheric chemistry (e. g. *Langmann et al.* [2009]). Furthermore, the emitted particulates can be unhealthy or even toxic to be inhaled (*Kim et al.* [2014]).

### **Accidental releases**

The scenarios of accidental releases encompass pollutant emissions rising into the atmosphere as consequence of a damage or breakdown of industrial plants. The emitted aerosols can include a variety of anthropogenic substances, but if there is a fire involved in the accident, the released aerosols surely involve carbon compounds. In case of nuclear accidents like for example in Fukushima in 2011, the emitted material is even radioactive (*Adachi et al.* [2013]).

Although accidental releases are rarely investigated in atmospheric science, the related hazards and impacts are evident: in the same way as for the above described aerosol scenarios, aerosols released during industrial accidents interact with radiation. They impact air quality and atmospheric chemistry, and they can be very hazardous to all kind of organisms on Earth.

## 3 | Data Assimilation

In atmospheric science, the objective is to gain a detailed understanding of the physical and chemical processes in the atmosphere and its interactions with associated earth system compartments. Both prospects of modeling and observations allow the obtainment of reliable information about the atmospheric system (see Section 2.2). However, the concept of data assimilation addresses algorithms that provide the most accurate and consistent image of the system state and its evolution. For this optimal state estimation, observational information and a priori knowledge are combined with physical and chemical laws by models. Data assimilation can propagate information from data-rich regions to data-poor areas and, to a certain extent, it enables the gain of additional information on unobserved variables. Allowing for specific uncertainties and errors of the information elements, their respective contribution to the analysis is weighted. Therefore, data assimilation encompasses various techniques, proceeding from estimation and probability to control theories.

In the following sections, the concept of four dimensional variational (4D-var) data assimilation is introduced as well as the theory of the ensemble-based particle filter and smoother. Detailed descriptions of the historical development of and accomplishments due to various data assimilation techniques, mainly of atmospheric emphasis, are given by *Daley* [1991], *Talagrand* [1997], *Kalnay* [2003], *Lahoz et al.* [2010], and *van Leeuwen* [2015].

### 3.1 Four dimensional variational data assimilation

A well established data assimilation method in numerical weather prediction that enables to improve the knowledge of the system state is given by 4D-var data assimilation (e. g. *Rabier et al.* [2000]; *Navon* [2009]). Yet to a minor degree, 4D-var data assimilation is also applied in inverse atmospheric chemistry transport modeling (e. g. *Elbern et al.* [2000; 2007]; *Wang et al.* [2001]; *Engelen and McNally* [2005]). In general, the 4D-var approach seeks to find the most probable model parameters or initial states by applying the variational calculus. Thereby, these parameters are optimized in space and with simultaneous consideration of the temporal evolution of the system.

The objective is to determine the best estimation of a state variable  $\mathbf{x}$ , taking into account a first guess estimation  $\mathbf{x}_b$ , named background, and observations  $\mathbf{y}$ . Hence,

the a posteriori probability  $p(\mathbf{x}|\mathbf{y})$  can be derived with the Bayes' Theorem, such that

$$p(\mathbf{x}|\mathbf{y}) = \frac{p(\mathbf{y}|\mathbf{x})p(\mathbf{x})}{p(\mathbf{y})} = \frac{p(\mathbf{y}|\mathbf{x})p(\mathbf{x})}{\int p(\mathbf{y}|\mathbf{x}')p(\mathbf{x}')d\mathbf{x}'}. \quad (3.1)$$

Here,  $p(\mathbf{x})$  denotes the a priori probability density function (PDF), describing the knowledge of the likelihood of the model state, and  $p(\mathbf{y})$  is the PDF of the observations.

The negative natural logarithm is applied to Equation (3.1), which yields the cost function

$$J(\mathbf{x}) = -\ln(p(\mathbf{x}|\mathbf{y})) + c = -\ln(p(\mathbf{y}|\mathbf{x})) - \ln(p(\mathbf{x})) + c, \quad (3.2)$$

where  $c$  is a constant resulting from the denominator in Equation (3.1). Thereby,  $\mathbf{y} \in \mathbb{R}^M$  with  $M$  being the dimension of the partial phase space of the observations. In addition, the misfit of the background field  $\mathbf{x}_b$  to the state vector  $\mathbf{x}$  is taken into account. The background field can either be acquired by a short term forecast or by climatology such that  $\mathbf{x}_b \in \mathbb{R}^N$  with  $N$  the dimension of the partial phase space of the model state, which is identical to the dimension of the background phase space. Assuming uncorrelated background and observation errors and Gaussian distributed PDFs, the a priori PDF and the observation likelihood PDF read

$$\begin{aligned} p(\mathbf{x}_b|\mathbf{x}) &= \frac{1}{\sqrt{2\pi}^N |\mathbf{B}|^{1/2}} \exp\left(-\frac{1}{2}(\mathbf{x}_b - \mathbf{x})^T \mathbf{B}^{-1}(\mathbf{x}_b - \mathbf{x})\right), \text{ and} \\ p(\mathbf{y}|\mathbf{x}) &= \frac{1}{\sqrt{2\pi}^M |\mathbf{R}|^{1/2}} \exp\left(-\frac{1}{2}(\mathbf{y} - H(\mathbf{x}))^T \mathbf{R}^{-1}(\mathbf{y} - H(\mathbf{x}))\right), \end{aligned} \quad (3.3)$$

respectively. The superscript  $T$  denotes the transposed of a vector,  $\mathbf{B} \in \mathbb{R}^{N \times N}$  is the background error covariance matrix, and  $\mathbf{R} \in \mathbb{R}^{M \times M}$  indicates the observation error covariance matrix.  $H$  depicts the forward observation operator that maps the model state vector from model space into the space of observations (see Section 2.1.2).

Thus, choosing an appropriate constant  $c$  of Equation (3.2), the maximum a posteriori probability can be obtained by finding the minimum of the scalar cost function

$$J(\mathbf{x}) = \frac{1}{2}(\mathbf{x}_b - \mathbf{x})^T \mathbf{B}^{-1}(\mathbf{x}_b - \mathbf{x}) + \frac{1}{2}(\mathbf{y} - H(\mathbf{x}))^T \mathbf{R}^{-1}(\mathbf{y} - H(\mathbf{x})). \quad (3.4)$$

This is the standard 3D-var cost function, which does not take the temporal evolution of the system into account. In 4D-var data assimilation, timely smoothing is achieved by comparing all observations within the assimilation window with the corresponding model state and integrating the information forward and backward in time. Additionally, the cost function is now transferred to the incremental representation (*Courtier et al.* [1994]), where  $\mathbf{x}(t_0) = \mathbf{x}_b(t_0) + \delta\mathbf{x}(t_0)$ , and  $\mathbf{d}(t_i) = \mathbf{y}(t_i) - \mathbf{H}\mathbf{M}_i\mathbf{x}_b(t_i)$ , such that

$$\begin{aligned} J(\delta\mathbf{x}(t_0)) &= \frac{1}{2}(\delta\mathbf{x}(t_0))^T \mathbf{B}^{-1}(\delta\mathbf{x}(t_0)) \\ &+ \frac{1}{2} \sum_{i=1}^N (\mathbf{d}(t_i) - \mathbf{H}\mathbf{M}_i\delta\mathbf{x}(t_i))^T \mathbf{R}^{-1}(\mathbf{d}(t_i) - \mathbf{H}\mathbf{M}_i\delta\mathbf{x}(t_i)). \end{aligned} \quad (3.5)$$

This cost function, which is used for initial value optimization, is defined within the time interval  $[t_0, t_N]$ .  $\mathbf{H}$  and  $\mathbf{M}_i$  describe the linearized observation operator and the tangent linear model integration operator with  $\mathbf{M}_i = \mathbf{M}_{t_i} \mathbf{M}_{t_i - \Delta t} \dots \mathbf{M}_{\Delta t}$ , respectively. According to *Elbern et al.* [2007], a joint optimization of initial values and emission factors is attainable by adding a third, emission related term, with  $\mathbf{K} \in \mathbb{R}^{E \times E}$  the covariance matrix of emission errors, and perturbations  $\delta \mathbf{u}$  resulting in

$$\begin{aligned} J(\delta \mathbf{x}(t_0), \delta \mathbf{u}) &= J_b + J_o + J_e \\ &= \frac{1}{2} (\delta \mathbf{x}(t_0))^T \mathbf{B}^{-1} (\delta \mathbf{x}(t_0)) \\ &\quad + \frac{1}{2} \sum_{i=1}^N (\mathbf{d}(t_i) - \mathbf{H} \mathbf{M}_i \delta \mathbf{x}(t_i))^T \mathbf{R}^{-1} (\mathbf{d}(t_i) - \mathbf{H} \mathbf{M}_i \delta \mathbf{x}(t_i)) \\ &\quad + \frac{1}{2} (\delta \mathbf{u})^T \mathbf{K}^{-1} (\delta \mathbf{u}). \end{aligned} \quad (3.6)$$

The number of emission factors is represented by  $E$  and  $\delta \mathbf{u}$  denotes a scaled deviation of the modified emissions  $\mathbf{e}$  from the background emission rate values  $\mathbf{e}_b$ . To minimize this cost function, the root of its gradient

$$\nabla J = \mathbf{B}^{-1} \delta \mathbf{x}(t_0) - \sum_{t_i=t_0}^{t_N} \mathbf{M}_i^* \mathbf{H}^T \mathbf{R}^{-1} (\mathbf{d}(t_i) - \mathbf{H} \mathbf{M}_i \delta \mathbf{x}(t_i)) + \mathbf{K}^{-1} \delta \mathbf{u} \quad (3.7)$$

must be determined.  $\mathbf{H}^T$  denotes the transposed of the tangent linear observation operator and  $\mathbf{M}^*$  is the adjoint of the tangent linear forward model. It propagates the observational increments backwards in time, from time step  $t_i$  to the initial time  $t_0$ .  $\mathbf{H}^T$  maps the vectors from observation space into model space. As a result, the variational data assimilation algorithm fulfills the preconditions that the observation operator and the model itself are linear or linearized, and all errors are Gaussian distributed, to provide the best linear unbiased estimation (BLUE) as analysis. In practice, the cost function is minimized by iterative minimization algorithms such as quasi-Newton or conjugate gradient methods.

For the calculation of the costs (Equation (3.6)) and the gradient (Equation (3.7)), the background error covariances of both the model state variables and the emission factors must be known. They weight the accuracy of the background state or emission knowledge relative to the observational accuracy, and they correlate the different components of the state or emission vector, respectively (*Elbern and Schmidt* [2001]). In general, the construction of the background error covariance matrix  $\mathbf{B}$  is challenging, since it includes the cross-correlations of the entries of the model state vector, which has a dimension of  $O(10^6)$ , and it has a high condition number. The diffusion approach following *Weaver and Courtier* [2001] is an excellent method as it sets up a proper covariance model operator utilizing the diffusion equation and regarding the square root of the covariances. Thus, higher flexibility in the design of anisotropic and heterogeneous influence radii is guaranteed (*Elbern et al.* [2007]). Furthermore, intensive computations of  $\mathbf{B}$  and  $\mathbf{K}$  can be circumvented by applying the preconditioning of the cost function (*Weaver and Courtier* [2001]; *Elbern et al.* [2007]). Therefore, the background error covariance matrices are split up using their

square roots such that  $\mathbf{B} = \mathbf{B}^{1/2}\mathbf{B}^{T/2}$  and  $\mathbf{K} = \mathbf{K}^{1/2}\mathbf{K}^{T/2}$ . In a next step, new variables  $\mathbf{v}$  and  $\mathbf{w}$  are defined as

$$\mathbf{v} := \mathbf{B}^{-1/2}\delta\mathbf{x}, \quad \text{and} \quad \mathbf{w} := \mathbf{K}^{-1/2}\delta\mathbf{u}. \quad (3.8)$$

Substituting these variables into Equation (3.6), the cost function can be expressed as

$$J(\mathbf{v}, \mathbf{w}) = \frac{1}{2}\mathbf{v}^T\mathbf{v} + J_o + \frac{1}{2}\mathbf{w}^T\mathbf{w}. \quad (3.9)$$

Consequently, the gradient of the cost function with respect to the newly derived variables  $\mathbf{v}$  and  $\mathbf{w}$  is determined by

$$\nabla J(\mathbf{v}, \mathbf{w}) = \begin{pmatrix} \mathbf{v} \\ \mathbf{w} \end{pmatrix} - \begin{pmatrix} \mathbf{B}^{1/2} & \mathbf{0} \\ \mathbf{0} & \mathbf{K}^{1/2} \end{pmatrix} \times \sum_{t_i=t_0}^{t_N} \mathbf{H}^T \mathbf{M}_i^* \mathbf{R}^{-1} (\mathbf{d}(t_i) - \mathbf{H}\mathbf{M}_i \delta\mathbf{x}(t_i)). \quad (3.10)$$

For operational application, the preconditioning presents a suitable method for 4D-var data assimilation, which allows for an easier computation of the gradient of the cost function. Further, the chosen substitution of  $\mathbf{v}$  and  $\mathbf{w}$  compensates ill-conditioned features that occur due to the formulation of  $\mathbf{B}$  and  $\mathbf{K}$ , as for example an unfavorable condition number of the covariance matrices during the minimization procedure (*Elbern and Schmidt* [2001]). Since the model state  $\mathbf{x}$  of the initial iteration is initialized with the initial background state  $\mathbf{x}_b$ , the difference  $\delta\mathbf{x} = 0$ . Moreover,  $\mathbf{v} = 0$  enters the minimization algorithm during the first iteration. The same applies to  $\mathbf{w}$ . After the minimization, the optimized initial state and emission vector  $\mathbf{e}$  are determined by

$$\begin{aligned} \mathbf{x}(t_0) &= \mathbf{B}^{1/2}\mathbf{v}(t_0) + \mathbf{x}_b(t_0), \quad \text{and} \\ \mathbf{e}(t_0) &= \mathbf{K}^{1/2}\mathbf{w}(t_0) + \mathbf{e}_b(t_0). \end{aligned} \quad (3.11)$$

During every following iteration,  $\mathbf{v}$  and  $\mathbf{w}$  as well as  $\mathbf{x}$  and  $\mathbf{e}$  are updated. Hence,  $\mathbf{x}$  and  $\mathbf{e}$  converge to the analysis iteratively.

Detailed derivations and supplementary aspects of the 4D-var data assimilation algorithms are given in *Elbern et al.* [1997], *Bouttier and Courtier* [1999], and *Lorenz* [2003].

## 3.2 Ensemble data assimilation via particle smoother

For 25 years, operational numerical weather prediction has benefited from ensemble forecasting (*Toth and Kalnay* [1993]; *Tracton and Kalnay* [1993]). Ensemble modeling describes the procedure of simulating different realizations of a system, processing several model runs of the same episode, for instance by introducing perturbations in the initial conditions or in the model formulations. As a result of these stochastic forecasts, the skill of the prediction can be estimated and additionally, the forecast uncertainties can be obtained from the ensemble spread. Ideally, the set ensemble

members should represent the uncertainty of the initial conditions, as well as the uncertainty of other introduced perturbations. The same holds true for the resulting data assimilation analyses. With the increase of computational resources, ensemble modeling has been established in many fields of atmospheric research: as mentioned before, ensembles are extremely important to numerical weather prediction (*Buizza et al. [2005]*), but also climate modeling (*Murphy et al. [2004]*), air quality modeling (*Marécal et al. [2015]*), and the more specific topic of dispersion simulation of released matter during special events (*Galmarini et al. [2001]*; *Kristiansen et al. [2012]*) profit significantly.

Most of the developed ensemble data assimilation methods, such as the ensemble Kalman filter (*Evensen [2009]*), rely on linear or linearized models, and on the assumption of Gaussian error statistics. This is insufficient for atmospheric models, which feature the representation of a complex nonlinear system. The approach of particle filtering eludes these assumptions and allows for nonlinearities of the model and its errors (*van Leeuwen [2009]*).

The method rests on the Bayes' Theorem (Equation (3.1)), where the a priori PDF is represented by an ensemble of  $N_{em}$  model runs, with probability

$$p(\mathbf{x}) = \frac{1}{N_{em}} \sum_{i=1}^{N_{em}} \delta(\mathbf{x} - \mathbf{x}_i), \quad (3.12)$$

where  $\mathbf{x}_i$  denotes the model state of the  $i^{\text{th}}$  ensemble member, also named particle, while  $\delta$  indicates the Dirac delta function. By applying a model, the particles are propagated forward in time to the next observation time  $t$ . Subsequently, the weight is attributed to each ensemble member  $i$  following

$$w_i(t) = \frac{p(\mathbf{y}(t)|\mathbf{x}_i(t))}{\sum_{j=1}^{N_{em}} p(\mathbf{y}(t)|\mathbf{x}_j(t))}, \quad (3.13)$$

by assessing the distance of the model state to the observation. The a posteriori PDF at time  $t$  is determined by inserting Equation (3.12) in Equation (3.1), resulting in

$$p(\mathbf{x}(t)|\mathbf{y}(t)) = \sum_{i=1}^{N_{em}} \frac{p(\mathbf{y}(t)|\mathbf{x}_i(t))}{\sum_{j=1}^{N_{em}} p(\mathbf{y}(t)|\mathbf{x}_j(t))} \delta(\mathbf{x}(t) - \mathbf{x}_i(t)). \quad (3.14)$$

In a next step, the resampling of the ensemble members with respect to the ensemble members' weights takes place: the classical particle filter accomplishes the resampling by multiplying individual particles according to their weights, which can lead to either the elimination of weak ensemble members or the replication of strong ensemble members; or by finding new members in the neighborhood of the particles with sufficiently large weights (*Nakamura and Potthast [2015]*). With the new selection of particles, the ensemble model is again propagated forward in time to the next available observation set. The procedures of weighting, resampling, and model integration are repeated accordingly. The ensemble mean of the a posteriori ensemble representation is defined as

$$\bar{\mathbf{x}} = \int \mathbf{x} p(\mathbf{x}|\mathbf{y}) d\mathbf{x} \approx \sum_{i=1}^{N_{em}} w_i \mathbf{x}_i \quad (3.15)$$

and tends to depict the best estimation of the predicted or analyzed system state. In contrast to particle filters, which always propagate forward in time, step by step, the particle smoother reuses earlier observations anew to determine the weights  $w_i$  upon proceeding to a new observation time. This assures consistency with measurements over the entire assimilation window.

A problem of particle filter and smoother algorithms is the filter degeneracy. It describes the dominance of a few particles prevailing in many resampling steps, while a larger portion of particles are assigned to negligible weights. Thus, the statistical information in the ensemble becomes insignificant. Discussion of attempts to overcome filtering degeneracy is exposed by e. g. *Li et al.* [2014] and *Snyder et al.* [2008], and is beyond the scope of this thesis.

## 4 | Observations

Observational data from two completely diverse satellite systems are used for both data assimilation and evaluation of the resulting analyses. In this chapter, the different observation systems of SEVIRI and CALIOP are introduced. The data applied in this work are described in detail as well as the underlying retrieval algorithms. These retrievals convert the measured spectral radiance into an atmospheric or geophysical quantities, as mass concentrations or aerosol extinction coefficients. Observational data, which are exclusively used for validation purposes, are shortly presented for each case in the analysis Chapter 7.

### 4.1 SEVIRI

To receive information about the horizontal distribution of aerosols above Europe, retrieval data from the optical imaging radiometer SEVIRI are chosen. While SEVIRI has the capability to gather observations of many different atmospheric phenomena, the focus here is on volcanic ash observations.

#### 4.1.1 Instrumentation and measurement configuration

The Spinning Enhanced Visible and Infrared Imager (SEVIRI) is installed on board the European geostationary meteorological satellite Meteosat Second Generation (MSG, *Schmetz et al.* [2002]). The MSG program, as cooperation between EUMETSAT (EUropean organisation for the exploitation of METeorological SATellites) and ESA (European Space Agency), involves four similar satellites (Meteosat-8, -9, -10 and -11) in total, operating since January 2004 successively, still time overlapping and therefore in backup service. One of these spin stabilized MSG satellites (Figure 4.1) provides real-time imagery, orbiting the Earth in about 36 000 km altitude with a nadir point of approximately 0°North, 0°West. As a geostationary satellite its orbit takes 24 hours, whereas the satellite rotates 100 revolutions per minute around its own axis, which is aligned in parallel with the north-south axis of the Earth.

The SEVIRI instrument (*Aminou* [2002]) is an optical imaging radiometer and has a total field of view on the Earth's disc from about 70°S (south) to 70°N (north) and from 70°W (west) to 70°E (east). Eleven spectral channels are integrated with three detectors and one high resolution channel with nine detectors, scanning the Earth and atmosphere line by line from South to North and East to West. The resulting images are composed of  $3712 \times 3712$  diamond shaped pixels for the eleven normal

channels and  $11136 \times 5568$  pixels for the high resolution channel. Correspondingly, the sub-satellite spatial resolution comprises  $3 \text{ km} \times 3 \text{ km}$  and  $1 \text{ km} \times 1 \text{ km}$  for the standard channels and the high resolution channel, respectively. The horizontal resolution increases to approximately  $10 \text{ km} \times 10 \text{ km}$  at the edges of the scanning field. The received full disc images are provided remarkably frequent with a repeat cycle of 15 minutes.

SEVIRI's channels observing the earth-atmosphere system include eleven narrow-band channels in the visible and infrared electromagnetic spectrum with a nominal spectral band width of about  $1 \mu\text{m}$ , and one high resolution broad band channel in the visible spectrum (see Tabel 4.1). Each channel has individual capacities to collect information about clouds, aerosol, water vapor, land and sea surface, or ozone. Via cloud tracking, wind fields can be ascertained. The combination of the atmospheric spectral response at different wavelength ranges enables, among other things, the receipt of information regarding atmospheric instabilities (*König and de Coning* [2009]), and the discrimination of aerosol species like volcanic ash (*Prata* [1989]) and mineral dust (*Banks and Brindley* [2013]). Due to the observation frequency, even rapidly changing phenomena like convective storms can be well tracked and hazardous effects can be estimated and predicted (*Senf et al.* [2015]).

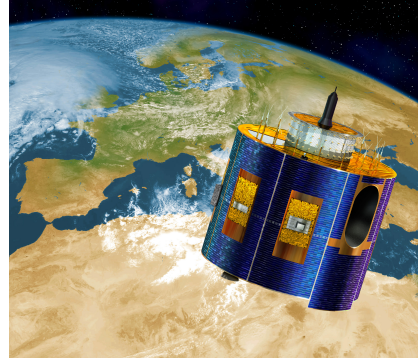


**Figure 4.1:** Artist's view of Meteosat Second Generation in space (source: *ESA* [2002]). The oval aperture on the right side of the satellite depicts the lens cover of SEVIRI.

**Table 4.1:** Characteristics of SEVIRI's spectral channels, examining the wavelength range and the observation request of each channel. The information is assembled from *Schmetz et al.* [2002] and *Schmetz et al.* [2005].

No.	Name	Spectral Band [ $\mu\text{m}$ ]	Observation Objective
1	VIS 0.6	0.56 – 0.71	clouds, aerosols, wind, surface, vegetation
2	VIS 0.8	0.74 – 0.88	clouds, aerosols, wind, surface, vegetation
3	NIR 1.6	1.50 – 1.78	cloud phase, aerosols, surface
4	IR 3.9	3.48 – 4.36	low clouds, fog, wind, surface temperatures
5	WV 6.2	5.35 – 7.15	water vapor, high level clouds/wind
6	WV 7.3	6.85 – 7.85	water vapor, atmospheric instability
7	IR 8.7	8.30 – 9.10	cirrus clouds, atmospheric instability, surface
8	IR 9.7	9.38 – 9.94	ozone, wind in lower stratosphere
9	IR 10.8	9.80 – 11.80	cloud top temperature, wind, surface
10	IR 12.0	11.00 – 13.00	cloud top temperature, surface
11	IR 13.4	12.40 – 14.40	cirrus cloud height, atmospheric instability
12	HRV	0.4 – 1.1	clouds, surface

### 4.1.2 Volcanic ash mass loading retrieval

For the retrieval of volcanic ash concentrations and other parameters from SEVIRI measurements, the observed signatures of infrared channels are simulated with a radiative transfer model. As a first step, all observed pixels containing volcanic ash must be identified and discriminated from pixels including meteorological clouds, smoke, anthropogenic aerosols, and wind blown mineral dust. Therefore, the retrieval algorithm takes advantage of the reverse absorption effect, which was initially described by *Prata* [1989]. Regarding the Planck brightness temperatures  $T_\lambda$  of the infrared channels with centered wavelengths  $\lambda$  at  $10.8 \mu\text{m}$  and  $12.0 \mu\text{m}$ , their difference

$$\Delta T = T_{10.8} - T_{12.0} \quad (4.1)$$

appears negative for volcanic ash, while it is generally positive for liquid water and ice clouds. Volcanic ash particles, which mainly consist of silicates, absorb infrared radiation more strongly at shorter wavelengths compared to water and ice particles that absorb more strongly at longer wavelengths (*Pavolonis et al.* [2006]). Prior to that step, the water vapor correction algorithm described by *Yu et al.* [2002] is applied to reduce water vapor absorption effects, which typically accounts for an additional brightness temperature difference of about  $-0.5 \text{ K}$  to  $-1.0 \text{ K}$  (*Prata and Prata* [2012]). Due to calibration uncertainties, field-of-view misalignments and mixed pixel effects, the ash pixel criterion  $\Delta T < 0 \text{ K}$  can be selected within the range  $-0.5 \text{ K} < \Delta T < 0.5 \text{ K}$  (*Prata and Grant* [2001]).

In the next step, the brightness temperatures  $T_{10.8}$  and  $T_{12.0}$  are inverted with a radiative transfer model (*Wen and Rose* [1994]) to determine the effective particle radius and optical depths. Therefore, several specific assumptions have to be made (*Wen and Rose* [1994]; *Prata and Grant* [2001]; *Prata and Kerkmann* [2007]; *Prata and Prata* [2012]):

- The volcanic ash particle shape is spherical, such that Mie theory can be applied for the calculation of the efficiency extinction factor  $Q_{ext} = \sigma_{ext}/(\pi r^2)$ . Here,  $\sigma_{ext}$  denotes the extinction cross section and  $r$  is the particle radius.
- For the Mie calculations, a volcanic ash refractive index has to be estimated, which depends on the observation wavelength  $\lambda$  and the particles' composition.
- The volcanic ash composition is siliceous and the volcanic ash has a density of  $2600 \text{ kg m}^{-3}$ .
- The particle sizes are approximated using the modified- $\gamma$  and log-normal size distributions. Within each pixel, the particle size distribution is uniform and monodisperse.
- The volcanic ash cloud is uniform and plane parallel and it has a geometrical thickness  $L$ .
- The surface temperature  $T_s$  and the cloud top temperature  $T_c$  are generally chosen within some discrete intervals.
- The radiation is isotropic and absorption, transmission and scattering of radiation between the satellite and the ash cloud layer are neglected.

In consequence, the observed radiance per pixel  $I_i$  can be determined via

$$I_i = (1 - R_i(r_e, \tau))B(T_c) + t_i(r_e, \tau)(B(T_s) - B(T_c)), \quad (4.2)$$

where  $R_i$  is the reflectivity of each ash containing pixel,  $B$  is the Planck function and  $t_i$  is the transmissivity of the clouds. The effective radius  $r_e$  of the particles of the size distribution  $n(r)$  is described by

$$r_e = \frac{\int \pi r^3 n(r) dr}{\int \pi r^2 n(r) dr}. \quad (4.3)$$

The size distribution and the effective radius dependent on the particle radius  $r$ . The infrared optical depth  $\tau(\lambda)$  is derived using up to 16 scattering angles upwards from the ash cloud, such that

$$\tau(\lambda) = \pi L \int_0^\infty r^2 Q_{ext}(\lambda, r) n(r) dr. \quad (4.4)$$

Finally, the total mass loading of volcanic ash  $M_l$  within the atmospheric column of the observed pixel can be directly obtained from

$$M_l = \frac{4}{3} \rho \frac{r_e \tau(\lambda)}{Q_{ext}(\lambda, r_e)}. \quad (4.5)$$

The sensitivity study by *Wen and Rose* [1994] assesses the errors of the column ash mass loading to be between 40 % and 60 % due to the uncertainties of the numerous assumptions. In addition, the retrieval algorithm is preferentially sensitive to volcanic ash particles with diameters between  $2 \mu\text{m}$  and  $32 \mu\text{m}$  (*Stohl et al.* [2011]), and the lower boundary of the detection limit is about  $0.2 \text{ g m}^{-2}$  (*Prata and Prata* [2012]).

Other investigations have aimed to obtain more robust volcanic ash concentration retrievals from infrared measurements: *Francis et al.* [2012] and *Dubuisson et al.* [2014] include the information of a third SEVIRI channel in their algorithms, while *Pavolonis et al.* [2006] find that, in comparison to the two wavelength approach, the algorithm is more sensitive to the presence of volcanic ash using four channels at  $0.65 \mu\text{m}$ ,  $3.75 \mu\text{m}$ ,  $11.0 \mu\text{m}$ , and  $12.0 \mu\text{m}$ . This method even includes mitigation effects of underlying water and ice clouds (see also *Pavolonis et al.* [2013]). *Millington et al.* [2012] and *Kylling et al.* [2015] apply coupled systems of a radiative transfer model combined with the Lagrangian volcanic ash dispersion models NAME and FLEXPART, respectively. Investigations on the characteristics of highly irregular and porous volcanic ash particles in the context of infrared optical properties were performed by *Kylling et al.* [2014]. They demonstrate that larger particles are detectable in case of irregular shapes compared to mass equivalent spheres. Additionally, retrievals with spherical particles appear to underestimate column mass loadings in contrast to the retrievals assuming morphologically complex inhomogeneous ash particles. *Clarisse et al.* [2010] developed an algorithm based on correlation coefficients for the application of hyperspectral sounders such as IASI (Infrared Atmospheric Sounding Interferometer). Within this study, an upgraded version of the data set described by *Stohl et al.* [2011] and *Prata and Prata* [2012] is provided and used (*F. Prata, personal communication,*



**Figure 4.2:** MSG-SEVIRI's total field of view and the area of the retrieved volcanic ash data set, which is encompassed by red boundaries.

28 Oct. 2015). It contains volcanic ash cloud observations of the Eyjafjallajökull eruption in April and May 2010. The data is stored in NetCDF (Network Common Data Form) files. The retrieval area encompasses the very northern part of SEVIRI's field of view, which is pictured in Figure 4.2. The red bordered region of the data set stretches from 40°N to 70°N and from 60°W to 60°E. The spatial resolution of the data is given by a grid of  $0.1^\circ \times 0.1^\circ$ . The data is averaged over hourly intervals. The retrieved quantities include the total atmospheric volcanic ash column mass loadings in  $\text{g m}^{-2}$  and the corresponding absolute error, as well as the effective particle radii in  $\mu\text{m}$ , and the unitless infrared optical depth of the volcanic particles. Only pixels containing volcanic ash have retrieval values. This implies that there is no available information if volcanic ash occurrence could be ruled out as the observation is performed during clear sky conditions, or if the retrieval failed due to cloud coverage or similar incidents. This fact proved challenging in data assimilation.

### 4.1.3 Advantages and disadvantages

Using volcanic ash observations from SEVIRI for assimilation-based distribution analysis has different advantages and disadvantages. A significant advantage is the information about the horizontal extension of the volcanic ash cloud, which is provided by the satellite imagery. SEVIRI gives the unprecedented advantage of frequently observing the same region every 15 minutes. In this way, the ash transport and distribution is constantly tracked in detail within the instrument's field of view. Even if the data set used for this work is time-averaged to hourly time steps, these observation intervals are still small compared to observations from polar orbiting satellite sensors, which often have repeat cycles of one to ten days. Furthermore, observing in the infrared spectral range allows for volcanic ash detection during

day and night, while instruments detecting in the ultraviolet or visible range are restricted to day time observations.

On the downside, observing only the horizontal distribution of volcanic ash leads to the challenge in inverse modeling of reconstructing the vertical position and structure of the volcanic cloud. The detection of volcanic ash infrared signatures from space is limited to pixels clear of water clouds. In particular, if meteorological clouds are above the volcanic ash, the signal of ash is attenuated. Overshooting cloud tops, high water vapor burden, instrument noise, and very cold scenes can also lead to negative brightness temperature differences (*Prata and Grant [2001]*). On the other hand, very dense ash clouds or eruption plumes, which often include water or ice, generally result in positive brightness temperature differences. Observing mineral-based aerosol such as mineral dust, or even sampling pixels with sandy or silty ground surfaces under clear sky conditions, can induce false volcanic ash detection.

The numerous assumptions that act as input to the retrieval algorithm, might imply large uncertainties and lead to significant over- or underestimations of the retrieved quantities. The detection limit of  $0.2 \text{ g m}^{-2}$  and the clear sky requirement cause a downsizing of the information content, meaning that there is less data available compared to the number of observed pixels. The missing values of zero volcanic ash content cause a particular problem to the assimilation and analysis of volcanic ash dispersion. It is difficult to correct incorrectly emitted ash of the background simulation, if there is no information about certain ash free areas.

## 4.2 CALIOP

Observations performed by active remote sensing lidar instruments especially profit from vertically resolved information about the structure of aerosol layers within the atmosphere. Therefore, retrievals from the satellite-borne CALIOP are selected for this study. Here, the objective also regards aerosol detection with a special focus on the identification of volcanic ash.

### 4.2.1 Instrumentation and measurement configuration

The Cloud-Aerosol Lidar with Orthogonal Polarization (CALIOP) is mounted on board the Cloud-Aerosol Lidar and Infrared Pathfinder Satellite Observation (CALIPSO, *Winker et al. [2009]*) satellite, which is part of NASA's (National Aeronautics and Space Administration) A-train (Afternoon Train, *Stephens et al. [2002]*). The A-train describes a constellation of polar orbiting satellites, which circle the Earth successively flying at an altitude of 705 km. The sun-synchronous orbit has an inclination of  $98.2^\circ$  towards the equator, such that global coverage is provided between  $82^\circ\text{N}$  and  $82^\circ\text{S}$ . Successive orbits have a longitudinal offset by 2752 km at the equator. Each circuit takes about 98.9 minutes, meaning that the satellites fly 14.6 orbits per day. The resulting repeat cycle with less than  $\pm 10$  km cross-track shift is conducted every 16 days. During daytime passes the satellites cross the equator northbound at 1:30 p.m. local time, with a relative ground speed of  $6.7 \text{ km s}^{-1}$ . Due to the special

flight configuration of the A-train satellites, all observed regions of the atmosphere and the Earth's surface are monitored by different instruments within a very short time frame. Hence, the same areas are observed in different spectral ranges, so that the information content obtained by the sum of measurements is particularly comprehensive.

The CALIPSO satellite (Figure 4.3) was launched in April 2006 and was developed in collaboration with the French space agency CNES (Centre National d'Études Spatiales). Besides the active CALIOP instrument, CALIPSO carries two passive remote sensors: the Imaging Infrared Radiometer (IIR) is an imager with three channels and the Wide Field Camera (WFC) is a visible sensor. Both instruments view nadir with swaths centered on CALIOP's footprint. In this way, this satellite provides unique measurements to improve the understanding of the role of clouds and aerosols in the climate system (*Winker et al.* [2003]).

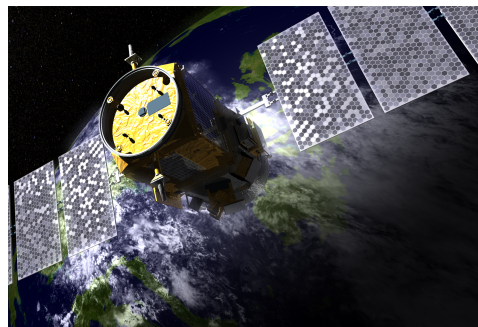


**Figure 4.3:** Artist's view of the CALIPSO satellite in space (source: NASA [2005]).

CALIOP (*Winker et al.* [2007; 2009]; *Hunt et al.* [2009]) is a continuously operating LIght Detection And Ranging (lidar) instrument, constructed around a solid-state neodymium-doped yttrium aluminum garnet (Nd:YAG) laser. It simultaneously transmits co-aligned pulses of 532 nm and 1064 nm wavelengths nadir pointing with an angle of  $0.3^\circ$  in forward direction. Each laser pulse is about 20 ns long and comprises 110 mJ of energy. The pulse repetition frequency amounts to 20.2 Hz. Due to small angular divergence, the beam has a diameter of approximately 70 m at the Earth's surface and the footprints are resolved every 333 m along CALIPSO's ground track.

The laser beams are transmitted as linearly polarized signals into the atmosphere. Therein, they are scattered and absorbed by molecules, cloud particles, and aerosols. The receiver detects the part of the signal that is scattered back with an angle of  $180^\circ$  towards the satellite. The full backscattered intensity is measured by an avalanche photodiode at 1064 nm, while at 532 nm, two orthogonally polarized components (parallel and perpendicular) of the backscattered signal are measured by photomultiplier tubes. The vertical distribution of clouds, aerosols and molecules is derived via the run time  $t$  between sending and receiving of the laser pulse. The distance  $r$  to the scattering objects can be obtained by

$$r = \frac{\delta t \cdot c}{2}, \quad (4.6)$$

where the signal travels with velocity of light  $c$ . Depending on the altitude and the measuring wavelength, the data is resolved differently: regarding the troposphere, the lidar signal at 532 nm has a vertical resolution of 30 m in the lower 8.2 km and 60 m between 8.2 km and 20.2 km. The 1064 nm measurements are resolved by 60 m

intervals extending to 20.2 km height.

Thus, CALIOP is able to capture the full range of molecular, aerosol, and cloud backscattering, which spans five orders of magnitude. In the following section, the focus is placed on the detection of aerosols with the objective to assimilate the retrieved quantities.

#### 4.2.2 Aerosol extinction coefficient retrieval

This study aims to assimilate volcanic ash information from CALIOP elastic backscatter measurements. Therefore, the aerosol extinction coefficient is selected, since it best captures aerosol properties and, at the same time, it is comparable with the modeled quantities. However, as CALIOP is not capable of measuring the aerosol extinction coefficient directly, it can be retrieved as follows. The description proceeds accordant with *Young and Vaughan [2009]*.

The retrieved profiles of particulate extinction coefficients are generated by a fully automated algorithm including three primary modules (*Liu et al. [2009]*). First, the selective, iterated boundary location (SIBYL, *Vaughan et al. [2009]*) algorithm is deployed to retrieve attenuated backscatter data acquired by CALIOP. It identifies the atmospheric layers, which contain clouds and aerosols, and obtains their vertical and horizontal extent. To improve the signal to noise ratio, varying numbers of successive single profiles are averaged. The spatial resolution of these averaged features varies depending on atmospheric regions that are characterized by uniform optical properties and comparable signal strengths. Moreover, within SIBYL high resolution cloud clearing is attained, which mainly discriminates cloud from aerosol layers, and an initial estimate of the 532 nm lidar ratio is accomplished (*Young [1995]*). The lidar ratio describes the relation of proportion of the extinction coefficient  $\alpha$  and the backscatter coefficient  $\beta$  within a defined air volume as

$$S = \frac{\alpha}{\beta}. \quad (4.7)$$

The coefficients express the efficiency of removing photons from the electromagnetic beam by simple scattering, or by the combination of scattering and absorption, respectively.

The hybrid extinction retrieval algorithm (HERA, *Young and Vaughan [2009]*) retrieves the particulate extinction and backscatter coefficients frequently interacting with the scene classification algorithm (SCA, *Liu et al. [2009]*). The intensity of the received backscattered signal  $P(r)$  at the measurement wavelength is described by the lidar equation

$$P(r) = C_{sys} \frac{\beta_m(r) + \beta_a(r)}{r^2} T_m^2(0, r) T_{O_3}^2(0, r) T_a^2(0, r). \quad (4.8)$$

Here, the system constant  $C_{sys}$  includes different parameters describing characteristics of the individual lidar instrumentation, such as the laser energy and lidar calibration coefficients. The backscatter coefficients are dependent on the wavelength and distance  $r$  to the observed object. They are composed of a molecular contribution,

indicated by the subscript  $m$ , and an aerosol contribution, which is denoted by the subscript  $a$ .  $T_m^2(0, r)$ ,  $T_{O_3}^2(0, r)$ , and  $T_a^2(0, r)$  depict the transmission of the probed volume, which the laser signal passes in two directions, due to molecular, ozone and aerosol absorption. The two-way transmission is generally defined as

$$T_i^2(0, r) = \exp\left(-2\eta_i(r) \int_0^r \alpha_i(r') dr'\right), \quad (4.9)$$

where  $i$  denotes the transmission effects of either molecules, ozone, or aerosols. The multiple scattering parameterization  $\eta_i(r)$  is neglected for molecular and ozone transmittance, while for aerosols it is calculated by SCA. The ozone absorption effects and the molecular number density of the observed profiles are obtained and contributed from the NASA Global Modeling and Assimilation Office (GMAO).

HERA considers multiple scattering by particles, such that the CALIOP aerosol extinction retrieval proceeds iteratively. Therefore, Equation (4.8) is rearranged to depict the attenuated backscatter profile

$$\beta'(0, r) = (\beta_m(r) + \beta_a(r))T_m^2(0, r)T_a^2(0, r) = \frac{P(r)r^2}{C_{sys}T_{O_3}^2(0, r)}, \quad (4.10)$$

which is only dependent on atmospheric quantities. These profiles are now corrected for the attenuation between the satellite, where  $r = 0$  and the first atmospheric layer to be analyzed at  $r_N$ . Thus, the aerosol backscatter coefficient at range  $r$  can be determined by

$$\beta_a(r) = \frac{\beta'_N(r)}{T_m^2(r_N, r)T_a^2(r_N, r)} - \beta_m(r), \quad (4.11)$$

with  $\beta'_N(r)$  denoting the renormalized attenuated backscatter that can be calculated by the profile solver within HERA. According to the Equations (4.9) and (4.7), the aerosol transmittance includes  $\beta_a(r)$ , since

$$T_a^2(r_N, r) = \exp\left(-2\eta_a(r)S_a \int_{r_N}^r \beta_a(r') dr'\right). \quad (4.12)$$

HERA solves Equation (4.11) iteratively with a Newton-Raphson algorithm. If divergence is detected within this algorithm, the profile solver algorithm is restarted with a modified lidar ratio, which is selected by the SCA (*Omar et al.* [2009]). The extinction coefficient of the first aerosol layer is finally determined using the extinction to backscatter relation of Equation (4.7). All underlying atmospheric regions are further analyzed by updating the renormalized attenuated backscatter  $\beta'_N(r)$ , by dividing the attenuated backscatter data by the retrieved two-way transmittance and by rerunning the iterative profile solver. In this way, the analysis of the full laser path to the ground is performed.

The retrieved profiles of particulate extinction coefficients are included in the CALIOP level 2 aerosol profile product and available at NASA's Atmospheric Science Data Center (*CALIPSO Science Team* [2016]). Within this work, data products of version 4.1 are applied, while the focus is placed on the retrieval received from the observations with 532 nm wavelength. The horizontal resolution of the profile data is 5 km, while

the vertical resolution covers 60 m sectors. Besides the extinction coefficient profiles in  $\text{km}^{-1}$ , the backscatter coefficients in  $\text{km}^{-1} \text{sr}^{-1}$  are used to calculate the lidar ratio, and consequently identify the aerosol layers that are most likely to contain volcanic ash. According to *Ansmann et al.* [2010], the lidar ratio of volcanic ash varies between 50 sr and 65 sr. *Winker et al.* [2012] stated that the automatic classification algorithms often classify volcanic ash as either mineral dust or ice clouds, which are characterized by lidar ratios of 40 sr or lower (*Omar et al.* [2009]). Thus for the data assimilation experiments, all extinction coefficients that are characterized by a lidar ratio between 40 sr and 60 sr are selected for the analysis. This data selection implies that non volcanic aerosol layers might impair the analysis, but also that there is no observational information provided to the assimilation algorithm about missing observations, clear air conditions, aerosol or cloud layers that do not contain volcanic ash.

### 4.2.3 Advantages and disadvantages

Lidar measurements have the unique advantage of resolving the vertical structure of the atmosphere with full details. Regarding the horizontal direction, CALIOP also shows good resolution along the flight track. In fact, lidar is the only remote sensing observation technique that is able to obtain high resolution profiles of aerosols (*Winker et al.* [2009]). With its high sensitivity to aerosol, CALIOP can detect even tenuous aerosol layers (*Winker et al.* [2012]). Moreover, observations of aerosol layers above bright surfaces such as bright meteorological clouds, snow or deserts, are not problematic for CALIOP, but these are very difficult for passive remote sensing instruments. Lidar signals can penetrate high optically thin clouds and due to the viewing position from space, CALIOP measurements are less affected by cloud attenuation, which favorably appears due to optically thick clouds in lower altitudes. Measuring the depolarization of the backscattered signal, CALIOP is even able to discriminate between liquid and ice water phase as well as between cloud and aerosol. As an active remote sensing instrument, lidar provides its own illumination, such that observations can be taken over the full globe during day and night time. The data sets provided by the NASA Langley Research Center are generally freely available in near real time, such that the data would be well applicable for the analysis of an ongoing volcanic eruption. The utilized CALIOP data of aerosol extinction coefficients is also easily transferable to other aerosol events, as long there is certain information about the aerosol species given.

On the other hand, CALIOP has the following disadvantages: CALIOP's near-nadir, pencil line viewing field limits the coverage of regional scale significantly. Flying in an polar orbit reduces the availability of data for a specific region even more. The European continent counts hardly more than four CALIPSO passes per day. Further, the lidar signal is affected by noise. Especially during day time, the sunlight contaminates the return signals of the lidar. In addition, molecular scattering appears as noise in between the stronger aerosol and cloud signals and therefore must be filtered out for aerosol analyses. The observation of lower atmospheric regions can be limited due to the extinction of the transmitted lidar signal by very

dense clouds. All involved retrieval algorithms have the disadvantage of requiring estimations, assumptions and compromises, that must be made in order to obtain a fully automatic retrieval sequence. For a discussion of these limitations see *Vaughan et al.* [2009], *Liu et al.* [2009], *Young and Vaughan* [2009], and *Omar et al.* [2009].

*Winker et al.* [2012] investigated the performance of CALIOP at observing the transported volcanic ash during the Eyjafjallajökull eruption in April 2010. They discussed the following difficulties of detecting volcanic ash: 1) Most of the ash plumes were transported in mid-tropospheric regions such that the distinction between ash layers and cirrus or desert dust was challenging. 2) Both cirrus and desert dust are typical for these atmospheric regions and they have similar scattering behaviors to volcanic ash. 3) The volcanic ash acts as CCN and IN. And 4) Close to the Eyjafjallajökull, the ash plume was mixed with condensate water from the phreatic eruption. Due to these issues, the identification of volcanic ash is hardly realizable in these cases.



## 5 | Modelling system

For the experiments performed in this study, two data assimilation systems are applied. The 4D-var version of the EUROpean Air pollution Dispersion – Inverse Model (EURAD-IM) is used to investigate the observability on the basis of initial value optimization analyses. Additional experiments including the estimation and improvement of emission factors by the Ensemble for Stochastic Integration of Atmospheric Simulations (ESIAS-chem) are evaluated in order to examine the observability with a state of the art ensemble system, regarding a reasonable stochastic representation of the simulated events. This chapter introduces the model system and briefly describes the data assimilation features of ESIAS-chem.

### 5.1 EURAD-IM

The EUROpean Air pollution Dispersion model (EURAD, *Hass [1991]; Ebel et al. [1997]*) with its Inverse Model (IM, *Elbern et al. [1997]; Elbern and Schmidt [2002]; Elbern et al. [2007]*) extension is an Eulerian state of the art chemistry transport model (CTM), including 3D-var and 4D-var data assimilation. It computes the advection, diffusion, chemical transformation, wet and dry deposition, and sedimentation of tropospheric trace gases and aerosols. From its beginning, EURAD-IM was applied in several studies on air pollution. Later examples include *Marécal et al. [2015]*, *Monteiro et al. [2013]*, and *Huijnen et al. [2010]*.

Figure 5.1 illustrates all principal components of the EURAD-IM in a flow diagram. At the top, the input information is shown, including the meteorological and chemical initial and boundary conditions, emission rates, and observations. The meteorological driver of the model system that provides the meteorological state evolution, is the non-hydrostatic Weather Research and Forecasting model (WRF, *Skamarock et al. [2008]*) with the Advanced Research WRF (ARW) solver. The EURAD Emission Model (EEM, *Memmesheimer et al. [1991]*) allocates fields with anthropogenic emission data, based on the TNO (Nederlandse Organisatie voor toegepast-natuurwetenschappelijk onderzoek) emission inventories. The variability of emissions due to seasonal or daily cycles is incorporated in the EEM output. However, the emissions of unexpected events are generated by specific modules, simulating the emissions during volcanic eruptions, wildfires and mineral dust events. The observations are prepared by the data preprocessor PREP. It collects all kind of measurements from the original observational data files and gathers this information in one file with a standard file format. This is then provided to the assimilation system. All atmospheric

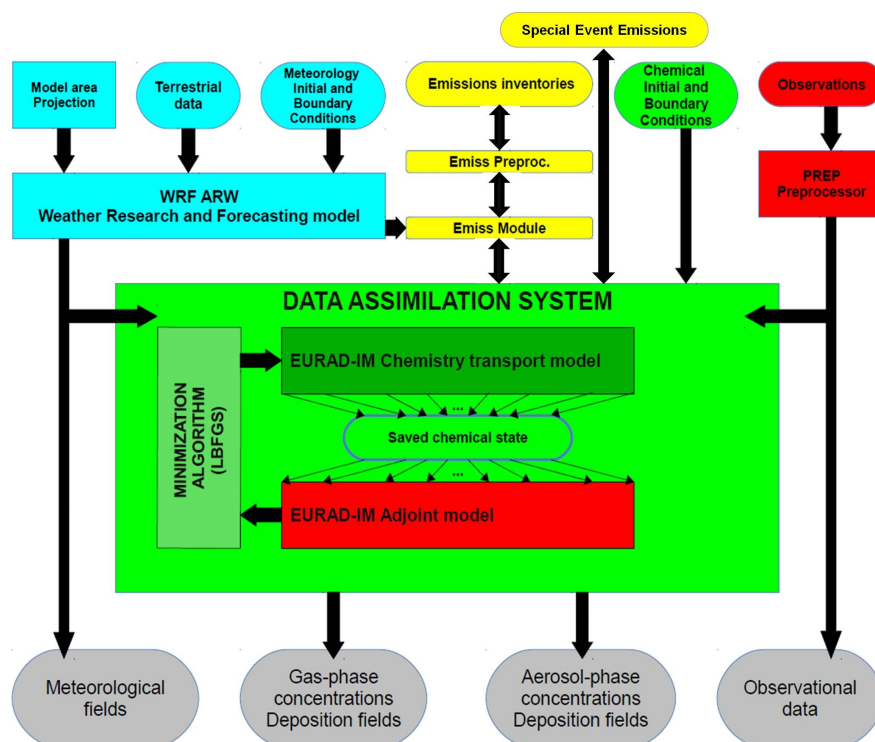


**Figure 5.1:** Flow chart of the EURAD-IM model system with a propagation direction from the top, starting with the model input, to the bottom, where the model output is depicted. The different model parts and their contributors are illustrated in different colors: the meteorological driver in cyan, the emission module in yellow, the chemistry and aerosol part in green, observation affected components in red, and the model output in gray. All input contributions enclosed in rounded boxes contain input data from external providers, whereas modules in rectangular boxes represent parts of the model that are controllable by the user.

chemistry and aerosol related parts of EURAD-IM are illustrated in green. The 4D-var assimilation system consists of the forward CTM and the adjoint model, which contains adjoint operators for transport and diffusion (*Elbern et al.* [2000]), adjoint gas phase mechanisms (*Strunk* [2006]), and the adjoint scheme of the secondary inorganic aerosol formation (*Nieradzik* [2011]). Moreover, there are several observation operators implemented in a forward and an adjoint representation. For minimization, the Limited-memory Broyden-Fletcher-Goldfarb-Shanno algorithm (L-BFGS, *Liu and Nocedal* [1989]) is applied. Finally, the model system provides fields of meteorology, trace gas and aerosol concentrations, as well as observations as output (gray). In the following paragraphs, the EURAD-IM components, which are of importance to this thesis, are described in more detail.

### The chemistry transport

The CTM computes the transport, diffusion, and reactions of up to 109 gaseous species. There are approximately 160 chemical reactions implemented in the model. In order to reduce systematic biases, the state vector is updated to employ a

symmetric operator splitting method (*McRae et al.* [1982]), when stepping from one time step  $t$  to the next  $t + \Delta t$ . With  $T$  denoting the transport operator,  $D$  being the diffusion operator, and  $C$  describing the chemical transformations including the parameterizations of emission sources and deposition processes, the integration of the model state reads

$$\mathbf{x}(t + \Delta t) = T_h T_v D_v C D_v T_v T_h \mathbf{x}(t). \quad (5.1)$$

The indices  $h$  and  $v$  indicate the direction of the computed fluxes, either in the horizontal or in the vertical orientation. Consequently, transport and diffusion are processed every half time step. For advection, there are different schemes available, from which the Walcek scheme (*Walcek* [2000]) is applied in this thesis. As gas phase mechanism RACM-MIM (combined Regional Atmospheric Chemistry Mechanism – Mainz Isoprene Mechanism, *Geiger et al.* [2003]) is taken.

### The aerosol representation in MADE

The Modal Aerosol Dynamics model for Europe (MADE, *Ackermann* [1997]; *Ackermann et al.* [1998]) simulates the aerosol dynamics for EURAD-IM. The chemical and physical transformations of altogether 40 independent aerosol variables are processed, including primary and secondary aerosols. These are, for example, mineral dust, sea salt and volcanic ash, as well as secondary aerosols. The latter are split in inorganic particles, including sulfate and ammonium, and organic aerosols, developing from aromates, alkanes, isoprenes or  $\alpha$ -pinene. The formation of secondary organic aerosols is simulated by the updated version of SORGAM (Secondary Organic Aerosol Model, *Li et al.* [2013]).

The integration of the model state including aerosols proceeds according to Equation (5.1), where  $C$  is extended in the way that the full aerosol dynamics can be calculated. These are described by *Friedlander* [1977] as

$$\begin{aligned} \frac{\partial}{\partial t} n(\nu) = & -\nabla \cdot \mathbf{v}n(\nu) - \nabla \mathbf{c}(\nu)n(\nu) + \nabla(\mathcal{D}\nabla n(\nu)) \\ & + \frac{1}{2} \int_0^\nu \beta(\tilde{\nu}, \nu - \tilde{\nu})n(\tilde{\nu})n(\nu - \tilde{\nu})d\tilde{\nu} - \int_0^\infty \beta(\nu, \tilde{\nu})n(\nu)n(\tilde{\nu})d\tilde{\nu} \\ & + \left. \frac{\partial}{\partial t} n(\nu) \right|_g + \mathcal{J}(\nu)\delta(\nu - \nu_0) + \mathcal{S}(\nu) - \mathcal{R}(\nu), \end{aligned} \quad (5.2)$$

such that the temporal evolution of the particle size distribution  $n(\nu)$  is obtained. Here,  $\nu$  denotes the particle volume,  $\mathbf{v}$  represents the wind vector, and  $\mathbf{c}$  is the particle drift velocity. Further,  $\mathcal{D}$  symbolizes the diffusion coefficient,  $\beta$  describes the coagulation coefficient, and  $\mathcal{J}$  is the nucleation rate. The last four terms of Equation (5.2) include particle growth due to chemical reactions, nucleation, and sources and sinks, respectively.

The aerosol size distribution is represented by three log-normal particle size modes. The log-normal distribution function is defined as

$$n_i(\ln(d_p)) = \frac{N_i}{\sqrt{2\pi} \ln(\sigma_i)} \exp\left(-\frac{(\ln(d_p) - \ln(d_i^{median}))^2}{2 \ln^2(\sigma_i)}\right), \quad (5.3)$$

**Table 5.1:** Standard deviation  $\sigma_i$  and initial median diameter  $d_i^{median}$  for the trimodal log-normal representation of the aerosols in MADE.

Mode	Aitken	Accumulation	Coarse
$\sigma_i$	1.7	2.0	2.2
$d_i^{median}$	0.01	0.07	1.0

where the index  $i$  characterizes one of the three modes. The number concentration is given by  $N_i$ , while  $d_p$  indicates the aerosol diameter. The standard deviation of the particle size distribution  $\sigma_i$ , which is constant for each mode, and the initial median diameter  $d_i^{median}$  of the distribution are listed for the three modes in Table 5.1. The temporal changes of the aerosol size distribution emerge from the shifting of the median diameter along the logarithmic diameter abscissa. The aerosol mass and number concentrations are derivable from the third and zeroth moment of the particle size distribution, respectively.

Within each mode, the aerosols are assumed to be internally mixed. Thereby, any aerosol is characterized by a particle homogeneously assembled of all available mode specific aerosol species, with a composition depending on the percentage of the aerosol type's mass. Consequently, the chemical and physical properties are represented by the average of all contributing components.

### The model domain

EURAD-IM can be operated on different scales, from meso- $\alpha$  to - $\gamma$  scale, following the definitions of *Orlanski* [1975]. It is generally applied to simulate the air quality within the extended European troposphere and higher resolved subdomains by nesting. Here, EURAD-IM uses terrain-following  $\sigma$ -coordinates. These are defined as

$$\sigma = \frac{p - p_t}{p_s - p_t}, \quad (5.4)$$

where  $p$  depicts the model layer pressure,  $p_s$  is the surface pressure, and  $p_t$  the pressure at the model top. The model domain, which is selected for this study's experiments, is described in detail in Section 6.1.

### The volcanic emission module

In EURAD-IM, volcanic emissions are generated in a special volcanic emission module. Information about eruption parameters has to be provided by the user. These include the location of the erupting volcano and its height, the eruption date and time, the plume height as well as the emission strength. The latter information is subdivided into sulfur dioxide and volcanic ash emissions. By means of the chosen vertical mass distribution profile, which can be uniform, poisson, umbrella (*Webley et al.* [2009]), or topheavy (*Webster et al.* [2012]), the emissions are distributed over the model layers between the volcano's summit and the maximum emission height.

All developments and experiments within this thesis are performed with the EURAD-IM model version 5.8.1. Thus, the volcanic ash assigned aerosol variable is **VSOILA**.

The ash dispersion is accordingly simulated with mineral dust coarse mode particles. In the meantime developments of new volcanic ash variables took place, such that with the newest EURAD-IM versions starting from 5.9.1, the simulation of volcanic ash is possible with a distinct coarse mode variable `VASH` and an accumulation mode variable `VASHJ`.

## 5.2 ESIAS-Chem

The Ensemble for Stochastic Integration of Atmospheric Simulations (ESIAS) couples the novel model implementations of ESIAS-met (*Berndt [2018]*), which is an ensemble version of WRF, and ESIAS-chem (*Franke [2018]*), which includes an ensemble setup of EURAD-IM. The coupling is accomplished by an ensemble of meteorological field evolution, generated by ESIAS-met, which is input for the chemistry ensemble produced by ESIAS-chem. In this way, the uncertainties of the driving meteorological fields can be represented in the atmospheric chemistry forecasts or analyses. ESIAS is designed to provide short and medium range probabilistic weather forecasts for renewable energy assessments regarding wind and solar energy, and near real time probabilistic analysis for emission parameter estimations in case of special aerosol events.

Within this thesis, only the atmospheric chemistry partition is applied. Thus, the focus is placed on the system description of ESIAS-chem. ESIAS-chem is an extension to the EURAD-IM system that acts as an environment enabling the model to run in stochastic integration mode in large to ultra-large ensemble sizes, and hence provides the requirements for nonlinear ensemble-based data assimilation. It remains flexible in integrating different modules or methods. A special focus of this study is the application of the ESIAS-chem particle smoother data assimilation algorithm to investigate volcanic ash emission parameters. Therefore, the volcanic ash dispersion ensemble is initialized with distinct volcanic ash emission packages, which are characterized by constant mass injections over a defined height and time interval. Consequently, the cost function that needs to be minimized to find the optimal combination of the emission packages results in

$$J(\mathbf{a}) = \sum_{i=1}^N (H\tilde{M}_i(\mathbf{a}_i[\mathbf{z}]\mathbf{e}_0) - \mathbf{y}_i)^T \mathbf{R}^{-1} (H\tilde{M}_i(\mathbf{a}_i[\mathbf{z}]\mathbf{e}_0) - \mathbf{y}_i) + \mathbf{a}^T \mathbf{K}^{-1} \mathbf{a}. \quad (5.5)$$

Here,  $\tilde{M}_i$  denotes the source receptor model, which maps the a priori emissions  $\mathbf{e}_0$  to the model state and transports the resulting concentrations to the place of observations  $\mathbf{y}_i$ . The profile of emission factors is given by  $\mathbf{a}_i[\mathbf{z}]$ , where  $\mathbf{z}$  is the vector of model level heights. The particle smoother is combined with a discrete ensemble extension of the Nelder-Mead minimization algorithm (*Nelder and Mead [1965]*). This method enables the temporal and vertical resolution of the volcanic emission strength. The filtering step of the particle smoother is realized by evaluating the weights  $w$  of each ensemble member  $i$  that are obtained by

$$w_i = \frac{\tilde{w}_i}{\sum_{j=1}^{N_{em}} \tilde{w}_j}, \quad \tilde{w}_i = \left( \frac{N_{em}}{J(\mathbf{a})} \right)^{0.7}. \quad (5.6)$$

With respect to the weights, the particle smoother scales the variance of the ensemble in the way that the analysis provides the best estimate of emission profiles. Therefore, the system takes advantage of the separation of the volcanic ash emissions due to the wind shear. For more information about the ESIAS-chem system see *Franke* [2018].

## 6 | Developments

In the framework of this thesis, several new modules are developed in the assimilation system of EURAD-IM and thoroughly tested. First, this chapter addresses the design of a new model domain, which aims to make the most efficient use of computational resources in the selected case studies. Hereafter, this chapter briefly summarizes the main implementations that are acquired, in order to facilitate the assimilation of the selected satellite-borne remote sensing data. The contribution of this work to ESIAS in connection with the question of observability is then resumed.

### 6.1 Model domain

For the performed experiments simulating ash dispersion related to the Eyjafjallajökull eruption in April 2010, a new model domain is prepared. This development is necessary because of two reasons: on the one hand, the domain size is optimized to save computational costs, while on the other hand, the vertical grid is adjusted to a finer resolution in the main area of interest of the mid troposphere. Figure 6.1 illustrates the horizontal extent of the model domain and the vertical grid structure. The model domain covers Europe from Southern France, Northern Italy to Romania at the southern boundary, expanding to Northern Scandinavia at the northern boundary, and extending from the West Atlantic to Western Russia and Ukraine in the west to east direction. The location of the Eyjafjallajökull volcano is indicated by the red triangle.

The projection used for this model domain is the Lambert conformal conic projection, which is centered at  $58.0^{\circ}\text{N}$  and  $8.5^{\circ}\text{W}$ . In total, it contains 213 grid cells in the longitudinal direction and 185 grid cells in the latitudinal direction, each with a width of  $15\text{ km} \times 15\text{ km}$ .

Vertically, the atmosphere is subdivided in 23 layers, defined by terrain following sigma coordinates between the surface and 100 hPa, which corresponds to approximately 16 km altitude. For the volcanic ash event, the levels are distributed so that mid-tropospheric model layers have a thickness of less than 1 km. Since in nature, the volcanic ash is usually transported in plumes with small vertical expansion (*Schumann et al.* [2011]), this setup aims to keep the discretization error and numerical diffusion preferably low.

All simulations including both forecasts and analyses, are performed with a temporal resolution of 300 s. However, all results are written out in hourly values, such that the evaluation is accomplished on this basis.

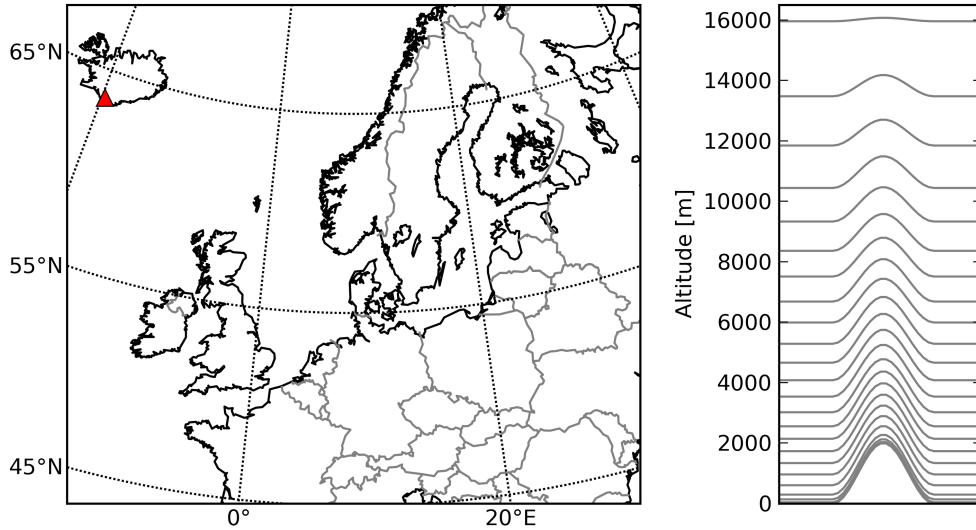


**Figure 6.1:** The selected EURAD-IM model domain (left) including North-West and Central Europe, has a horizontal resolution of  $15\text{ km} \times 15\text{ km}$ . The location of the Eyjafjallajökull is indicated by the red triangle. The mean vertical grid resolution (right) illustrates the terrain following discretization in 23 layers.

## 6.2 The SEVIRI observation operator

In order to assimilate ash column mass loading data retrieved from SEVIRI infrared measurements, the data must be treated to be readable and processable by EURAD-IM. This is carried out with new implementations in the preprocessing module PREP. At first, the available SEVIRI data is reduced to a data set including only retrievals of areas within the model domain. Furthermore, this subset is subject to a quality control eliminating all retrieval pixels with an ash mass lower than  $0.1\text{ g m}^{-2}$  or negative error values. This selection is reasonable, since the mass threshold is below the SEVIRI detection limit and negative values are based on algorithmic inaccuracies of the retrieval algorithm (*F. Prata, personal communication, 20 Jul. 2015*). The conversion to the required data format completes the preprocessing of SEVIRI data.

In data assimilation, the comparison between the model state and the observations is enabled by the observation operator. It maps the 3D distributed model state variable of volcanic ash concentrations  $\mathbf{x}^{ash}$  in  $\mu\text{g m}^{-3}$  to the observation space at each observation time. The SEVIRI data is retrieved in the dimension of integrated column mass loadings  $\mathbf{y}_S$  in  $\text{g m}^{-2}$ . Therefore, the individual model equivalent  $\mathbf{H}_S(\mathbf{x}_i^{ash})$  for each grid cell  $i$  is determined by

$$\mathbf{H}_S(\mathbf{x}_i^{ash}) = 10^6 \sum_{k=1}^{N_{lev}} x_{i,k}^{ash} \Delta z_{i,k}. \quad (6.1)$$

Here,  $\Delta z_{i,k}$  depicts the vertical layer extent of each level  $k$ , where  $N_{lev}$  is the maximum number of model layers. The factor  $10^6$  ensures the mapping of units from  $\mu\text{g}$  to  $\text{g}$ . To determine the observational costs, all  $j$  observations within one model grid cell are compared with the correspondent model equivalent by taking the individual difference  $y_{S,j} - \mathbf{H}_S(\mathbf{x}_i^{ash})$ , which is the observation increment.

The gradient of the cost function with respect to the initial time  $t_0$  is obtained by using the adjoint model. This also implies the necessity of an adjoint observation operator that maps the weighted observation increments described by  $\delta \mathbf{y}_S^{*(w)} = \mathbf{R}_S^{-1}(\mathbf{d}(t) - \mathbf{H}_S \mathbf{M}_t \delta \mathbf{x}^{ash}(t))$  (see Equation (3.7)) from observation space back to the model space. Hereby in this work, the superscript *ash* is omitted for the sake of convenience. Therefore, the classical derivation of the adjoint (Kalnay [2003]) of Equation (6.1) results in

$$\begin{aligned} \delta \mathbf{x}_{i,k}^* &= \delta \mathbf{x}_{i,k}^* + 10^6 \Delta z_{i,k} \delta \mathbf{y}_{S;j}^{*(w)} \quad , \quad k = 1, \dots, N_{lev} \\ \delta \mathbf{y}_{S;j}^{*(w)} &= 0. \end{aligned} \tag{6.2}$$

The superscript ( $w$ ) denotes the weighting through the observation errors by multiplying the inverse SEVIRI observation error covariance matrix  $\mathbf{R}_S^{-1}$ . Applying Equation (6.2) for the conversion from observation space in model space, the multiplication with the layer thickness  $\Delta z_{i,k}$  provokes a vertical redistribution of the volcanic ash in the way, that the upper layers with large vertical extent receive high adjoint changes of ash concentrations, while the low shallow model layers are supplied with low adjoint changes of ash amounts. This is inconsistent with the natural distribution of volcanic ash in the atmosphere, which is generally transported within plumes of low vertical extent, and finally a consequence of an insufficient vertical resolution, which is dictated by computational limits.

Since the SEVIRI data set does not provide further information about the vertical distribution of volcanic ash, this information must now be gained from the model simulations. Therefore, the adjoint observation operator is modified to redistribute the volcanic ash according to the current modeled ash distribution by adding a weighting factor  $\omega_{i,k}$  to the first equation of Equation (6.2) such that

$$\delta \mathbf{x}_{i,k}^* = \delta \mathbf{x}_{i,k}^* + 10^6 \Delta z_{i,k} \omega_{i,k} \delta \mathbf{y}_{S;j}^{*(w)}. \tag{6.3}$$

The weighting factor  $\omega_{i,k}$  for each level  $k$  is determined by a model thickness dependent Gaussian distribution and the proportion of the modeled ash content of the individual grid box in relation to the complete vertical ash concentration profile. To sustain consistency in terms of the order of magnitude, the adjoint increment is normalized to the column value of the classical adjoint calculations.

### 6.3 The CALIOP observation operator

Since the assimilation of CALIOP data is newly introduced to EURAD-IM by this thesis's project, adequate preprocessing is accomplished. The global CALIOP data sets include retrievals of satellite paths reaching from ground to 30 km in altitude. The

preprocessor reduces the data set to data, which are included in the 3D extension of the model domain. Quality assurance is carried out by selecting only those extinction coefficients that are characterized by positive values, where the related backscatter coefficients are positive, and as described in Section 4.2.2 where the corresponding lidar ratios are between 40 sr and 60 sr. The resulting aerosol extinction profiles are then provided to the EURAD-IM assimilation system.

The design of the observation operator mapping the model state of volcanic ash to the dimension of the retrieved CALIOP aerosol extinction profiles in  $\text{km}^{-1}$  is based on the statement of *Ansmann et al.* [2012], that one way to retrieve estimations of volcanic ash mass concentrations as a function of height is to assume mass specific extinction coefficients. Their inverse is also known as the mass-extinction conversion factor. It describes a linear relationship between the extinction coefficient  $\alpha$  and the mass of the observed aerosol  $m$  by  $\text{g m}^{-3}$  by

$$\eta = \frac{m}{\alpha}, \quad (6.4)$$

where  $\eta$  denotes the mass-extinction conversion factor in  $\text{g m}^{-2}$ . During the Eyjafjallajökull eruption in 2010, *Gasteiger et al.* [2011] obtained a mass-extinction conversion factor of  $1.45 \text{ g m}^{-2}$  using lidar observations at 532 nm detection wavelength. This appraisal is in good agreement with the corresponding average of other studies (*Ansmann et al.* [2012]). The CALIOP observation operator  $\mathbf{H}_C(\mathbf{x}_{i,k})$  is consequently defined as

$$\mathbf{H}_C(\mathbf{x}_{i,k}) = 10^3 \frac{\mathbf{x}_{i,k}}{1.45}, \quad (6.5)$$

where  $10^3$  ensures the conversion of the units from  $\text{km}^{-1}$  in  $\text{m}^{-1}$ . The index  $i$  indicates the grid cell and  $k$  denotes the model layer, where extinction coefficient retrievals are available. Since the vertical and horizontal resolution of the CALIOP retrievals  $\mathbf{y}_C$  is higher than the model resolution, the observational costs are obtained by adding the individual differences of each retrieved extinction coefficient compared to the corresponding model grid cell with  $\sum_j \sum_l y_{C;j,l} - \mathbf{H}_C(\mathbf{x}_{i,k})$ . Here,  $j$  is the index of the extinction profiles within the grid cell  $i$ , and the index  $l$  depicts the vertical extinction profile coordinate within a model layer  $k$ .

The adjoint CALIOP observation operator is applied to the observation increments  $\delta \mathbf{y}_C^{*(w)} = \mathbf{R}_C^{-1}(\mathbf{d}(t) - \mathbf{H}_C \mathbf{M}_t \delta \mathbf{x}(t))$ , where the inverse CALIOP background error covariance matrix  $\mathbf{R}_C^{-1}$  acts as a weighting. Accordingly, the adjoint of Equation (6.5) is composed of

$$\begin{aligned} \delta \mathbf{x}_{i,k}^* &= \delta \mathbf{x}_{i,k}^* + \frac{10^3}{1.45} \delta \mathbf{y}_{C;j,l}^{*(w)} \quad \text{and} \\ \delta \mathbf{y}_{C;j,l}^{*(w)} &= 0. \end{aligned} \quad (6.6)$$

Here,  $\delta \mathbf{x}_{i,k}^*$  and  $\delta \mathbf{y}_{C;j,l}^{*(w)}$  denote the adjoint variables that are transported backward in time to determine the gradient of the cost function at the initial time.

## 6.4 Observability analysis with ESIAS

ESIAS-chem, the ensemble environment of EURAD-IM computes all simulations with the selected domain properties. The developments described above for the forward observation operators are adopted to the particle smoother algorithm of ESIAS-chem. This data assimilation technique is characterized as adjoint-free, such that the adjoint observation operator implementations are not needed. Here, the vertical distribution of the volcanic ash relies only on the information gained by vertical wind shear of horizontal winds.

This work applies ESIAS-chem in order to analyze the observability of transported volcanic ash clouds. The observability of such an event is closely related to its predictability (*Lorenz [1963]*). In the context of atmospheric applications, predictability describes the likelihood of a true atmospheric state to be represented in NWP or CTM modeling and their corresponding ensemble extensions. Since quality controlled observations are considered to be closer to the true atmospheric state, data assimilation constrains the model calculations to a degree depending on the relative errors. Accordingly, observations limit the ensemble performance.

Here, this predictability is exploited to identify regions and patterns of high observability where the volcanic ash concentrations are strongly constrained by any observations within the analysis period. Therefore, the following analysis strategy is developed:

- Dense mass isopleths (lines of equal masses) provide information about areas, where the ensemble predictions coincide, supporting likelihood of reliability.
- The comparison of mass isopleths distributions in the background ensemble run and the analysis ensemble run offers valuable clues on the constraining impact of the observations.
- The ensemble spread, which can be quantified in terms of the standard deviation, provides additional indication of whether the isopleths converge due to constraints imposed by high observability, or due to conforming outliers imposed by high stability (negative Lyapunov exponents).
- The weighted ensemble mean is evaluated with regards to the general qualitative ensemble prediction skills, and hence is accessible for applications with strong interest in reliability such as aviation.

In Chapter 7, plots of mass isopleths are also referred to as 'spaghetti plots'. Besides gaining the pure results of observability, the studies of this work are likewise used for evidence provision of developments in ESIAS.



## 7 | Observability Analyses

For the present work, the eruption of the Eyjafjallajökull volcano during April and May 2010 was selected to be analyzed as a prototype study, since it depicts a unique special aerosol event. The eruption affected nearly the whole of Europe due to a grounding of air traffic for several days in many countries (e. g. *Zehner* [2010], or *Schumann et al.* [2011] referring to EUROCONTROL<sup>1</sup> reports). Moreover, explosive volcanic eruptions are rather exceptional in Europe. Combined with the prevailing weather conditions, the volcanic ash was transported from Iceland to Central Europe and dispersed over the continent (e.g. *Langmann et al.* [2012]). From an assimilation viewpoint, the Eyjafjallajökull eruption is particularly interesting as it was well observed from many different observation platforms. Furthermore, the exemplary investigation of an explosive volcanic eruption is instructive as it poses the challenge of determining highly variable emission terms.

This work focuses on the first eruptive phase of the Eyjafjallajökull. The ash dispersion within the period of 14 April at 00:00 UTC to 00:00 UTC on 18 April is analyzed in detail, since they particularly include the special event characteristics described beforehand. Thus, the developments in observability assessment methodologies are validated for this scenario. Therefore, all 4D-var analyses are executed on the Jülich Research on Exascale Cluster Architectures – JURECA (*Jülich Supercomputing Centre* [2016]) applying the software Stage 2016a, while the ESIAS-chem experiments are computed on the Jülich Blue Gene/Q – JUQUEEN supercomputer (*Jülich Supercomputing Centre* [2015]).

This chapter initially describes the volcanic scenario and the meteorological circumstances, which controlled the ash transport as well as the observation opportunities. Further, the two different ways of ensemble generation are presented and the selected error assumptions are shortly discussed. In total, three different experiments are performed to study the observability of the volcanic ash event. These include first, the analysis of a small ensemble using the EURAD-IM 4D-var algorithm and SEVIRI column mass loading retrievals as observational data. The second experiment investigates the value of assimilating CALIOP aerosol extinction coefficient profiles in addition. Finally, the observability of SEVIRI data within ESIAS-chem is evaluated in a third experiment. The exercised ensemble runs are described, illustrated and analyzed in the sections 7.2, 7.3, and 7.4, respectively.

---

<sup>1</sup>European organisation for the safety of air navigation

## 7.1 General experiment setup

The investigation of the experiments performed in this work requires a detailed understanding of the aerosol emissions, the subsequent transport, as well as the known uncertainties. The following sections describe these conditions and present the similarities and differences between the particular analysis experiments.

### 7.1.1 Aerosol scenario

The Eyjafjallajökull volcano is located in a glacial area at the south coast of Iceland, generally rests below an ice cap with a peak height of 1666 m, and is one of the lesser active Icelandic volcanoes. The previous eruption happened between 1821 and 1823, followed by a long period of rest. Since 1994, enhanced seismic activity and significant crustal deformation were detected in the area around the volcano (*Sigmundsson et al.* [2010]).

On 20 March 2010, the Eyjafjallajökull started to erupt after approximately 190 years of rest. This eruption occurred in a calmer effusive, alkali-basalt releasing style, with fountains of liquid lava and fire that spread hundreds of meters in the air, as well as lava flows that ran down the slopes and canyons of the volcano (*Zehner* [2010]).



**Figure 7.1:** Explosive eruption of the Eyjafjallajökull volcano on 16 April 2010 (source: *Fulle* [2010]).

In the morning of 14 April 2010, the phreatomagmatic eruption of the Eyjafjallajökull started at the central crater (*Gudmundsson et al.* [2012]). The encounter of the hot lava with water of the melted ice cap and surrounding glaciers evoked the immediate expansion and vaporization of the water. An ash plume reaching several thousand meters high was formed, due to small fragments of magma that were accelerated skywards together with water vapor and gases. Volcanic ash was raised in heights of the tropopause and temporarily to altitudes of more than 9 km. Between 14 and 18 April, the explosive eruption phase continued with plume heights pulsating between 5 km and 10 km (*Arason et al.* [2011]). Figure 7.1 illustrates the spatial dimensions such a plume can attain using an example from 16 April 2010. Volcanic activity and therefore the emission strength and emission height reduced between 19 April and 3 May 2010, during which time the eruption gathered strength. Thereafter, a second explosive phase lasted until 20 May, whereupon the emission plume rose again into atmospheric levels of 4-8.5 km altitude. From 20 May on, the eruption changed from being phreatomagmatic to purely magmatic and decreased quite fast (*Keiding and Sigmarsson* [2012]). On 23 May, the Eyjafjallajökull calmed again and remained inactive since then.

### 7.1.2 Meteorological conditions

During the first explosive phase of the Eyjafjallajökull eruption, a well developed high pressure system extending from the surface to high levels was located south of Iceland. Its anticyclonic rotation provoked westerly winds along the south coast of Iceland, such that the volcanic emissions were transported at first towards Scandinavia. This meteorological situation is shown in Figure 7.2, which displays the WRF forecast initialized with the ECMWF analysis on 14 April 2010 (left) and 16 April 2010 (right), both at 12:00 UTC. The geopotential height at 500 hPa is displayed in color map, whereas the sea level surface pressure is indicated by white contours. Above the North Atlantic, the upper flow persisted in a zonal direction over the considered period. A major trough remained above North-East Europe, while the local minimum of the 500 hPa geopotential above Central Europe declined from 14 to 16 April. West of the Iberian Peninsula, a cyclone rested statically and filled slowly until 18 April. A detailed meteorological overview of the complete eruption period between 14 April and 23 May 2010 is given by *Petersen* [2010].

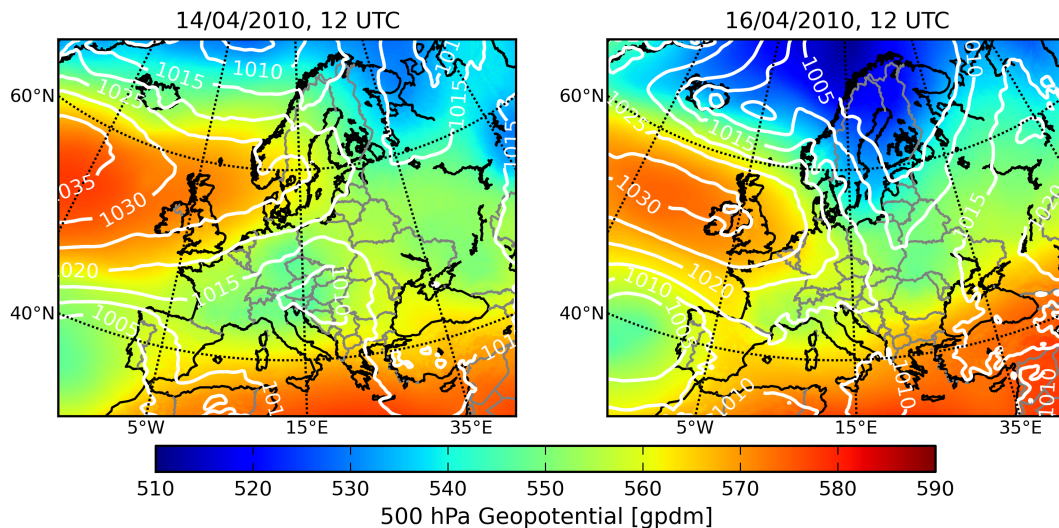


**Figure 7.2:** Meteorological situation in Europe during the Eyjafjallajökull eruption, showing the geopotential height at 500 hPa (color coded) and the sea level surface pressure (white contours), on 14 and 16 April 2010.

Following the flow along the isohypses, the volcanic ash transport pattern featured a dispersion from the southern tip of Iceland, at first east bound – to Norway, and then slightly further south over Scotland and the North Sea towards Central Europe. Two volcanic ash plume branches were established on 15 April, as the ash cloud hit the low pressure area in Central Europe: one, stretching from the North Sea to North Norway, crossed Scandinavia eastwards between 15 and 16 April. The second branch elongated from the west of Ireland to the North Sea, and drifted southwards crossing Great Britain, the Benelux countries, Germany, and France. However, both branches were connected, featuring higher concentrations of volcanic ash in the center and decreasing concentrations towards the edges. Once the volcanic ash plume arrived

over Southern Germany, its southbound trajectory was blocked by the Alps such that the ash was transported around a weak high pressure system above France during 17 and 18 April. The eastern part of the plume was further advected across Eastern Europe. Between 16 and 22 April, the aerosol layer subsided continuously until it descended into the planetary boundary layer, where it mixed with the general boundary layer aerosols.

When considering the observability of the volcanic ash event, the cloud cover must be examined because it strongly affects the observation wealth as discussed in the sections 4.1.3 and 4.2.3. To demonstrate the limitations imposed by the cloud cover of the episode, Figure 7.3 shows true color images from the Moderate-resolution Imaging Spectroradiometer (MODIS) on board the Terra satellite. The daily pictures of the cloud distribution above Europe on 14 to 17 April 2010 (upper left to lower right panel) clearly indicate the potential that the ash mixed with meteorological clouds and that ash observations from space may have interfered with water and ice clouds. The cloud patterns remarkably differ between tenuous and thick, as well as fragmented and widespread. On 14 April, a large gap in the cloud coverage opened above Southern Norway and Sweden, Denmark and Northern Germany, as well as above the North and Baltic Seas. This gap moved eastwards on 15 April arriving at the Baltic states. However, this cloudless area was not penetrated with volcanic ash. Within this period, the ash plume was farther west as it is visible in beige on the image from 15 April, spreading from Iceland towards Southern Norway. Thus, the

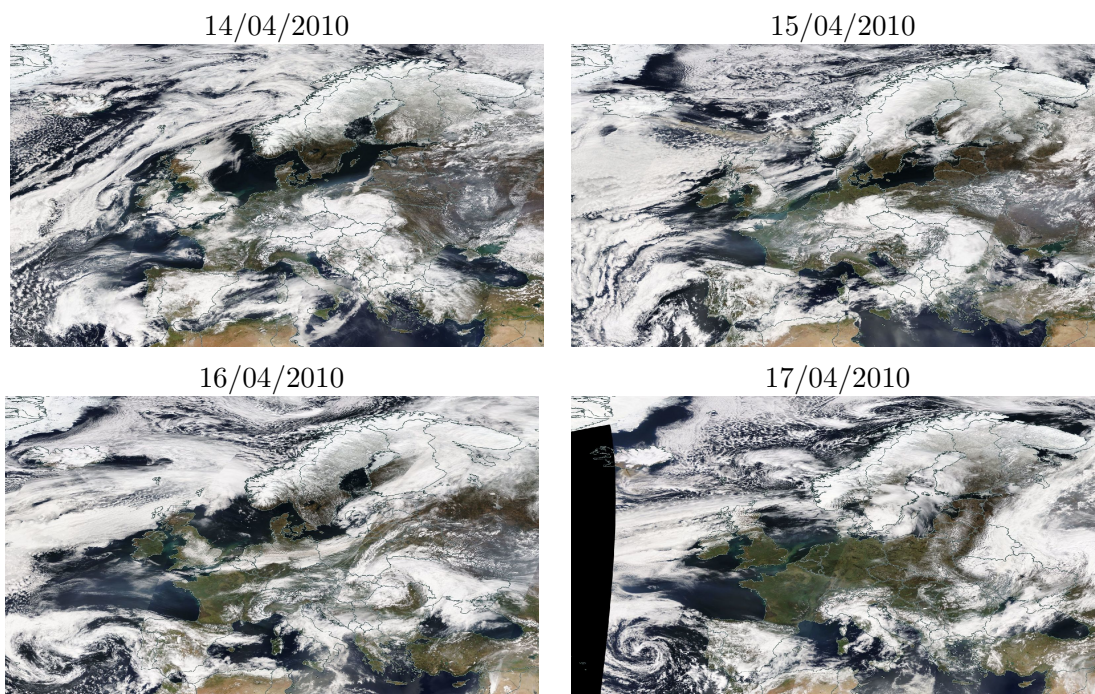


**Figure 7.3:** Cloud cover above Europe during the Eyjafjallajökull eruption illustrated by daily MODIS (Terra) natural color images of morning overpasses from 14 to 17 April 2010 (source: NASA [2010]).

conditions to observe the ash transport above the sea were fairly restricted, due to the widespread cloud cover. From 16 April onward, a new cloud clear region formed over the North Sea and the Bay of Biscay, before enlarging and drifting to England, France, Benelux and Germany on 17 April. The volcanic ash traversed Germany on 16 April, which is depicted on the MODIS image. It appears that the ash interfered with a thin cloud band. On 17 April, the thinning volcanic ash should have been well detectable over West and Central Europe.

### 7.1.3 Ensemble generation

In this study, all ensembles are generated by assigning different volcanic ash emission profiles to the ensemble members. The meteorological fields, which are responsible for the ash dispersion, are assumed to be free of significant errors, such that all ensemble members are driven by the same meteorological WRF forecast.

The ensemble, which is set up for the 4D-var assimilation, is not designed as a conventional ensemble in the classical sense. Rather, it is designed to reflect the highest applicable extent of the eruption scenario. This ensemble consists of nine ensemble members that are chosen to include the potential extremes of the eruption strengths and heights, and possible emissions in between. Hereby, the ensemble does not aim to hold uncertainty representations, which are consistent with the analysis, but to embrace the largest conceivable uncertainties. In all following discussions, this ensemble is referred to as 4D-var ensemble.

Figure 7.4 illustrates the time series of volcanic ash emission profiles, where each time series is assigned to one 4D-var ensemble member and extends from 00:00 UTC on 14 April to 00:00 UTC on 18 April 2010. The emissions of the first ensemble member (EM-1, upper time series) are based on the Keflavík radar emission height observation of *Arason et al.* [2011], and the correspondent mass eruption rates following *Mastin et al.* [2009], who estimate the mass flow  $F_m$  in  $\text{g s}^{-1}$  by

$$F_m = f\rho \left( \frac{h}{2000} \right)^{\frac{1}{0.241}}. \quad (7.1)$$

Here,  $f = 0.02$  denotes the fine ash mass fraction,  $\rho = 2500 \text{ kg m}^{-3}$  is the volcanic ash density, and  $h$  depicts the maximum plume emission height in m. The emissions are vertically distributed assuming a Poisson distribution according to *Webley et al.* [2009]. The emissions are characterized by a very fine temporal resolution of 5 min, with maximum emission heights up to about 10 km. The emission rates of the second ensemble member (EM-2) were estimated by the EURAD-IM modelers of the Rhenish Institute of Environmental Research at University of Cologne in their real time modeling efforts, based on the poor information base in 2010 during the Eyjafjallajökull eruption. Here, the emission heights vary between 6–11 km, wherein the emissions are distributed with a Poisson distribution with a constant total emission rate of  $2.5 \cdot 10^6 \text{ g s}^{-1}$ . The remaining seven ensemble members (EM-3, EM-4, EM-5, EM-6, EM-7, EM-8, and EM-9) are generated with constant maximum emission heights of 14 km, 12 km, 10 km, 8 km, 6 km, 4 km, and 2.5 km. The emission rates are

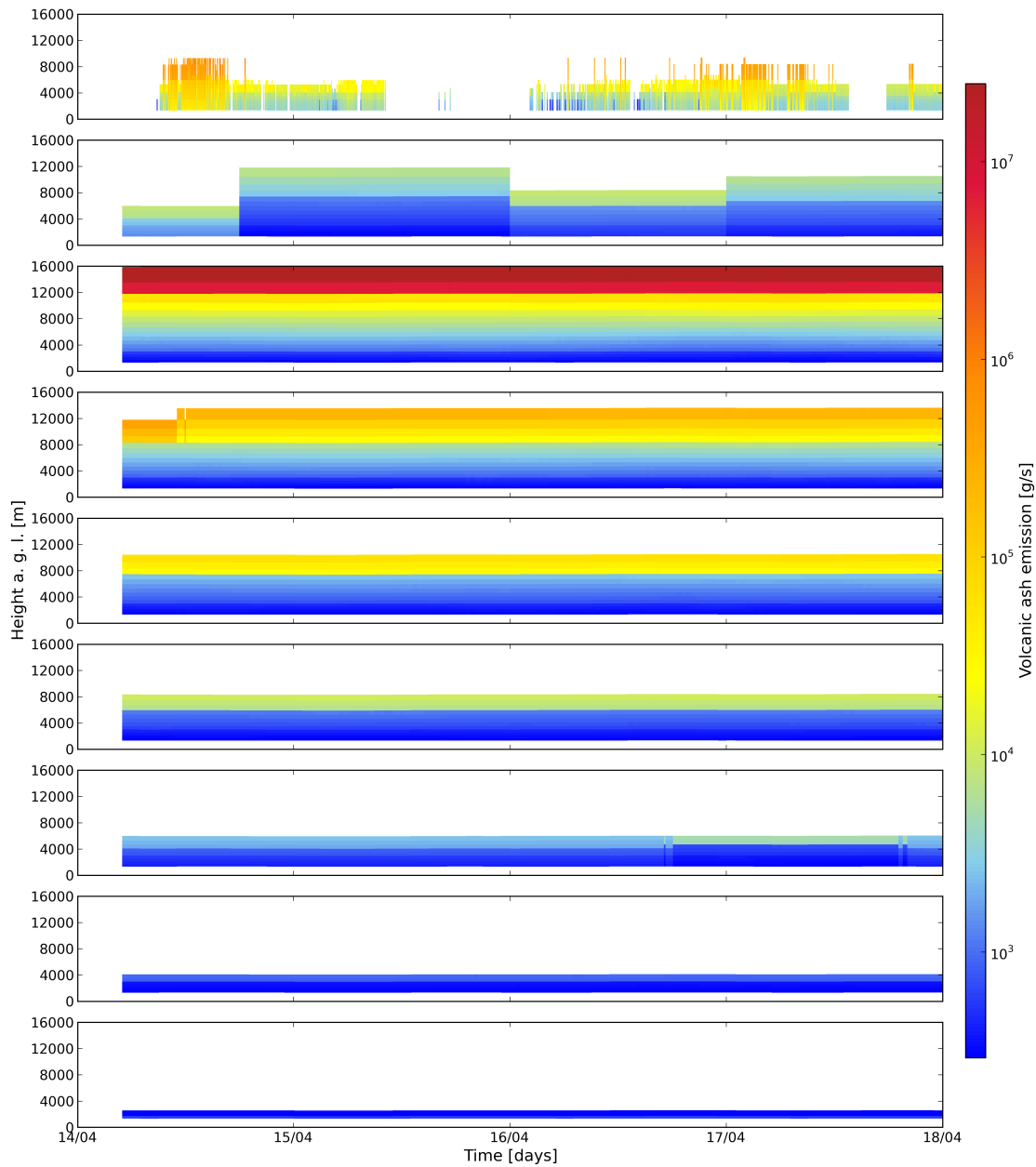


**Figure 7.4:** Volcanic ash emission profiles of all nine ensemble members of the 4D-var ensemble between 14 April, 00:00 UTC to 18 April, 00:00 UTC.

derived using Equation (7.1) and the emissions are vertically assigned applying the Poisson distribution. Here, the small discontinuities in the emission profile time series of ensemble member 4 and 7 are caused by the changing meteorological conditions, interacting with the discrete, yet pressure dependent height levels of the model.

For the observability assessment applying the particle smoother algorithm within ESIAS-chem, the ensemble is generated by selecting an individual a priori emission package for each ensemble member, which constantly emits a normalized a priori ash

concentration of  $100 \mu\text{g cm}^{-3}$ . The ensemble spans 60 ensemble members in total. In the following sections, this ensemble is called particle smoother (PS) ensemble.

For each ensemble member, the emission duration is restricted to a specific three hour interval between 06:00 UTC on 14 April and 12:00 UTC on 15 April. The emission period is chosen to include only this epoch of the Eyjafjallajökull eruption, in order to sustain acceptable computational costs. However, this time span is assured to be reasonable, since the available observations used in the analysis contain observations of ash clouds, which were released during this temporal interval. Each emission package is allocated to one single model layer such that the full ensemble covers all model layers, except the model top layer, during the total emission period.

#### 7.1.4 Error assessment

For the experiments performed with the 4D-var ensemble, observation errors are extensively investigated. Testing results indicate that it is mostly favorable to not rely on the original observation errors, which are included in the data sets. Since the original observation errors are generally close to the order of magnitude of the retrieved value, and while the volcanic ash quantities span over several orders of magnitudes, observations with small observation values and small errors tend to dominate the corrections in the analysis. This is induced by the modality of obtaining the gradient. The weighting with the inverse observation error covariance matrix  $\mathbf{R}^{-1}$  leads to higher weights for smaller errors. Selecting the same error value for all observations revealed the most reliable analysis results.

In the 4D-var ensemble studies, the SEVIRI observation error is estimated to a value of  $0.1 \text{ g m}^{-2}$ , which is in the range of the mean retrieved error value. The CALIOP observation error is estimated to be  $0.1 \text{ km}^{-1}$ . For the PS ensemble analysis, the SEVIRI observation error is only slightly adjusted, to observation errors of  $0.3 \text{ g m}^{-2}$  for ash column mass loading retrievals smaller than  $0.8 \text{ g m}^{-2}$ , and observation errors of  $0.1 \text{ g m}^{-2}$  for all observations of values higher than  $0.8 \text{ g m}^{-2}$ . In this way, slightly higher weights are assigned to higher observation values. To stay with the expressions of classical data assimilation, the term retrieval is here taken synonymously with the term of observation. Two ensemble analyses are performed within the PS ensemble study; one including all available SEVIRI observations, and a second applying only SEVIRI retrievals with values larger than  $0.45 \text{ g m}^{-2}$ . The latter ensemble analysis additionally includes perturbations of the observations  $y_i$  with  $y_i = y_i + 0.75 \cdot dy_i \cdot r_i$ , where  $dy_i$  is the observation error and  $r_i$  depicts a random number.

A background error must be defined for the 4D-var ensemble only, while the cost function applied in the PS ensemble renounces the use of a background error covariance matrix. Where needed, the background errors are chosen to include a minimum error for volcanic ash concentrations of  $750 \mu\text{g m}^{-3}$ . For background concentrations larger than  $375 \mu\text{g m}^{-3}$ , their doubled amount is assigned as background errors. However, for the PS ensemble run using perturbed observations, a background error is applied in order to reduce the variation in the emission factors.

## 7.2 4D-var ensemble using SEVIRI retrievals

This first experiment evaluates the analysis of the Eyjafjallajökull ash dispersion during the period of 14–18 April 2010. Each model run is initialized at 00:00 UTC with a forecast lead time of 24 hours. Thereby, data assimilation windows of 24 hours are chosen as a reasonable compromise between acceptable computational expenditure and sufficient observational information. All available SEVIRI retrievals are incorporated in the 4D-var assimilation algorithm. Since no volcanic ash retrievals are available on 14 April, for that day only forward model runs are performed with the selected emissions in order to obtain adequate initial values for the next day. For the remaining period of 15–17 April, ensemble 4D-var assimilation runs are executed, whereas each ensemble member is initialized by the corresponding analysis of the previous day, taken as first guess. The 4D-var ensemble is restricted to initial value optimization, because emission factor optimization is not computationally feasible due to the long lasting adjoint transport exceeding the defined assimilation window. Hence, under prevailing restrictions, the observational information cannot be used to estimate the true emissions by using the adjoint model.

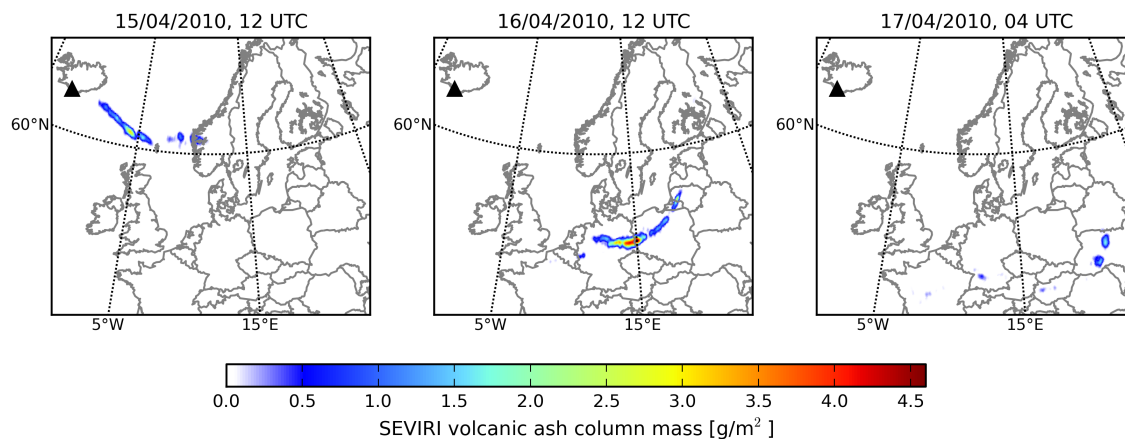


**Figure 7.5:** MSG-SEVIRI volcanic ash column mass loading retrievals of the Eyjafjallajökull 2010 ash plume on 15 April at 12 UTC, 16 April at 12 UTC, and 17 April at 04 UTC (cf. *Prata and Prata [2012]*).

Figure 7.5 illustrates the dispersion of volcanic ash over the European continent as detected by SEVIRI. Retrievals of vertically integrated volcanic ash concentrations are displayed at 12:00 UTC on 15 and 16 April, and at 04:00 UTC on 17 April 2010. During the evaluated period, volcanic ash is generally retrieved within narrow bands of clouds, being transported south-east bound from Iceland to the North Sea and from thereon transversely shifted across Central Europe. Maximum concentrations in volcanic ash column mass of approximately  $4.6 \text{ g m}^{-2}$  are retrieved above the German-Polish boarder region on 16 April around 12:00 UTC. When the volcanic ash reached the Alps in the late evening of 16 April, the observed ash clouds started to break up in steadily thinning cloud patches, which further drifted in west and east

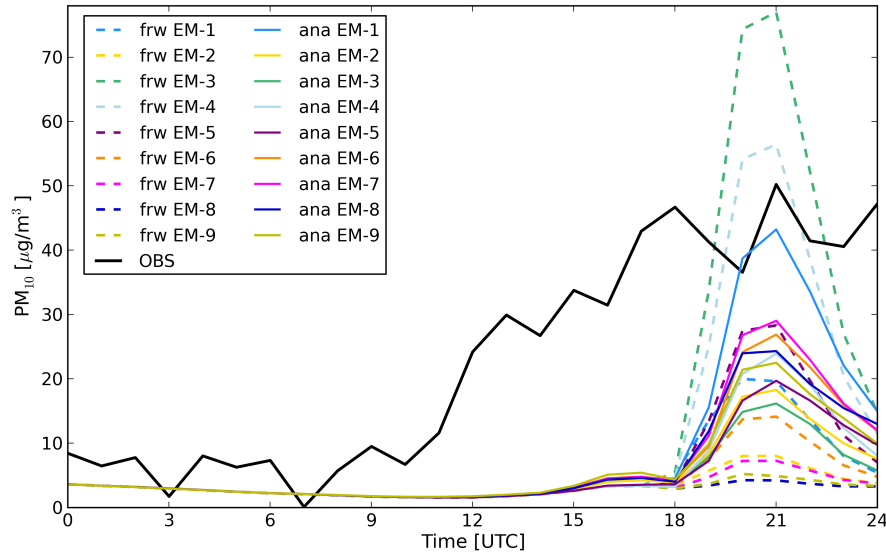


**Figure 7.6:** Comparison of  $PM_{10}$  time series of the 4D-var ensemble first guesses (frw) and analyses (ana) with independent observations (OBS) at Schneefernerhaus (Zugspitze) on 17 April 2010. The analyses are based on the use of SEVIRI retrieval data to optimize the volcanic ash dispersion between 15 and 18 April.

direction. The three graphs of Figure 7.5 are representative of the very limited data available for assimilation, due to the extended cloud cover. Hence, the observability of the first days of the Eyjafjallajökull eruption in 2010 can be considered as constricted. At first, the performance of the different ensemble members and the benefit of data assimilation is investigated. Therefore, validation is performed with independent in situ observations of  $PM_{10}$  concentrations, measured at the environmental research station Schneefernerhaus at  $47.42^{\circ}N$ ,  $10.98^{\circ}E$ , with an elevation of 2650 m a. s. l. at Zugspitze.  $PM_{10}$  refers to all particulate mass contained in aerosols with a diameter of less than  $10\ \mu m$ . Figure 7.6 shows the temporal evolution of measured  $PM_{10}$  concentrations in comparison with  $PM_{10}$  of first guess and analysis for all nine ensemble members on 17 April. The observations depict a distinct increase of  $PM_{10}$  at 11:00 UTC, which is associated with the volcanic ash arrival at Zugspitze. The observations reach a maximum concentration of  $50\ \mu g\ m^{-3}$  at 21:00 UTC. In contrast, the modeled  $PM_{10}$  concentrations start to increase at 18:00 UTC for both the first guesses and the analyses. All simulations feature maximum values between 20:00 UTC and 21:00 UTC, followed by a concentration decline until the end of the day. The assimilation of SEVIRI volcanic ash column mass loadings indicates the discrepancies between first guesses and analyses. While the  $PM_{10}$  concentrations of EM-3, EM-4 and EM-5, which consider the highest and strongest volcanic emissions, are corrected to lower concentrations, the remaining ensemble members are corrected to higher concentrations. Considering the skill of forward modeling only, EM-4 proceeds closest to the maximum values of the observations. However, examining the analyses, EM-1 agrees best with the  $PM_{10}$  measurements.

The assimilation rests on observational information obtained by SEVIRI total column

retrievals, which strongly differ in the spatio-temporal and quantitative volcanic ash assessment from in situ  $PM_{10}$  measurements. The temporal disagreement in the ash arrival between the analysis and the reference observations at Zugspitze reveals the insufficient information content provided by the SEVIRI retrieval. The leading part of the ash cloud that was detected at Schneefernerhaus between 12:00 UTC and 18:00 UTC could either not be observed by SEVIRI due to the prevailing cloud cover or could not be identified as volcanic ash in the retrieval algorithm. An inadequate vertical redistribution of volcanic ash to the model layers by the adjoint observation operator is unlikely. The vertical realignment of the ash is carried out according to the vertical background distribution, whereas the ensemble background includes all possible height levels, such that a compliance with the late ash arrival of all ensemble members is inconsistent. Yet, the assimilation of SEVIRI data reduces the spread among the ensemble members significantly, when regarding the  $PM_{10}$  concentrations. Consequently, a certain constraining impact of the SEVIRI data to the model state is identified.

The impact of the assimilation of SEVIRI data on the horizontal dispersion of vol-

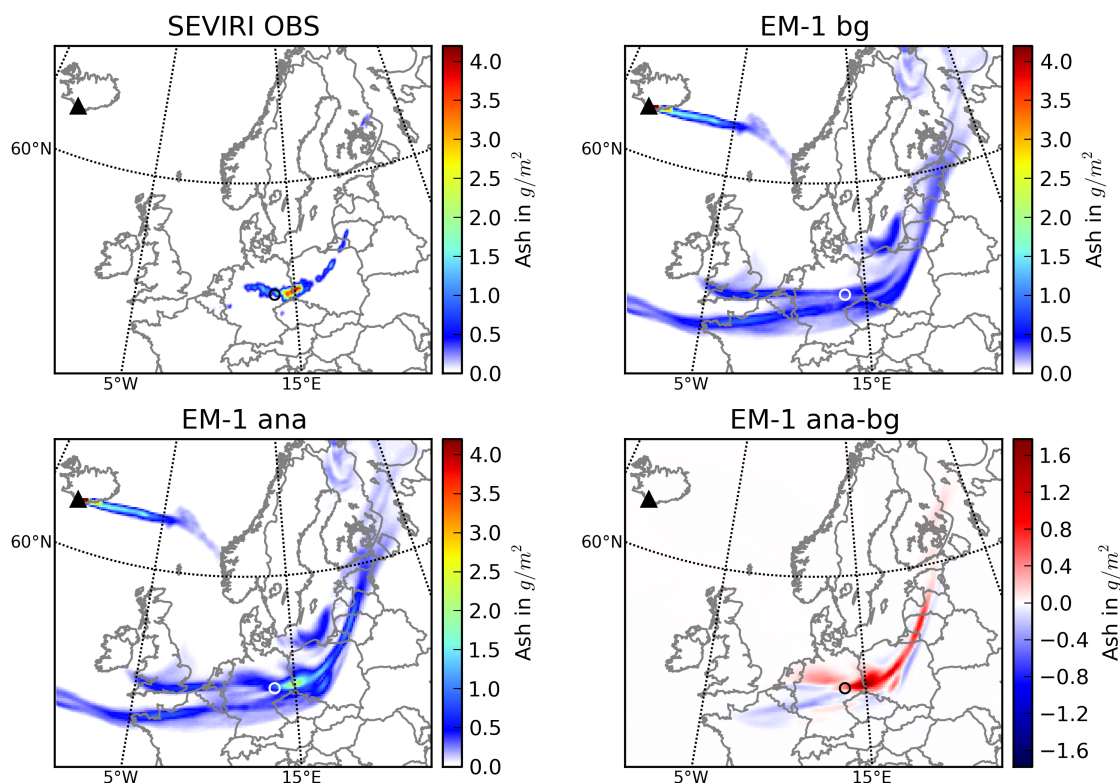


**Figure 7.7:** Horizontal volcanic ash distribution above Europe on 16 April at 13 UTC, as retrieved from SEVIRI observations (upper left), EM-1 background field (upper right), EM-1 analysis field applying 4D-var assimilation of SEVIRI data (lower left), and the analysis increment given by the difference between analysis and background field (lower right). The small circles indicate the location of EARLINET lidar in Leipzig.

canic ash varies significantly among the ensemble members. Figure 7.7 illustrates the horizontal ash distribution above Europe on 16 April at 13:00 UTC. Retrieved volcanic ash column mass loadings from SEVIRI observations depict an ash cloud extending from Central Germany to the southern German-Polish boarder, thinning over Central Poland, the Kaliningrad Oblast to Lithuania. Three tenuous ash signals are retrieved in Western Germany, Western Czech Republic, and Eastern Finland. The analysis results are evaluated by means of EM-1, as it characterizes a suitable representative of all ensemble members. The volcanic ash background distribution of EM-1, also displayed in ash column mass loadings, stretches from the West Atlantic and Southern Great Britain to Poland and northwards to Northern Finland and North-Eastern Russia. Here, the volcanic ash column mass loadings reach at most values of  $1.0 \text{ g m}^{-2}$ . Additionally, a volcanic ash plume is transported from the Eyjafjallajökull across the North Atlantic towards the coast of Norway, where maximum values exceed  $4.0 \text{ g m}^{-2}$  at regions nearby the erupting volcano. The EM-1 volcanic ash mass loading analysis shows a similar ash distribution as described by the background. By data assimilation, the model state is corrected to values between  $1.5 \text{ g m}^{-2}$  and  $2.5 \text{ g m}^{-2}$  in the region of highest observation values. However, the analysis increments allow for a better identification of the areas affected by the assimilation. Positive values of the analysis increments are clearly in compliance with SEVIRI observations of volcanic ash at the considered time. However, observations achieved earlier and later in the assimilation window induce changes in the analysis field in positive as well as negative direction, such as the ash reduction above Northern France. Apparently, the deficient observability of the ash plume above the North Atlantic during the entire day results in uncorrected background knowledge only. Analogous results can be achieved by the corresponding analysis of all other ensemble members (see Figures A.1, A.2, A.3, A.4, A.5, A.6, A.7, and A.8 of Appendix A).

On 16 April, the transit of the Eyjafjallajökull ash plume was well observed by the EARLINET lidar station in Leipzig, Germany (*Ansmann et al.* [2010]). The location of this lidar system at  $51.35^\circ\text{N}$  and  $12.43^\circ\text{E}$  is indicated by the small circle in the images of Figure 7.7. The plume's observability allows for further evaluation of the ensemble and assimilation results. Figure 7.8 shows the modeled vertical ash concentration profiles of the 4D-var ensemble's background and analysis fields at 13:00 UTC. The background simulations of EM-3 and EM-4 contain two elevated ash layers between 2–6 km and 9–13 km, while the formation of the upper ash layer is suppressed in the analysis. Regarding the background states, all nine ensemble members feature ash layers at altitudes varying between 1 km and 6 km and differing in ash concentrations between  $43 \mu\text{g m}^{-3}$  to  $996 \mu\text{g m}^{-3}$ . In the analysis, the ensemble spread decreases, such that eight ensemble members approximately concur that the ash cloud contains its highest concentration at about 2–3 km height. Solely EM-3 exhibits the maximum concentration at 4 km altitude. Furthermore, the range of maximum ash concentrations of all nine ensemble members is reduced to values of  $260 \mu\text{g m}^{-3}$  to  $688 \mu\text{g m}^{-3}$  in the analysis. In addition, Figure 7.8 displays the lidar derived mean backscatter coefficient profiles at 532 nm and 1064 nm, which are averaged over the period from 12:34 UTC to 13:28 UTC. In the case of both

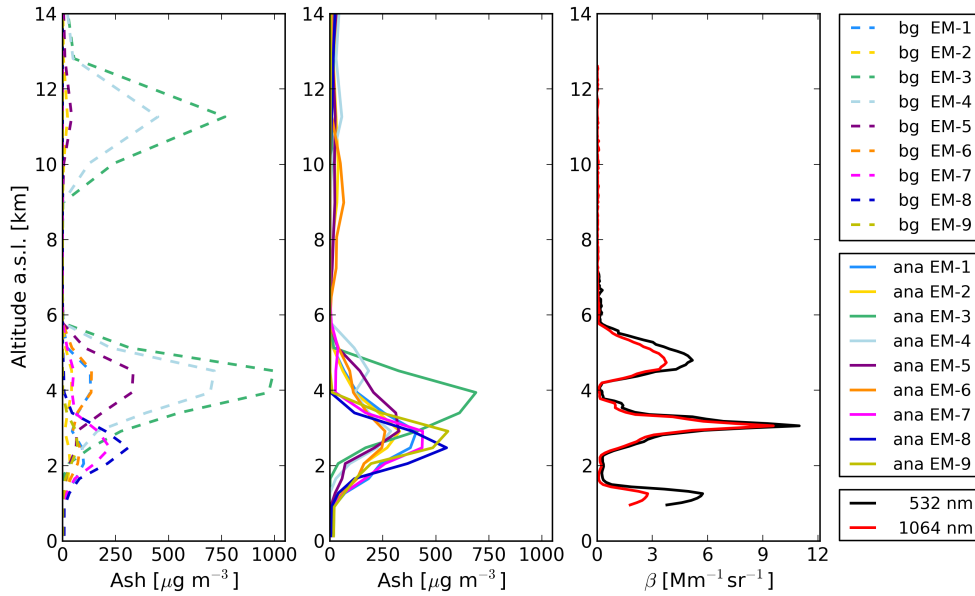


**Figure 7.8:** Vertical volcanic ash distribution over Leipzig on 16 April at 13 UTC: Concentration profiles of the background (left) and analysis (center) fields of the 4D-var ensemble, as well as the lidar retrieved mean backscatter coefficient profiles at 532 nm and 1064 nm of the Leipzig EARLINET station (right). The analyses are based on the use of SEVIRI retrieval data.

wavelengths, two elevated volcanic ash layers are observed at heights of about 3 km and 5 km. The increased signals below 2 km are most likely due to scattering effects of the planetary boundary layer. The comparison of the analysis and lidar profiles supports the conclusion that all nine ensemble members represent the volcanic ash layers in the correct vertical range. Among all ensemble members, EM-4 is in best compliance with the lidar observations, as it exclusively resolves two ash layers at 3 km and 4.4 km altitude.

Figure 7.9 combines the mass column loadings obtained from ensemble forecasts, analyses, three SEVIRI pixels, and lidar measurements for the EARLINET station in Leipzig on 16 April at 13:00 UTC. The bar chart includes the column values from the background and analysis simulations of all nine 4D-var ensemble members, as well as the ensemble mean analysis, the mean of SEVIRI observations, and the mass loading equivalent derived from the EARLINET lidar observations. The latter is computed by transforming the 532 nm lidar backscatter coefficients into the SEVIRI observation space. The background simulations reveal large differences in the column value between the ensemble members. The maximum value of  $3.27 \text{ g m}^{-2}$  corresponds to EM-3, while EM-9 shows the minimum value of  $0.09 \text{ g m}^{-2}$ . The analysis column mass loadings illustrate much better agreement laying between  $0.77 \text{ g m}^{-2}$  (EM-7) and  $1.26 \text{ g m}^{-2}$  (EM-3). The mean column mass loading of all nine ensemble analyses accounts for  $0.89 \text{ g m}^{-2}$ , associated with a standard deviation of  $\pm 0.15 \text{ g m}^{-2}$ . For comparison with observational data, the column mass loading of the SEVIRI retrievals

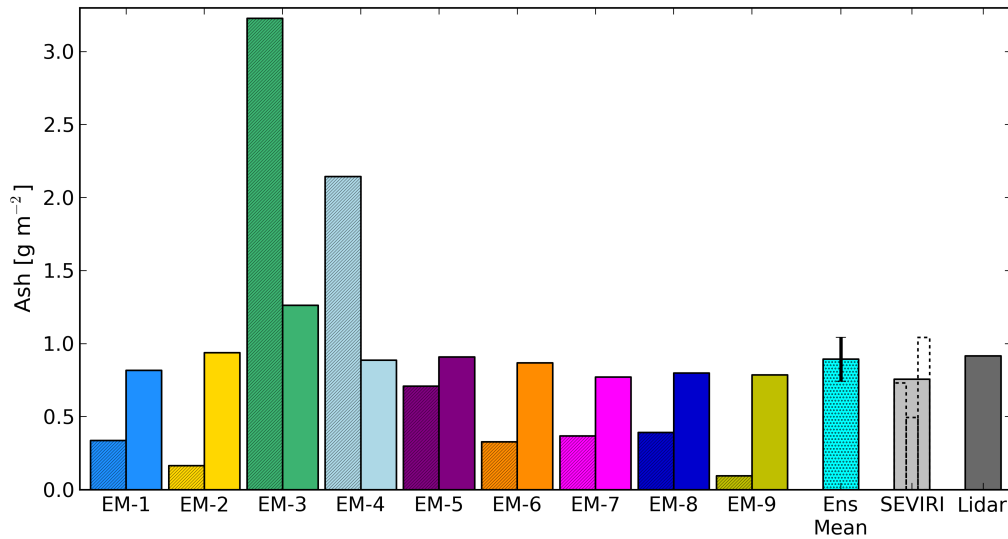


**Figure 7.9:** Volcanic ash column mass loadings at the EARLINET station in Leipzig on 16 April at 13 UTC: background (shaded bars – left) and analysis (clear bars – right) of the 4D-var ensemble, the analysis ensemble mean (Ens Mean, cyan dotted) including the standard deviation (error bar), SEVIRI observation mean (light gray) calculated from three retrieved pixels included in the considered model grid cell (dashed clear bars), and lidar derived mass loading equivalent (dark gray). The analyses are based on the use of SEVIRI retrieval data.

and the column mass loading equivalent of the lidar observations of Figure 7.8 are illustrated. In the EURAD-IM numerical grid cell of 15 km horizontal width, which includes the lidar measurement site, there are three SEVIRI retrieved ash columns. The limited comparability of gridded model data with observations is accounted for in the assimilation by equal weighting. All three SEVIRI retrieved column values are depicted as dashed bars in Figure 7.9 in addition to their mean value. The lidar equivalent volcanic ash column mass loading is calculated by vertically integrating all backscatter coefficients at 532 nm wavelength and following *Groß et al.* [2010], by further converting the integral applying the mass conversion factor of  $1.45 \text{ g m}^{-2}$  and a lidar ratio of 49 sr.

An ideal ensemble prediction system shows a perfect relationship between ensemble spread and ensemble mean error (*Grimt and Mass* [2007]). Regarding the ensemble analysis of volcanic ash column mass loadings, this objective is well fulfilled at least for the evaluation at Leipzig. Here, SEVIRI and lidar derived column values of  $0.76 \text{ g m}^{-2}$  and  $0.92 \text{ g m}^{-2}$ , respectively, lie within the ensemble spread of the 4D-var ensemble analysis. Thereby, the deviations between the mean analysis and observations remain small.

The skill of the assimilation performance depends on three main criteria: Firstly, the tangent linear model must approximate the leading processes, describing the dynamics and transformations in the model sufficiently well. Secondly, the discrepancies between observations and modeled background influence the assimilation achieve-

ments significantly, and thirdly, the minimization of the cost function is notably controlled by the quantity of observational information. Accordingly, the identification of weak ensemble members is not straightforward. This can be explained by the evaluation of the cost function during proceeding iterations. Figure 7.10 illustrates the normalized costs, determined by the ratio of iteration dependent costs and initial costs for the analyses of 15–17 April. The ensemble analysis is satisfactory if the costs are significantly reduced, unless background model states are close to the observations. Comparing the cost evaluation of the three assimilation windows, the ensemble analysis on 16 April appears to be most efficient, as the costs of all ensemble members are reduced by more than 60%. On 15 and 17 April, the minimization algorithms of many ensemble members attain a minimum in less than 20 iterations. Hereby, the costs only decrease by 7–61% of the initial costs. The explicitly successful minimization on 16 April might be linked to the large number of 36 662 column mass loading retrievals. Comparing the ensemble members among each other, EM-3 and EM-4 seem to perform best. However, EM-3 and EM-4 include extremely strong volcanic emissions, such that the disagreement of background state and observations might be particularly strong, which evokes the significant reduction of costs.

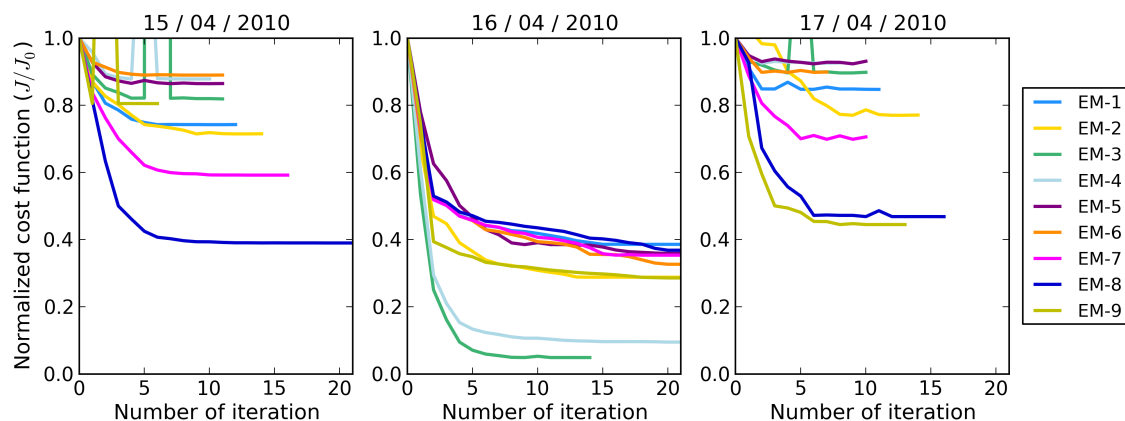


**Figure 7.10:** Iterative evolution of normalized cost function (costs  $J$  divided by the initial background costs  $J_0$ ) for the nine members of the 4D-var ensemble. The observation quantity applied in the analyses on 15 April (left), 16 April (center), and 17 April (right) differ markedly, counting 19 038, 36 662, and 5 768 SEVIRI retrievals within the 24-hours assimilation windows, respectively.

The uncertainty of the volcanic ash cloud position as analyzed by the ensemble spread can be illustrated in spaghetti plots. Figure 7.11 displays spaghetti plots of  $1.0 \text{ g m}^{-2}$  column mass isopleths on 15 April at 12:00 UTC, 16 April at 12:00 UTC, and 17 April at 04:00 UTC, matching the times of the observations illustrated in Figure 7.5. The isopleths of all nine ensemble members are depicted for the first guess and the analysis. The isopleth value is selected, such that a concentration threshold of  $2.0 \text{ mg m}^{-3}$  is exceeded assuming a realistic volcanic ash layer thickness of

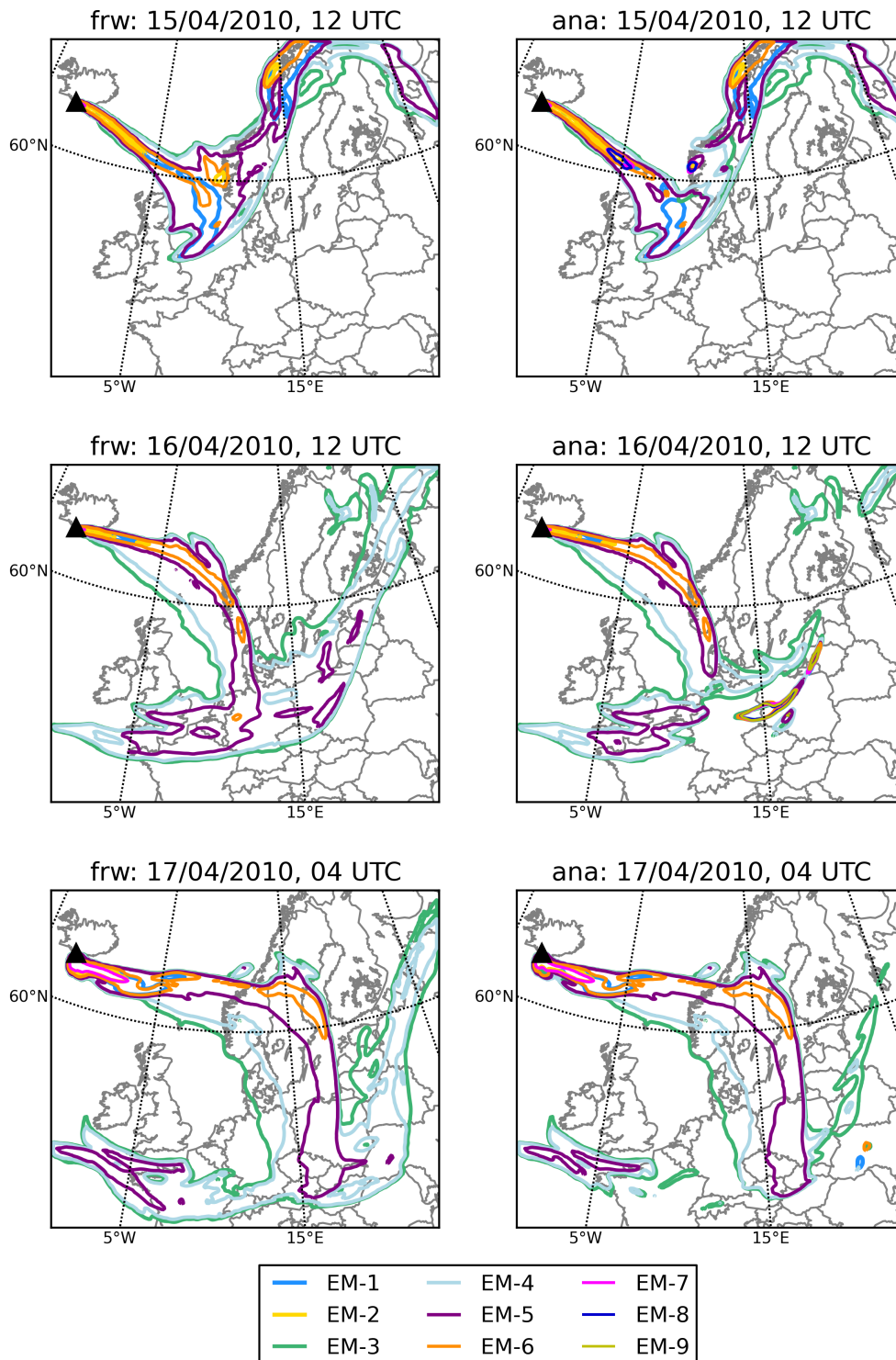


**Figure 7.11:** Spaghetti plots of  $1.0 \text{ g m}^{-2}$  mass isopleths for all nine 4D-var ensemble members: first guess (left column) and analysis (right column) are depicted on 15 April at 12 UTC, 16 April at 12 UTC, and 17 April at 04 UTC. The ensemble analysis is based on the assimilation of SEVIRI data.

500 m (*Schumann et al.* [2011]). The right graphics column of Figure 7.11 shows the corresponding assimilation-based adjustment of the ensemble members towards the observational data. The more the mass isopleths of the different ensemble members conform in their position, the more likely is the exceedance of the threshold. This is the essential fact for the provision of a skillful probabilistic prediction.

All first guess graphics have in common that the mass isopleths spread relatively strong. This originates from the differing emission assumptions of the ensemble members. The graphics are dominated by the spaghetti of EM-3, EM-4, EM-5, and EM-6, while all other ensemble members rarely exceed the threshold value. Assimilating SEVIRI observations, the ensemble analysis reflects the convergence of the ensemble members in regions of high observability. On 15 April at 12:00 UTC, concentrated isopleths are noticed over the North Atlantic, north of Scotland. Above the southern west coast of Norway, a similar effect is visible locally. In contrast to the first guess, the surrounding area is devoid of all ensemble members' isopleths in the analysis. The illustrations for 16 April at 12:00 UTC show a reduction of the EM-3, EM-4, and EM-5 volcanic ash concentrations in the regions of Central to Northern Europe. The area extending from Eastern Germany over Poland towards Latvia is characterized by concentrated mass isopleths of all nine ensemble members, revealing excellent observability. Comparing first guess and analysis ensemble on 17 April at 04:00 UTC, the decrease of areas, where EM-3 and EM-4 include column ash loadings higher than  $1.0 \text{ mg m}^{-3}$ , is predominant over France and Switzerland, as well as in the eastern regions of the model domain. However, there are two local spots of conforming, dense spaghetti occurrence over Western Ukraine, the threshold is not reached by all ensemble members though. All regions without changes between first guess and analysis ensemble are characterized by poor observability and remain uncertain.

Even if the horizontal illustration of spaghetti plots is already beneficial for air traffic advice, the vertical position of dense ash clouds and the position of dangerous ash concentrations are even more essential. The vertical cross section along a path reaching from the north western corner of the domain to Southern Romania is presented in Figure 7.12 for the ensemble first guess and the ensemble analysis on 16 April at 12:00 UTC (also cf. Figure A.18 for the analysis using SEVIRI and CALIOP data). Here, the ash concentration isopleths of  $0.2 \text{ mg m}^{-3}$  and  $2.0 \text{ mg m}^{-3}$  are plotted, corresponding to the limits of the enhanced procedures zone. Volcanic ash concentrations of  $2.0 \text{ mg m}^{-3}$  are solely exceeded by EM-4 and EM-5 and are hardly corrected during the assimilation of SEVIRI data. These high concentrations appear close to the volcano between 1.5 km and 12 km in altitude at about  $63^\circ\text{N}$ , and further south only in altitudes between 10 km and 15 km. Since the  $2.0 \text{ mg m}^{-3}$  threshold is only exceeded by very few ensemble members, and since the analysis does not reveal corrections towards better agreement of the isopleths, it is rather unlikely that the selected threshold value is exceeded. The spaghetti presenting the  $0.2 \text{ mg m}^{-3}$  threshold show strong adjustments due to the assimilation in the region between  $50^\circ\text{N}$  and  $53^\circ\text{N}$ , which corresponds to the German-Polish boarder region. While the first guess ensemble only exhibits the isopleths of five ensemble members between 1.5 km and 7 km, the analysis reveals isopleths of all nine ensemble

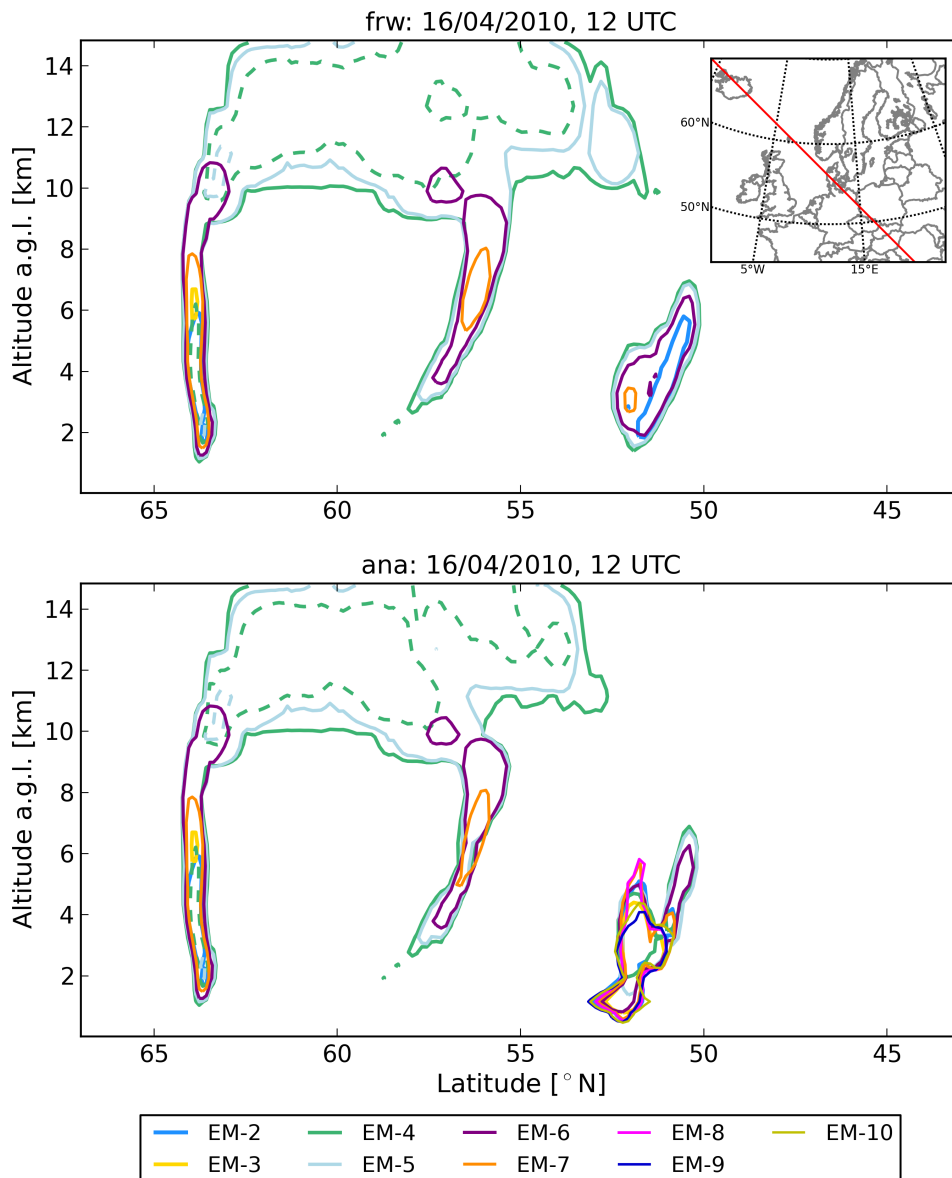


**Figure 7.12:** Spaghetti plots of  $0.2 \text{ mg m}^{-3}$  (solid lines) and  $2.0 \text{ mg m}^{-3}$  (dashed lines) volcanic ash concentration isopleths as vertical cross section for all nine 4D-var ensemble members: first guess (top) and analysis (bottom) on 16 April at 12 UTC are depicted along the red line illustrated in the map inlay of the top panel. The ensemble analysis is based on the assimilation of SEVIRI data.

members in the altitude range of 0.5–7 km. All other regions depicted in these plots demonstrate low observability for increased volcanic ash concentrations, as the spaghetti is not in good agreement.

To conclude the findings of this section, it is emphasized that the assimilation of SEVIRI volcanic ash column mass loadings well imposes constraints to the ensemble.

Despite missing height information in the observational data, the vertical distribution of volcanic ash is forced to height levels in reasonable agreement with lidar based validation data. The agreement of all ensemble members in specific ash concentration values is manifested by good observability of the volcanic ash scenario by the SEVIRI instrument. Consequently, observability determines areas of low uncertainty in the ensemble analysis that are often locally limited to those regions where the volcanic ash retrieval actually provides column mass loading data. More observational information is still desirable for the assimilation, as the analysis remains uncertain in large areas of the model domain. Explicit observational information from SEVIRI on volcanic ash free regions could be especially beneficial for this purpose.

### 7.3 4D-var ensemble using SEVIRI and CALIOP retrievals

The second experiment investigates how the information source of CALIOP aerosol extinction profile data impacts the volcanic ash dispersion ensemble analysis and to what extent it contributes to the observability of the special aerosol event. Therefore, the same scenario is evaluated utilizing the identical first guess ensemble setup and presuming the same analysis condition. The 4D-var assimilation is performed applying SEVIRI and CALIOP data though. In the considered period, there are five CALIPSO overpasses available crossing the model domain. *Winker et al.* [2012] identified all five overpasses to include observations of volcanic ash. Figure 7.13 shows the locations of the CALIPSO ground track under specification of the observation times. Thus, CALIOP observations of one overpass is additionally assimilated within the assimilation window of 15 April, and observations of two overpasses are assimilated for the analyses of 16–17 April, respectively.

The new ensemble analysis is evaluated in terms of the  $PM_{10}$  concentrations at Schneefernerhaus. Primarily, Figure 7.14 shows the same temporal  $PM_{10}$  evolution graphs as pictured in Figure 7.6. However here, the 4D-var ensemble analysis additionally includes the observational information of CALIOP retrievals. Regarding the comparison with the independent observations at Zugspitze, the amplitudes of the analyzed volcanic ash arrival are not improved compared to the ensemble analysis using SEVIRI data only. Generally, the temporal evolution of the ensemble analysis  $PM_{10}$  concentrations remains unsatisfying. The  $PM_{10}$  concentrations of the ensemble analysis is slightly increased compared to the ensemble first guess between 00:00 UTC and 18:00 UTC. However, the assimilated CALIOP aerosol extinction profiles did not observe the leading part of the ash cloud, apparently. Two aspects might be responsible: firstly, the CALIPSO overpasses did not cross this volcanic ash cloud, or secondly, the identification of the ash layer was impossible by reasons of the prevailing cloud cover. Nevertheless, the spread of the ensemble analysis decreases. This is traced back to an intensified constraining impact of the additionally exploited CALIOP data and consequently to an enhanced observability using CALIOP and SEVIRI data.

Figure 7.15 depicts the volcanic ash column mass loading background, analysis, and

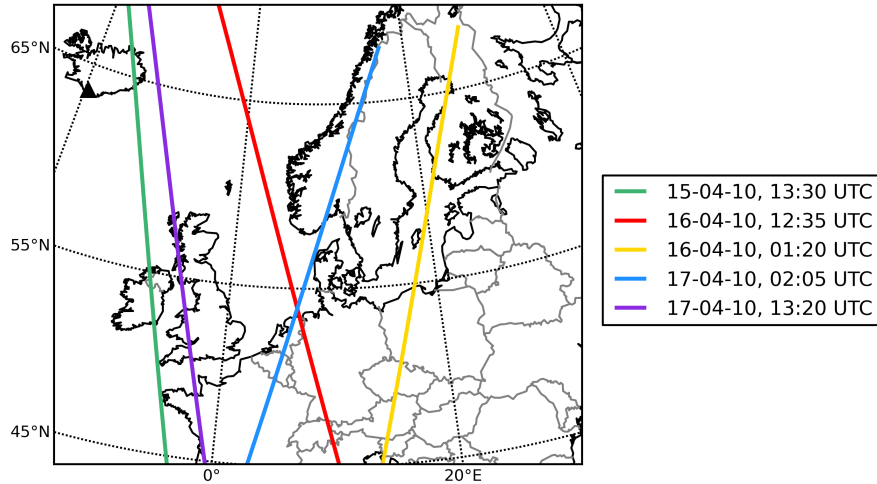


**Figure 7.13:** CALIPSO ground tracks of all available overpasses in the model domain between 15 and 17 April 2010. The aerosol extinction profiles of these observations are assimilated in the second 4D-var ensemble experiment.

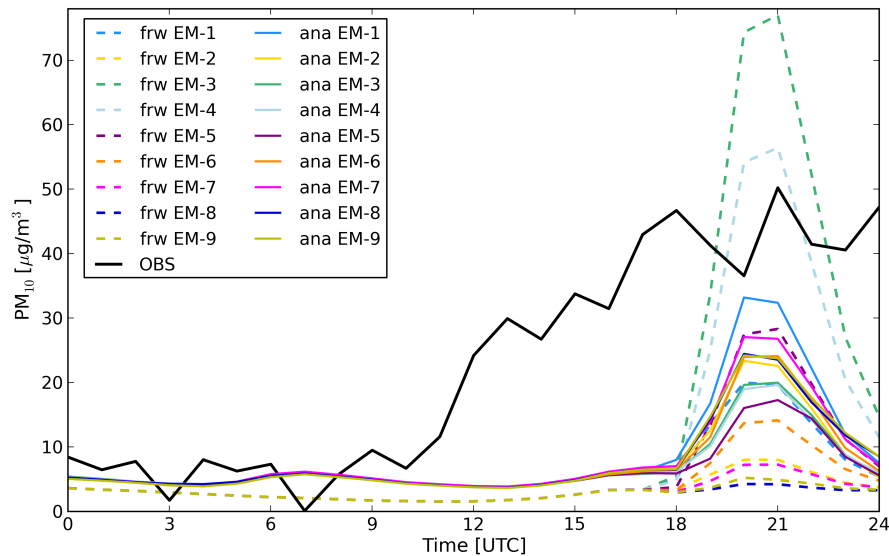


**Figure 7.14:** Comparison of  $PM_{10}$  time series of the 4D-var ensemble first guesses and analyses with independent observations at Schneefernerhaus (Zugspitze) on 17 April 2010. The analyses are based on the use of SEVIRI and CALIOP retrieval data to optimize the volcanic ash dispersion between 15 and 18 April.

analysis increment of EM-1 on 16 April at 13:00 UTC (cf. Figures A.9, A.10, A.11, A.12, A.13, A.14, A.15, and A.16 of Appendix A for ensemble members EM-2 to EM-9), comparably to Figure 7.7. For both experiments, the background distribution of volcanic ash remains unchanged. Thus, the analysis of 15 April, which is used for the initial states of the background simulations on 16 April, is independent of the

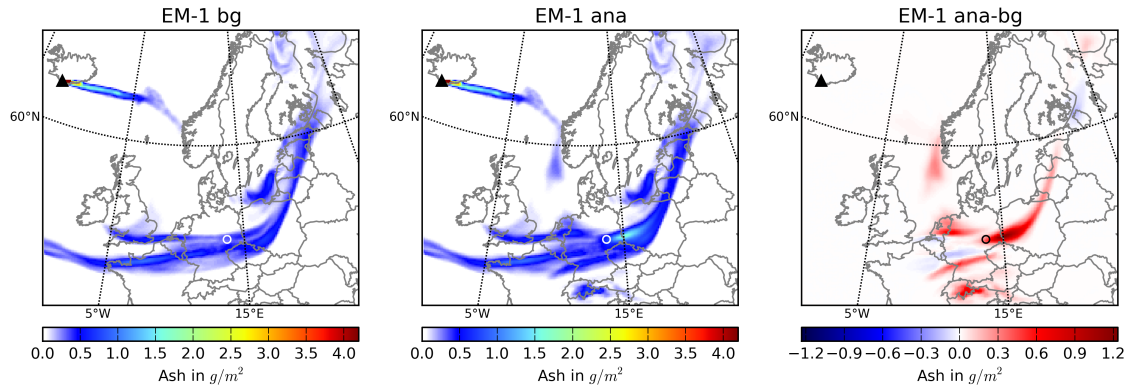


**Figure 7.15:** Horizontal volcanic ash distribution above Europe on 16 April at 13 UTC: EM-1 background field (left), EM-1 analysis field applying 4D-var assimilation of SEVIRI and CALIOP data (center), and the analysis increment given by the difference between analysis and background field (right). The small circles indicate the location of EARLINET lidar in Leipzig.

additional assimilation of the CALIOP retrievals on 15 April. The analysis and the analysis increments present significant corrections of the volcanic ash concentration above the German-Polish boarder region. In relation to Figure 7.7, which reveals a maximum increment of volcanic ash of about  $1.7 \text{ g m}^{-2}$ , here it only accounts for approximately  $1.2 \text{ g m}^{-2}$ . Furthermore, tenuous volcanic ash clouds additionally arise in the analysis, north and south of the main ash cloud.

For the same time, the vertical ash distribution of the two 4D-var ensemble experiments are pictured in Figure 7.16, in addition to an independent lidar equivalent profile at the EARLINET station of Leipzig. The comparison of both analyses allows for the identification of the impact of the assimilated CALIOP data on the volcanic ash distribution. In altitudes of 10–13 km, a low concentrated ash layer is simulated by four ensemble members. Between 3.5 km and 5.8 km, EM-3 and EM-4 both show a single ash layer, with maximum concentration below  $200 \mu\text{g m}^{-3}$ . The peak of the volcanic ash layers represented by EM-5 and EM-6 are also slightly shifted to 4 km heights. The remaining ensemble members only include insignificant changes. The discrepancies among the ensemble members appear to be slightly increased in contrast to the first experiment. The third graphic of Figure 7.16 illustrates the lidar mass equivalent, calculated from the 532 nm backscatter coefficients, using the same lidar ratio and mass conversion factor as described in the previous section. This mass equivalent depicts a maximum ash concentration of approximately  $780 \mu\text{g m}^{-3}$  at 3.2 km altitude. None of the ensemble members of both experiments captures this quantity in the analysis. A possible reason is the coarseness of vertical model grid discretization that prevents the formation of very thin ash layers such as it is captured by the high resolution lidar measurements. On the basis of these results, it is not possible to evaluate the influence of the supplementary observational data source on the analysis skill or the observability.

Figure 7.17 illustrates the mean volcanic ash mass column values of both 4D-var

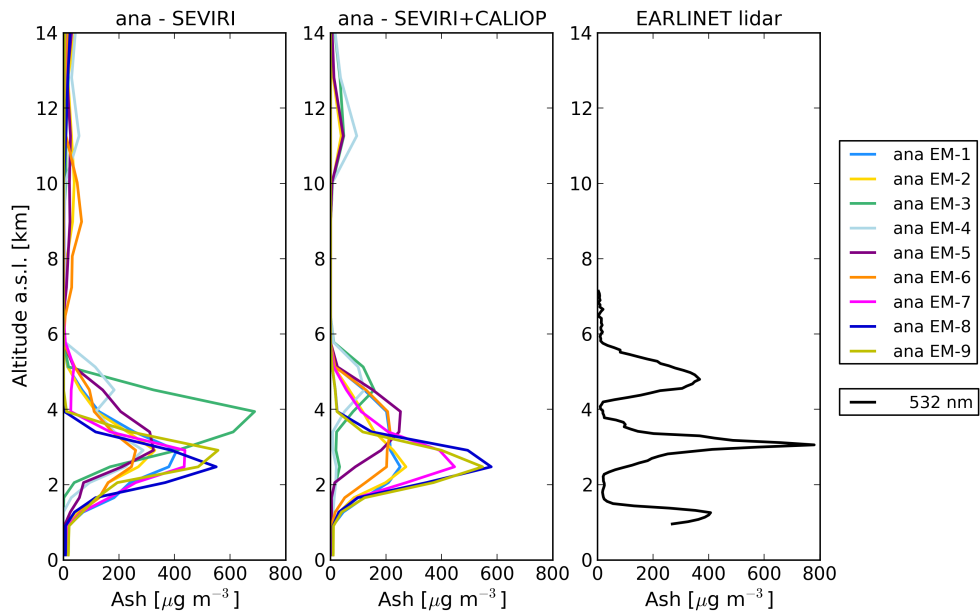


**Figure 7.16:** Vertical volcanic ash distribution over Leipzig on 16 April at 13 UTC: Concentration profiles of the analysis shown in Figure 7.8 (left) and of the analysis (center) applying combined SEVIRI and CALIOP retrievals, as well as the mass equivalent derived from the lidar backscatter coefficient profile at 532 nm of the Leipzig EARLINET station (right).

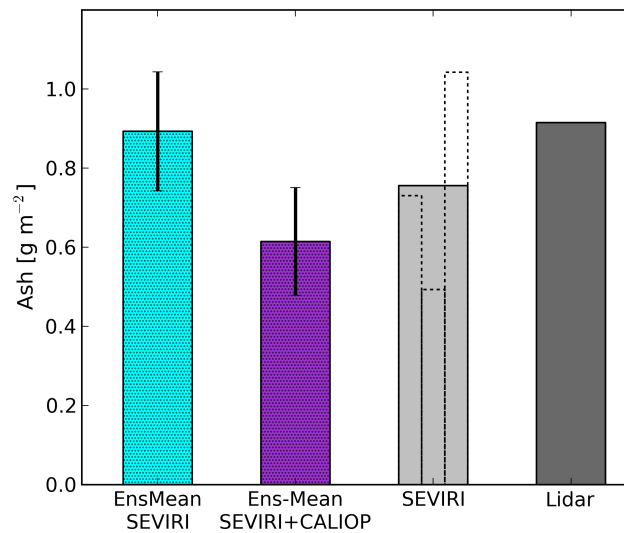


**Figure 7.17:** Volcanic ash column mass loadings at the EARLINET station in Leipzig on 16 April at 13 UTC: analysis ensemble mean applying only SEVIRI retrievals for the assimilation (Ens Mean SEVIRI, cyan dotted), analysis ensemble mean applying SEVIRI and CALIOP retrievals for the assimilation (Ens Mean SEVIRI+CALIOP, violet dotted), both including the standard deviation (error bars), SEVIRI observation mean (light gray) and lidar derived mass loading equivalent (dark gray).

ensemble experiments in comparison the observationally derived values from SEVIRI and the EARLINET lidar in Leipzig on 16 April at 13:00 UTC (cf. Figure 7.9). The ensemble mean of the analysis, which combines the information obtained by SEVIRI and CALIOP, features the lowest concentration of  $0.61 \text{ g m}^{-2}$ . In contrast to the analysis ensemble mean when ingesting SEVIRI retrievals only, the standard deviation of the second experiment does hardly reach the SEVIRI mean value and, at the same time, underestimates the lidar derived ash column mass loading markedly. However, the ensemble spread of both ensemble mean values is approximately equal. The graphic indicates that at least for the location of Leipzig, the assimilated CALIOP retrieved aerosol extinction coefficients induce a significant reduction of the vertically integrated ash concentration. This appears to be rather unfavorable, when comparing to the observations.

A detailed discussion of the cost function reductions for the investigated experiment is omitted here, since it is fairly speculative to draw conclusions in terms of the analysis skill and observability. However, it should be mentioned that the relative cost reduction turns out to perform less efficient compared to the first experiment (also cf. Figure A.17 of Appendix A). This might be caused either by an inadequate number of observations, or by a poor tangent linear approximation within the model. To reveal the influence of CALIOP data assimilation on the uncertainty of the ash cloud position, Figure 7.18 shows the same graphics as displayed in Figure 7.11, but for the 4D-var ensemble analysis applying SEVIRI and CALIOP retrievals. On 15 April at 12:00 UTC, all ensemble members feature elevated volcanic ash column mass loadings over the Atlantic, at about  $61^\circ\text{N}$  and  $4^\circ\text{W}$ . There, the elliptically shaped isopleths agree fairly well on their local position, while their lengthwise extension over the North Atlantic varies moderately. Here, the locally enhanced volcanic ash concentration at the Norwegian coast is also represented by all ensemble members. However, only EM-3 depicts volcanic ash concentrations above Brittany and the Irish Sea, which are introduced by the CALIOP retrievals obtained from the satellite overpass on 15 April at 13:30 UTC. The spaghetti plot of the analysis on 16 April at 12:00 UTC shows a reduced spatial extent of the concentrated mass isopleths over Central Europe, just capturing the area from Eastern Germany to Central Poland. South of this region, the area surrounded by the mass isopleths of EM-3 and EM-4 is slightly enlarged, as well as over the Gulf of Finland. In contrast to the analysis of the first experiment, the spaghetti plot of 17 April at 04:00 UTC depicts less changes of the isopleths in comparison with the first guess. The area characterized by concentrations higher than  $1.0 \text{ g m}^{-2}$  in the analysis of EM-3 and EM-4 over France and Switzerland is less reduced, while the locally increased ash concentrations above the Western Ukraine diminish.

On the basis of these spaghetti plots, the following conclusions can be drawn: Regions, where the spaghetti plots of all nine ensemble members densely coincide, are characterized by good observability. Strengthened observability due to CALIOP observations is solely given over the North Atlantic and the Norwegian West coast on 15 April. The confined localization of enhanced ash concentrations above the German-Polish border region on 16 April is either induced by increased observability, or by inconsistent ash retrievals of SEVIRI and CALIOP. The latter also explains that the high

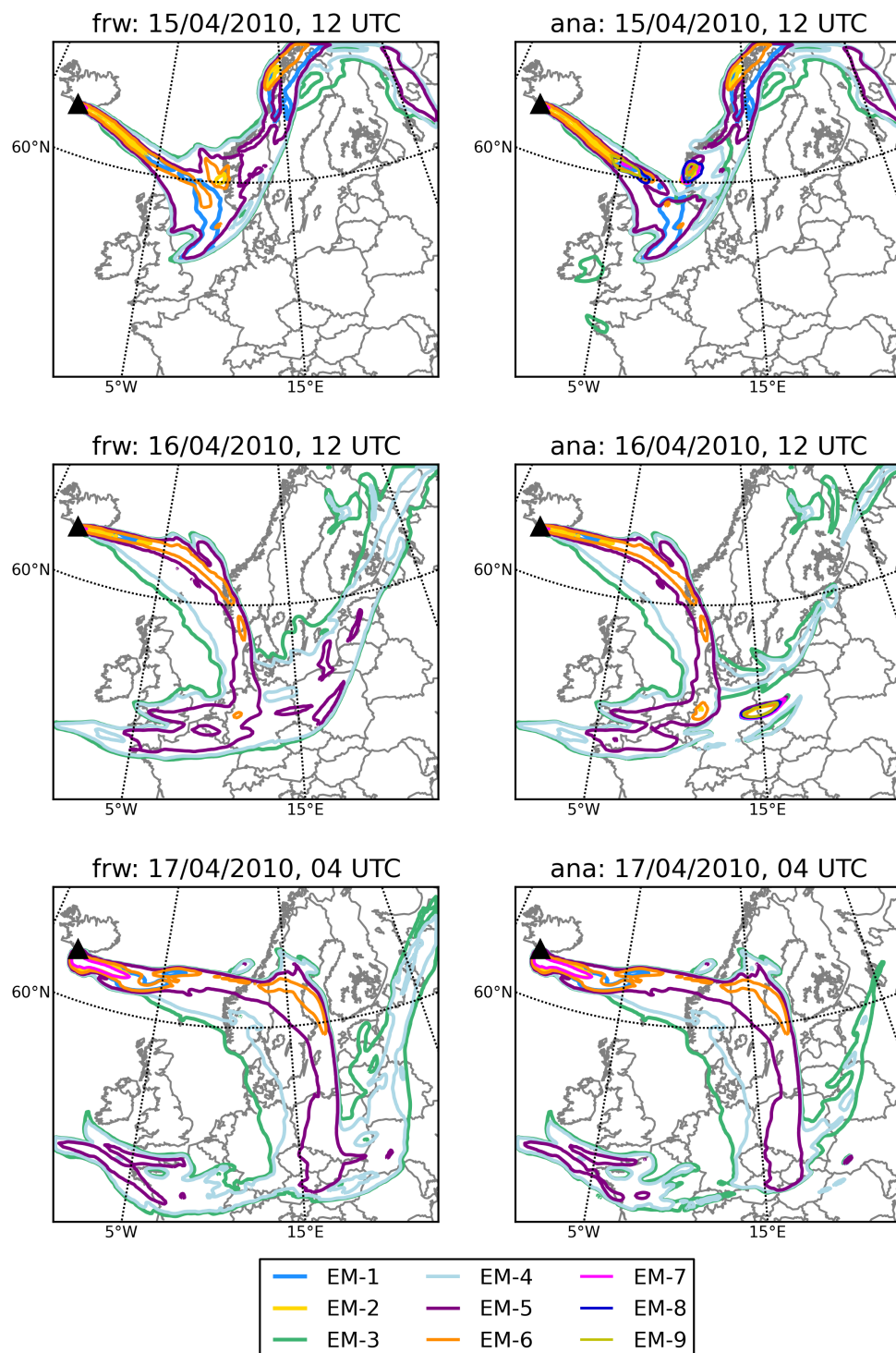


**Figure 7.18:** Spaghetti plots of  $1.0 \text{ g m}^{-2}$  mass isopleths for all nine 4D-var ensemble members: first guess (left column) and analysis (right column) are depicted on 15 April at 12 UTC, 16 April at 12 UTC, and 17 April at 04 UTC. The ensemble analysis is based on the assimilation of SEVIRI and CALIOP data.

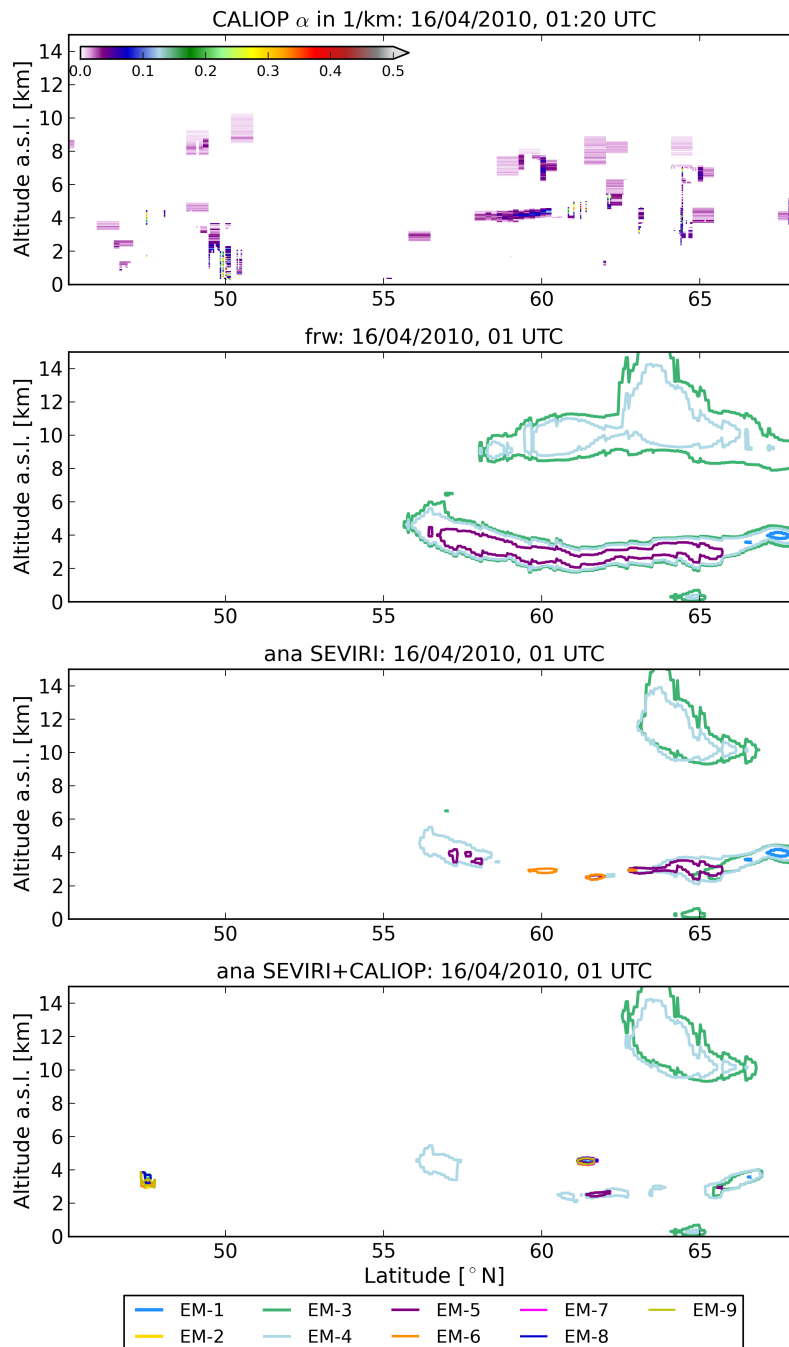


**Figure 7.19:** Comparison of assimilated CALIOP particle extinction retrievals (cf. *Winker et al.* [2012], top panel) with spaghetti plots of  $0.2 \text{ mg m}^{-3}$  volcanic ash concentration isopleths as vertical cross section along the 16 April 01:20 UTC CALIPSO overpass (cf. Figure 7.13). The mass isopleths of all nine 4D-var ensemble members are depicted for the first guess (second panel from top), the analysis using SEVIRI observations only (third panel from top), and the analysis using SEVIRI and CALIOP data (bottom panel) on 16 April at 01 UTC.

concentrations, emitted from EM-3 and EM-4 eruption patterns, are less reduced in the ensemble analysis.

Since the additional information source of CALIOP particle extinction coefficients in the 4D-var assimilation does not introduce significant impacts on the Europe-wide observability of the volcanic ash event, the local influence is now investigated. Figure 7.19 displays the volcanic ash extinction coefficient retrievals of CALIOP measurements taken on 16 April at 01:20 UTC in the top graphic. A moderate number of spatially narrow volcanic ash induced patterns is visible along this satellite path, which is illustrated in Figure 7.13 (yellow line). The retrievals at latitudes south of 55°N are rather not caused by volcanic ash, but assimilated. According to *Winker et al.* [2012], a well defined ash layer is visible between 4 km and 5 km in altitude and at latitudes of 58–62°N, where extinction coefficients increase towards higher latitudes. Since the model output is only available at full clock hours, the ensemble results are presented at 01:00 UTC. The vertical cross section of 0.2 mg m<sup>-3</sup> isopleths along the satellite path are illustrated for the ensemble first guess, and the ensemble analyses of the first and second experiment, respectively. Comparing the spaghetti plots, it can be seen that the extent of the high ash cloud represented in the EM-3 and EM-4 first guess runs in height levels between 8 km and 14 km in altitude and 58–69°N in latitude is strongly reduced in both analyses. Also the underlying ash layer at 2–6 km altitude featured by EM-3, EM-4, and EM-5 is significantly corrected to very small ash cloud patches. However, these patches are not in good agreement among the ensemble members. Solely the analysis applying SEVIRI and CALIOP retrievals exhibits dense spaghetti plots of all nine ensemble members at 62°N and at 5 km altitude. At about 47°N, another punctual ash cloud is reflected by all ensemble members of the second experiment. This is induced by the locally restricted but intense extinction coefficient profiles of the CALIOP observations at about 4 km altitude.

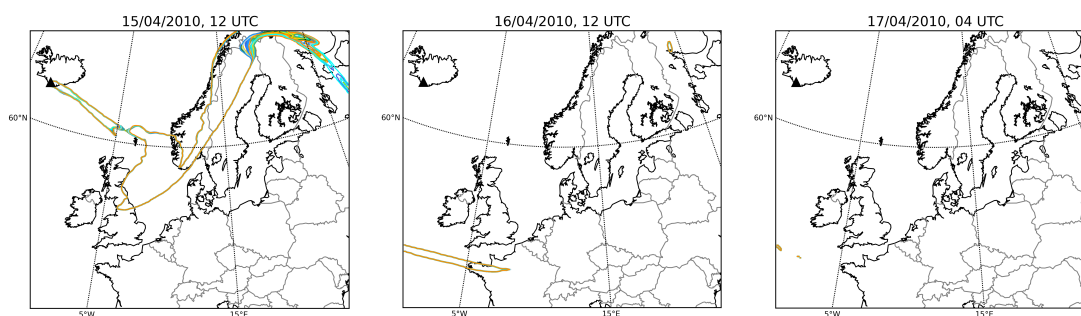
To summarize the results of this section, it is concluded that the additionally assimilated CALIOP volcanic ash extinction coefficient retrievals do not impact the ensemble analysis significantly. Only within very restricted areas, the CALIOP observations induce enhanced observability of the volcanic ash dispersion above Europe. This is certainly caused by the dense cloud cover above Europe, which impeded the retrieval of volcanic ash significantly. Moreover, it seems that CALIOP and SEVIRI retrievals are sometimes inconsistent in terms of the location and quantity of volcanic ash. The CALIOP retrieval includes much more assumptions and consequently larger uncertainties in contrast to the SEVIRI retrieval. Hence, the uncertainties of the CALIOP data prevent the constraining effects on the ensemble analysis of both the horizontal as well as the vertical distribution of volcanic ash.

## 7.4 ESIAS-chem ensemble using SEVIRI retrievals

In this third experiment, the volcanic ash dispersion following the eruption of the Eyjafjallajökull volcano and its observability is analyzed by means of the PS

ensemble analyses by ESIAS-chem. The focus is placed on the application of SEVIRI column mass loading retrievals for emission factor optimization using the particle smoother algorithm. The skill of the analysis and the evaluation of the observability is investigated, examining the analysis of the horizontal ash distribution.

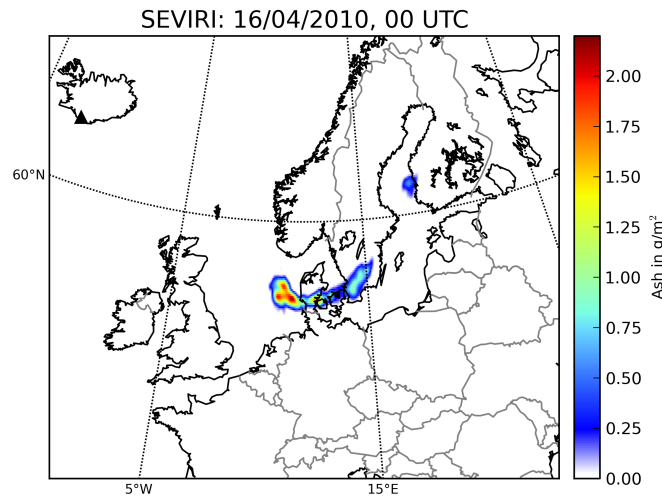
Figure 7.20 depicts the resulting spaghetti plots of the full 60 members PS ensemble on 15 April at 12:00 UTC, 16 April at 12:00 UTC, 17 April at 04:00 UTC, respectively. Here, the complete SEVIRI observational data set is applied, allowing for the comparability with the 4D-var ensemble experiments. All graphics illustrate that the isopleths of the 60 ensemble members mostly concur. Only above Northern Scandinavia and North-West Russia, the mass isopleths differ significantly on 15 April at 12:00 UTC. In the analyses of 16 and 17 April, there are no ash concentrations visible above the European continent, which exceed the threshold of  $1.0 \text{ g m}^{-2}$ . Fairly small areas of enhanced ash concentrations are only depicted west of Brittany and in North-West Russia, respectively. Consequently, it can be concluded, that the PS ensemble analysis is characterized by a weak skill regarding the long range transport from Iceland to Europe. It is not reasonable to further investigate the ESIAS results in terms of observability, later than two days after the initial eruption of the Eyjafjallajökull. Therefore, the comparability with the 4D-var ensemble is not presented in terms of the temporal evolution of the ash dispersion.



**Figure 7.20:** Spaghetti plots of  $1.0 \text{ g m}^{-2}$  volcanic ash column mass loadings for the PS ensemble analysis with 60 ensemble members on 15 April at 12 UTC, 16 April at 12 UTC, and 17 April at 04 UTC. The PS ensemble analysis is based on the assimilation of all available SEVIRI data.

Instead, the focus is placed on the investigation of the volcanic ash distribution on 16 April at 00:00 UTC. Figure 7.21 shows the SEVIRI volcanic ash column mass loading retrievals at this time. A dense ash cloud extends from the North Sea west of Denmark to Southern Sweden. The maximum ash column mass loading of  $2.17 \text{ g m}^{-2}$  is retrieved over the North Sea close to the Western Danish coast. Another small and tenuous volcanic ash cloud is located off-shore to South-West Finland.

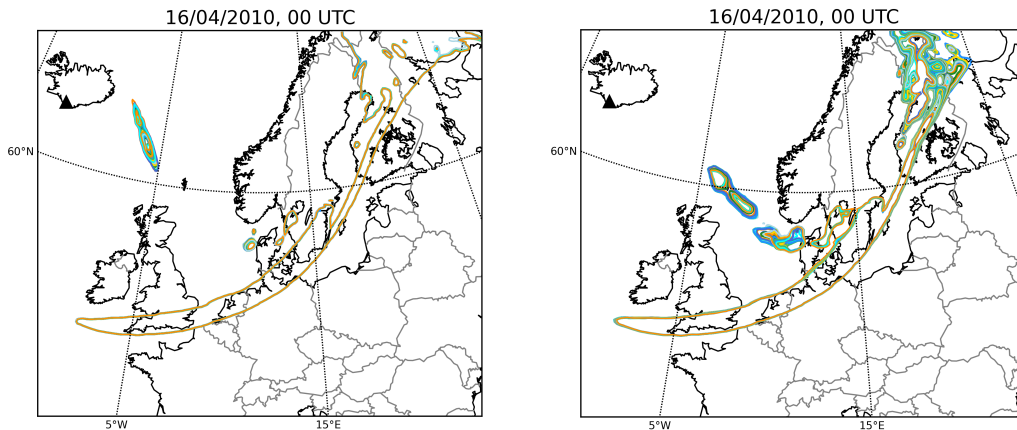
To increase the impact of observational information in terms of enhanced volcanic ash concentration values, a second particle smoother experiment is performed. Here, the SEVIRI data set is confined to all retrieval values higher than  $0.45 \text{ g m}^{-2}$  (see



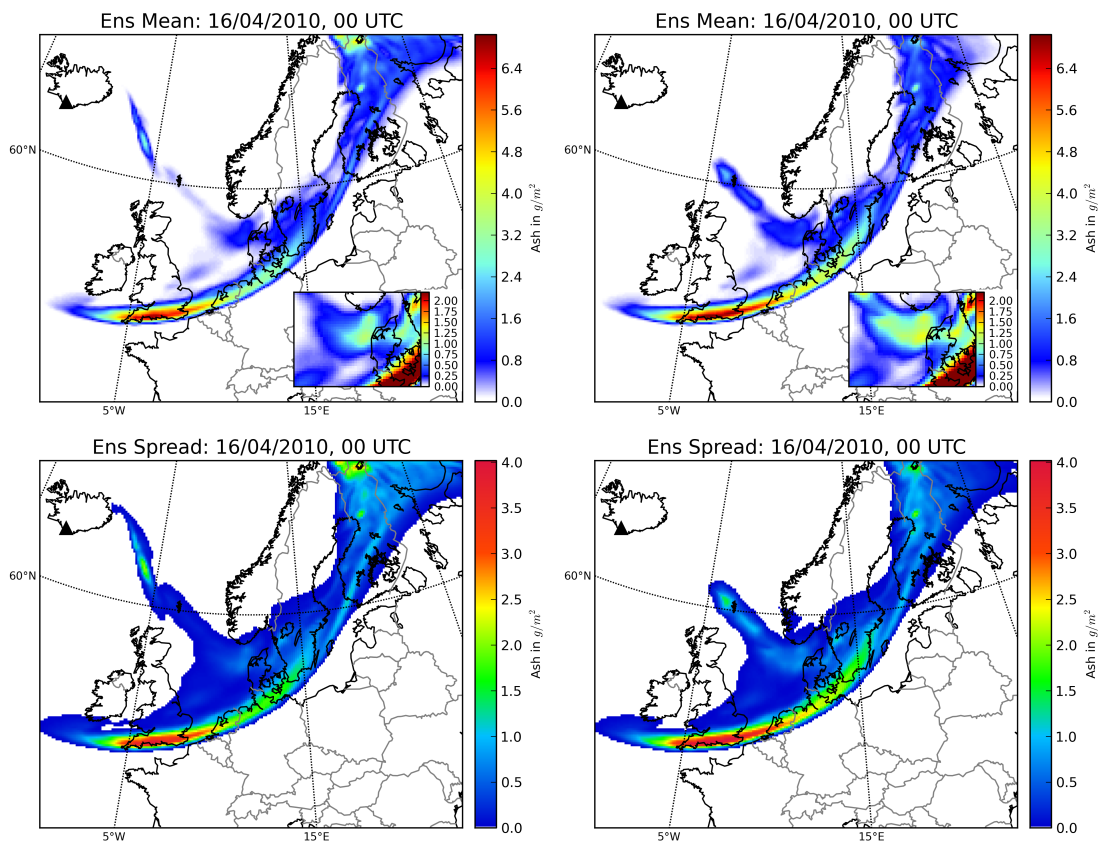
**Figure 7.21:** MSG-SEVIRI volcanic ash column mass loading retrievals on 16 April at 00 UTC (cf. *Prata and Prata* [2012]).

Figure A.19). In the following discussions, the PS ensemble analysis using all available SEVIRI data is referred to as SEVIRI-1 analysis, while the PS ensemble analysis using the reduced number of SEVIRI retrievals is called SEVIRI-2 analysis. Figure 7.22 presents the spaghetti plots of  $1.0 \text{ g m}^{-2}$  volcanic ash column mass loadings for both ESIAS-chem PS ensemble analyses on 16 April at 00:00 UTC. Comparing the two graphics, the impact of using a reduced number of observations becomes visible. The SEVIRI-1 analysis features a wide stretching ash cloud from south of Ireland to North-East Scandinavia. Here, the isopleths conform precisely. North of Scotland and at the western coast of Denmark, there are two ash clouds exceeding the threshold value of  $1.0 \text{ g m}^{-2}$ . Both indicate a compliance of all ensemble members, though the isopleths are not exactly at the same position. The major ash cloud is also depicted in the SEVIRI-2 analysis, whereas the spaghetti plots include a smaller area above North-West Russia. Here, the isopleths show less compliance, albeit they are not significantly diverging. The SEVIRI-2 analysis reveals an ash cloud between Scotland and Norway and another west of Denmark. The latter appears to be much larger in contrast to its shape in the SEVIRI-1 analysis. The spaghetti plots are fairly dense, but not perfectly overlapping. For both analyses, the ash cloud above the Kattegat and South-West Sweden as well as the ash patch at the Finish coast seem to be slightly displaced in contrast to the SEVIRI retrievals.

By means of these spaghetti plots, it is rather problematic to identify concentration patterns, which are controlled by the assimilated observations. Additional information on the constraining impacts can be gained by examining the ensemble mean and the ensemble spread. Both are illustrated in Figure 7.23 at the same analysis time for the SEVIRI-1 and the SEVIRI-2 analyses. The ensemble mean analyses generally reproduce the volcanic ash distribution as they were depicted in the spaghetti plots, whereas the areas of low ash concentrations appear close to the contours and over



**Figure 7.22:** Spaghetti plots of  $1.0 \text{ g m}^{-2}$  volcanic ash column mass loadings of with 60 ensemble members on 16 April at 00 UTC: the PS ensemble analysis based on the assimilation of all available SEVIRI data (SEVIRI-1 analysis, left panel) and the PS ensemble analysis based on the assimilation of SEVIRI retrievals higher than  $0.45 \text{ g m}^{-2}$  (SEVIRI-2 analysis, right panel).



**Figure 7.23:** Ensemble mean (top panels) and ensemble spread (bottom panels) for the PS ensemble analyses SEVIRI-1 (left panels) and SEVIRI-2 (right panels) on 16 April at 00 UTC. The inserted maps (in the upper panels) enlarges the ensemble mean in the area of highest SEVIRI retrieval values.

the North Sea. The highest volcanic ash column mass loadings are located over the south coast of England in both ensemble mean analyses. The comparison of the ensemble means with the ensemble spreads reveals that the areas of highest mean ash column mass loadings represent the areas of increased ensemble spreads. Since it is assumed that observations constrain the model states, the ensemble spread is typically reduced, when observations of the considered air masses are available for the assimilation. This implies that the part of volcanic ash cloud extending from south of Ireland to Southern Sweden is not observable. The same can be concluded for the higher concentrated volcanic ash in Northern Scandinavia.

To evaluate the predictive skill of the ensemble, the ensemble mean analyses are compared with the SEVIRI observations at this time. Therefore, the inlay maps in Figure 7.23 illustrate the ensemble mean column mass loadings of the PS analyses in the region of highest SEVIRI retrieval column mass loadings. Here, the color bar is chosen to include the same dimensions as displayed in Figure 7.21. It appears that SEVIRI-2 analysis represents the observations better than the SEVIRI-1 analysis. The SEVIRI-2 analysis provides maximum volcanic ash column mass loadings of  $1.4 \text{ g m}^{-2}$ , while the SEVIRI-1 analysis obtains maximum values of  $1.1 \text{ g m}^{-2}$ . As maximum volcanic ash loads are especially important for aviation control and guidance, the SEVIRI-2 analysis is now investigated in more depth.

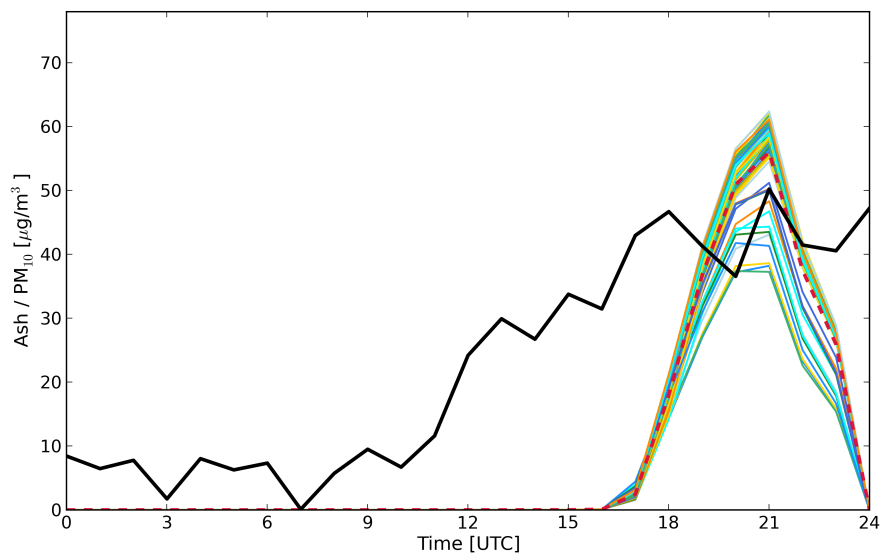


**Figure 7.24:** Comparison of  $\text{PM}_{10}$  observations (black line) with the PS ensemble analysis SEVIRI-2 of volcanic ash concentrations (60 ensemble members in colored lines) at Schneefernerhaus (Zugspitze) on 17 April 2010. The ensemble mean of the SEVIRI-2 analysis is depicted as red dashed line.

Figure 7.24 shows the time series of volcanic ash concentrations of all 60 ensemble members at Schneefernerhaus in Southern Germany on 17 April 2010 (cf. Figure A.20 for the SEVIRI-1 analysis). In comparison, their ensemble mean is illustrated as well as the observed  $\text{PM}_{10}$  concentrations. All ensemble members depict a similar temporal

evolution of the volcanic ash concentration at Zugspitze: Here, the volcanic ash cloud arrives past 16:00 UTC. The maximum ash concentrations are reached after about five hours. During the following 4–5 hours all concentrations decrease to zero level. As seen in Figure 7.6 and Figure 7.14, the measured  $\text{PM}_{10}$  concentration increases more than 5 hours earlier compared to the ensemble analysis. Between 19:00 UTC and 22:00 UTC, the observed concentration is well included in the ensemble spread of the PS ensemble analysis. The ensemble mean shows higher ash concentrations. Here, it must be considered that the measured concentrations are not directly comparable with the ensemble analysis, since the plotted quantities differ. The ensemble results include concentrations of pure volcanic ash of all particle sizes, whereas the measurements contain concentrations of all aerosol species of particles smaller than  $10\ \mu\text{m}$  in diameter. However, both depict the ash arrival and evolution at Zugspitze with sufficient precision. As already discussed in previous sections, the assimilated SEVIRI retrievals do not provide satisfying observability of the volcanic ash arriving at Schneefernerhaus on 17 April. Thus, also the particle smoother analysis cannot adequately represent the volcanic ash dispersion.

In the PS ensemble analysis, emission factors are optimized to find the best estimate of the emission source parameters, volcanic ash emission height and strength, which strongly control the volcanic ash dispersion. Figure 7.25 illustrates the analyzed volcanic ash emission profiles of ensemble member 30 in the atmospheric column above the Eyjafjallajökull. Ensemble member 30 is randomly chosen and acts here as example of possible emission estimates. Compared to the other ensemble members,

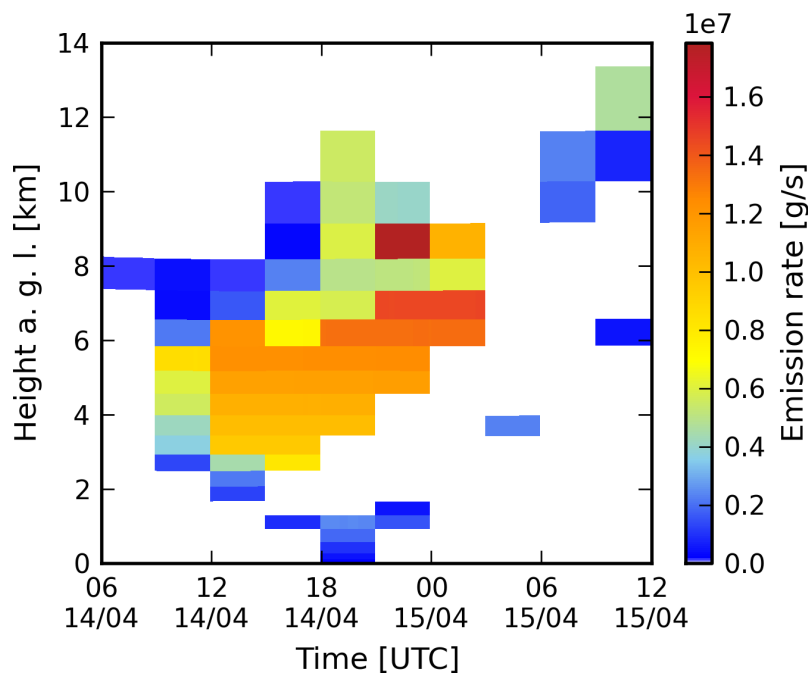


**Figure 7.25:** Analyzed volcanic ash emission profiles of PS ensemble member 30 between 14 April at 06 UTC to 15 April at 12 UTC.

member 30 shows slightly stronger emissions, whereas the emission pattern are similar for the full ensemble. The emission factor correction in the analysis is restricted to the period between 14 April at 06:00 UTC and 15 April at 12 UTC. The optimized emission packages are representative for one model layer and a time interval of three hours. The temporal evolution of volcanic ash emissions reveals that emissions are strongest between 09:00 UTC on 14 April and 03:00 UTC on 15 April at heights of 2.5–9.0 km above the volcano's summit. The emitted mass, containing the maximum emission rate of  $17.85 \text{ t s}^{-1}$  is analyzed at 21:00–00:00 UTC at 8.2–9.0 km altitude. Besides the strong and connected emission plume, several separated emission patches are visible. To some extent, this complies with the natural behavior of emission plumes. Compared to other studies such as performed for example by *Stohl et al.* [2011], the analyzed emission rates are estimated in the same order of magnitude. However, the observability of the volcanic ash dispersion above Europe does not sufficiently constrain the volcanic emissions of the Eyjafjallajökull eruption in 2010 accessing SEVIRI retrievals only. This conclusion does not only rest upon the analysis of the emission profiles (Figure 7.25), but predominantly on the analysis of the volcanic ash dispersion as described in this section before.



## 8 | Conclusion and Outlook

The observability of sudden aerosol injections in the Earth's atmosphere has been investigated, analyzing the aerosol scenario of the Eyjafjallajökull eruption in April 2010. The volcanic eruption is selected as a prototype aerosol event without validity of traditional assumptions of data assimilation like the tangent linear approximation. Decision making with respect to air traffic safety during a volcanic eruption is challenging. Aerosol dispersion predictions are generally based on numerical models. These predictions can be improved by applying data assimilation or inverse modeling, which allow for the supplemental inclusion of information obtained by observations. However, the resulting model analysis should be carefully evaluated with regard to uncertainties and in consideration of the applied knowledge. Here, the degree of observability of the volcanic ash dispersion scenario plays a major role. The combination of modeled and observed ash concentrations allows for the qualified identification of regions with critical threshold exceedance. During the Eyjafjallajökull eruption 2010, the air traffic regulatory responsibilities, and aircraft and engine manufacturers decided to define three flight zones (*Prata and Rose [2015]*): In any area where volcanic ash concentrations were higher than  $4.0 \text{ mg m}^{-3}$ , air traffic was prohibited (no fly zone). Aircraft were permitted to fly in volcanic ash concentrations between  $0.2 \text{ mg m}^{-3}$  and  $2.0 \text{ mg m}^{-3}$  (enhanced procedures zone), while aircraft engines were only permitted to be exposed to concentrations between  $2.0 \text{ mg m}^{-3}$  and  $4.0 \text{ mg m}^{-3}$  for a very limited time.

To identify, which volcanic ash concentration patterns of the prediction are controlled by modeled and observed knowledge, two ensemble-based data assimilation approaches have been implemented and their potential and limits have been validated: First, an EURAD-IM 4D-var ensemble including nine ensemble members was evaluated. The ensemble members were chosen to incorporate the extremes of the volcanic event in terms of minimum and maximum eruption plume heights and volcanic ash mass eruption rates, as well as different realizations in between. For each ensemble member, initial values were optimized independently within daily 24-hours assimilation windows. Secondly, a 60 member particle smoother ensemble analysis was performed with the ESIAS-chem system, which also integrates the EURAD-IM as kernel. Here, resampling is performed utilizing the ensemble members' individual weights that rely on the cost function. Thus, emission factor optimization is realized by scaling the ensembles variance to achieve the best estimate of emission profiles.

Both analysis techniques pursue different optimization strategies, such that a direct comparison of their skills is difficult. However, a novel concept to analyze the

observability of unexpected aerosol events has been realized. It is applicable to any ensemble-based spatio-temporal analysis. The density of mass concentration isopleths by spaghetti plots is interpreted in terms of ensemble mean and ensemble spread. The following conclusions can be drawn within the limits of the selected case study: The 4D-var ensemble analysis sustains the long-range transport of volcanic ash from Iceland beyond Central Europe. In contrast, the PS ensemble does not sufficiently resolve increased volcanic ash concentrations later than two days after the initial eruption. Regarding the observability of the aerosol dispersion above Europe, the 4D-var ensemble performs well to determine the impact of the observational information. The PS ensemble analysis demonstrates compliance of all ensemble members regarding the position of threshold exceedance at least for vertically integrated ash concentrations. The appraisal of the strong observation values appears to be better matching for the 4D-var ensemble, whereas the PS ensemble analysis can be improved by assimilating only increased observations.

In addition, volcanic ash retrieval data from two completely different remote sensing observation principles have been assimilated. The main focus was placed on SEVIRI volcanic ash column mass loadings. For this purpose, the theoretical approach of the Kolmogorov-Sinai entropy emphasizes that vertically integrated column mass loadings can provide valuable information on the vertical distribution of volcanic ash by exploiting the dynamics of the system such as wind shear. The 4D-var and PS analyses proved this and revealed that the vertical position of the volcanic ash cloud could be well constrained with the SEVIRI retrievals. The information gain due to additionally assimilated particle extinction coefficients from CALIOP was assessed with the 4D-var ensemble. The CALIOP retrievals did neither improve the volcanic ash dispersion prediction significantly nor demonstrated enhanced observability. This might be caused by the processed error estimations, where SEVIRI retrievals were assigned less uncertainties compared to CALIOP retrievals.

A major issue in aerosol dispersion modeling is the constraining effect of properly simulated meteorological transport. Inverse modeling or data assimilation are negatively affected, if the applied observations cannot be reproduced in the model due to a misleading transport. Hence, temporally successive observations of the same volcanic ash cloud can be mutually exclusive for the assimilation system. This might be a reason, why the long-range transport could not be maintained in the PS ensemble analysis. Likewise, this explains that the PS ensemble mean better represents the maximum concentrations applying only increased observation values.

A final judgment, whether the 4D-var ensemble or the PS ensemble performs better, is not feasible based on this single case study. It is most likely that the large fragmented cloud cover above Europe impaired both SEVIRI and CALIOP observational data sets and hence, affected the observability analyses. Other factors might also hamper a final conclusion and are further discussed in the outlook. Yet, both algorithms may perform well in a less cloudy environment and may show potential for skillful ensemble predictions and decision making in the context of hazardous sudden aerosol injections.

For future research on the observability of sudden aerosol injections with ensemble-

---

based data assimilation techniques the following amendment activities are suggested. The ensemble setup should include the uncertainties of the prevailing meteorological conditions. Therefore, the combination with ESIAS-met is desirable for both assimilation techniques. Similarly, the influence of the ensemble size on the observability analysis could be further investigated. For the 4D-var ensemble analysis, it should be considered to allow the interaction between the different ensemble members. This interaction could be realized in terms of resampling as it is done within the particle smoother method. Thus, ensemble members describing unrealistic or unlikely atmospheric conditions can be rejected to influence the analysis. These conditions likewise include the meteorology as well as the emission characteristics and their consequences. To that effect, the aerosol dispersion could be constrained more specifically. For the ESIAS-chem emission factor optimization, it is recommended to increase the temporal resolution of constant emission profiles. The temporal evolution of the emission plume at the volcano appears much more dynamical compared to three-hourly estimates. This is emphasized by the radar observations of the Eyjafjallajökull emission plume described by *Arason et al.* [2011].

The observational information provided by SEVIRI and CALIOP retrievals is limited in case of the Eyjafjallajökull eruption 2010. On the one hand, this is owed to the prevailing cloud cover above Europe during the eruption. On the other hand, the measurements and retrievals are restricted by optical limitations and several assumptions used in the retrieval algorithms. To gain more information from observations additional satellite missions could be consulted. For example, these could be observations obtained by infrared sounders such as IASI (e. g. *Newman et al.* [2012]), spectroradiometers such as MODIS (e. g. *Picchiani et al.* [2011]), or other lidar instruments such as CATS (e. g. *Hughes et al.* [2016]). For future aerosol scenarios, the information content gained from forthcoming Sentinel-4, Sentinel-5 and Sentinel-5P (already launched in Oct. 2017) as well as from the EarthCARE (Earth Clouds, Aerosols and Radiation Explorer) mission should be investigated. The assimilation of SO<sub>2</sub> observations might contribute useful information. According to *Thomas and Prata* [2011], SO<sub>2</sub> can serve as a proxy for volcanic ash. Hence, the assimilation of OMI (Ozone Monitoring Instrument) or GOME-2 (Global Ozone Monitoring Experiment-2) data might be beneficial also regarding the prediction of gaseous emissions and sulfate. Observations provided by ground-based networks, such as EARLINET or obtained during research aircraft flights, allow for a different perspective and insight to the transported aerosol. Another improvement towards better observability might be realized by adapting the observation operators from retrieval assimilation towards radiance data assimilation. However, this requires special algorithmic features. The radiative transport of aerosol signatures or lidar signals must be described sufficiently well. Especially scattering effects are challenging to resolve. Mie scattering algorithms often ignore the complex shape of the particulates as well as multiple scattering. This can be respected to a certain extent by the T-matrix method (*Mishchenko et al.* [1996]) or by a data base approach, resting upon combinatory radiative transport methods as performed by *Meng et al.* [2010]. Finally, the current and new developments should be applied to different unexpected aerosol scenarios. Considering former volcanic eruptions, the Grímsvötn eruption in

2011 and the Holuhraun fissure eruption during 2014–2015 characterize scenarios with appropriate potential to be studied with an European chemistry transport model such as EURAD-IM. The developed system can also be tested on a near real time basis during future eruptions. Here, the needed observational data availability might be the most critical component of the prediction and analysis skill. Also for other aerosol emission events, the particle dispersion analysis and observability study can provide valuable information for decision making. Moreover, the investigation of numerical simulations of tropospheric transport of mineral dust (e. g. *Klose and Shao* [2013]), biomass burning aerosol (e. g. *Freitas et al.* [2007]; *Rio et al.* [2010]) or accidentally released substances (e. g. *Winiarek et al.* [2012]) with respect to observability might provide particular understanding of the emission parameters as well as the aerosols' properties, dynamics and chemical transformation processes.

# General Acknowledgments

The author gratefully acknowledges the computing time granted by the John von Neumann Institute for Computing (NIC) and provided on the supercomputer JU-RECA at Jülich Supercomputing Centre (JSC).

The author also gratefully acknowledges the Gauss Centre for Supercomputing e.V. ([www.gauss-centre.eu](http://www.gauss-centre.eu)) for funding this project by providing computing time on the GCS Supercomputer JUQUEEN at Jülich Supercomputing Centre (JSC).

For the provision of the SEVIRI ash retrieval data, the author sincerely thanks Dr. Fred Prata formerly from Nicarnica Aviation AS.

The CALIPSO data sets were obtained via the web page of the NASA Atmospheric Science Data Center (<https://eosweb.larc.nasa.gov>). Many thanks are granted to all involved people of the CALIPSO Science Team.

The PM<sub>10</sub> observations obtained at Schneefernerhaus, Zugspitze are courteously provided by the Hohenpeißenberg Meteorological Observatory, German Weather Service.

The author acknowledges EARLINET for providing aerosol lidar profiles available from the EARLINET webpage. The financial support for EARLINET in the ACTRIS Research Infrastructure Project by the European Union's Horizon 2020 research and innovation programme under grant agreement No. 654169 and previously under the grants No. 262254 in the 7th Framework Programme (FP7/2007-2013) and No. 025991 in the 6th Framework Programme (FP6/2002-2006) is gratefully acknowledged.



# A | Appendix

This appendix is designed to give further insight into the experiments studied in Chapter 7. Therefore, the Section A.1 includes graphics related to the 4D-var ensemble analysis, applying SEVIRI retrievals only. Section A.2 provides additional plots to the 4D-var ensemble analysis using SEVIRI and CALIOP retrievals. Finally, Section A.3 presents contributing results to the ESIAS-chem PS analysis assimilating SEVIRI data in the context of emission factor optimization. All figures are related to the aerosol scenario of the Eyjafjallajökull eruption in 2010.

## A.1 Supplements to the 4D-var ensemble analysis using SEVIRI retrievals

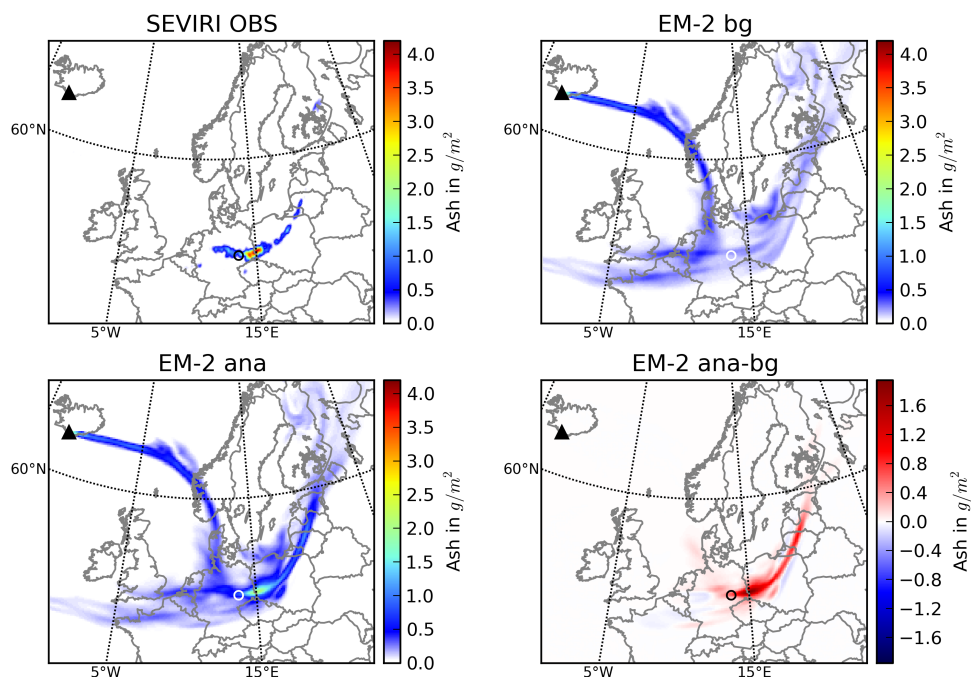


**Figure A.1:** Horizontal ash distribution above Europe on 16 April at 13 UTC as displayed in Figure 7.7 but for EM-2. The 4D-var analysis applies SEVIRI retrieval data.

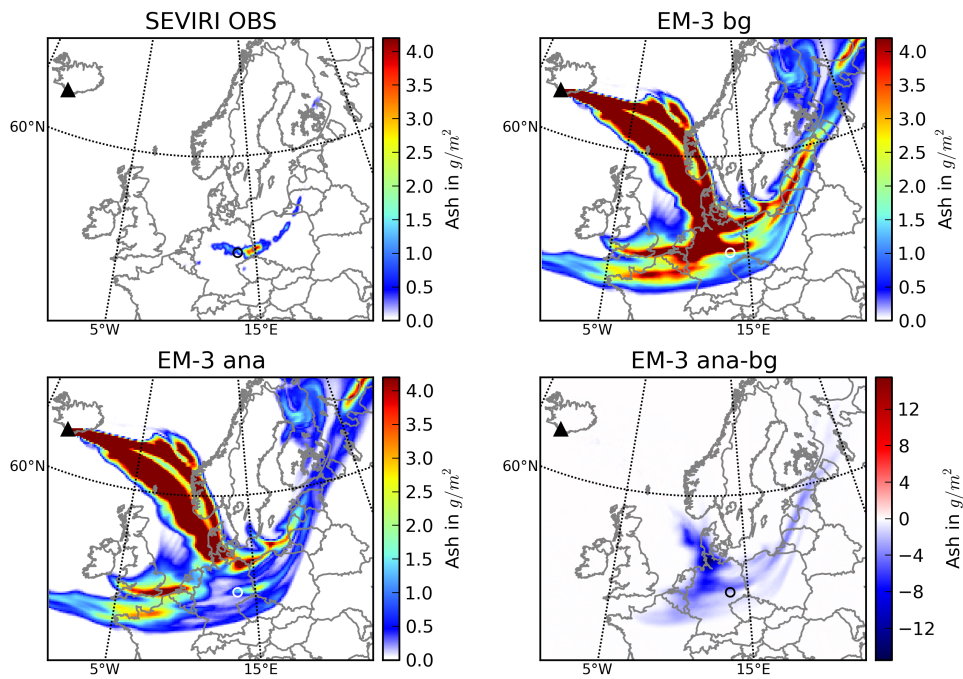


**Figure A.2:** Horizontal ash distribution above Europe on 16 April at 13 UTC as displayed in Figure 7.7 but for EM-3. The 4D-var analysis applies SEVIRI retrieval data.

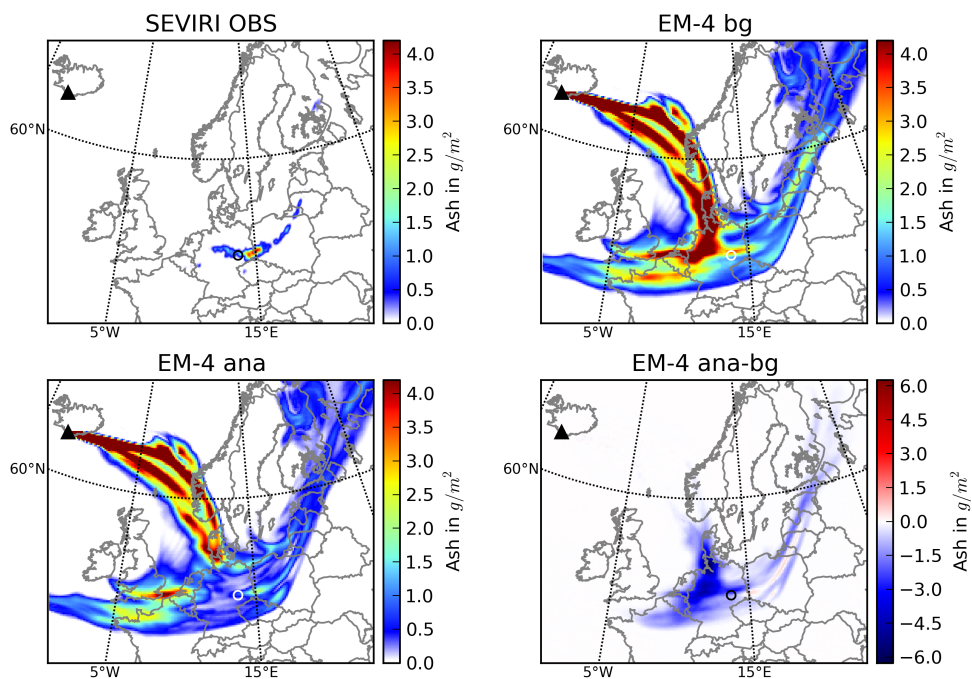


**Figure A.3:** Horizontal ash distribution above Europe on 16 April at 13 UTC as displayed in Figure 7.7 but for EM-4. The 4D-var analysis applies SEVIRI retrieval data.

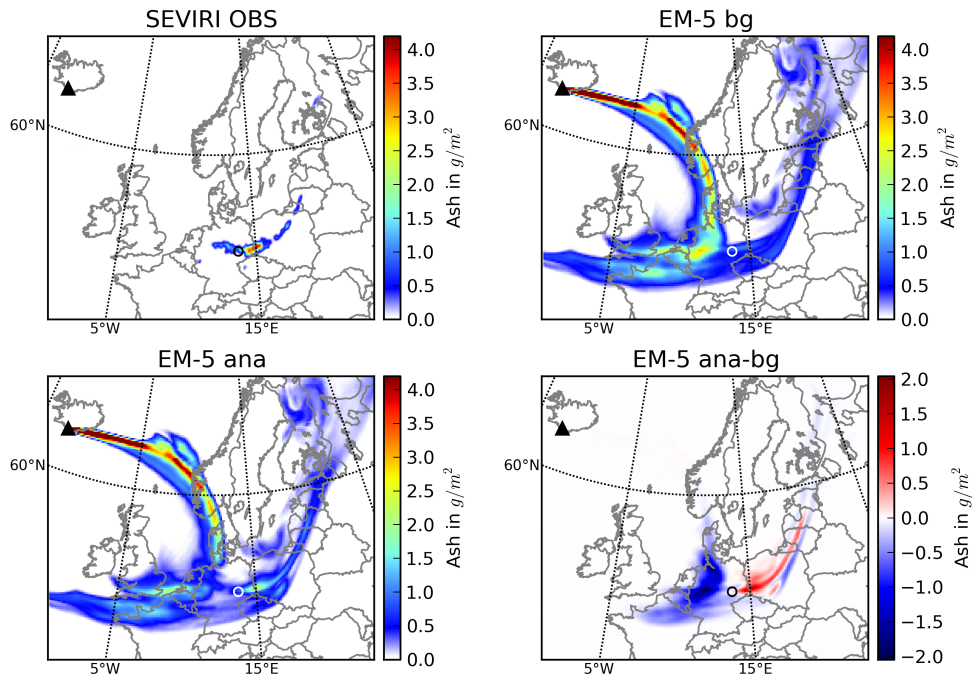


**Figure A.4:** Horizontal ash distribution above Europe on 16 April at 13 UTC as displayed in Figure 7.7 but for EM-5. The 4D-var analysis applies SEVIRI retrieval data.

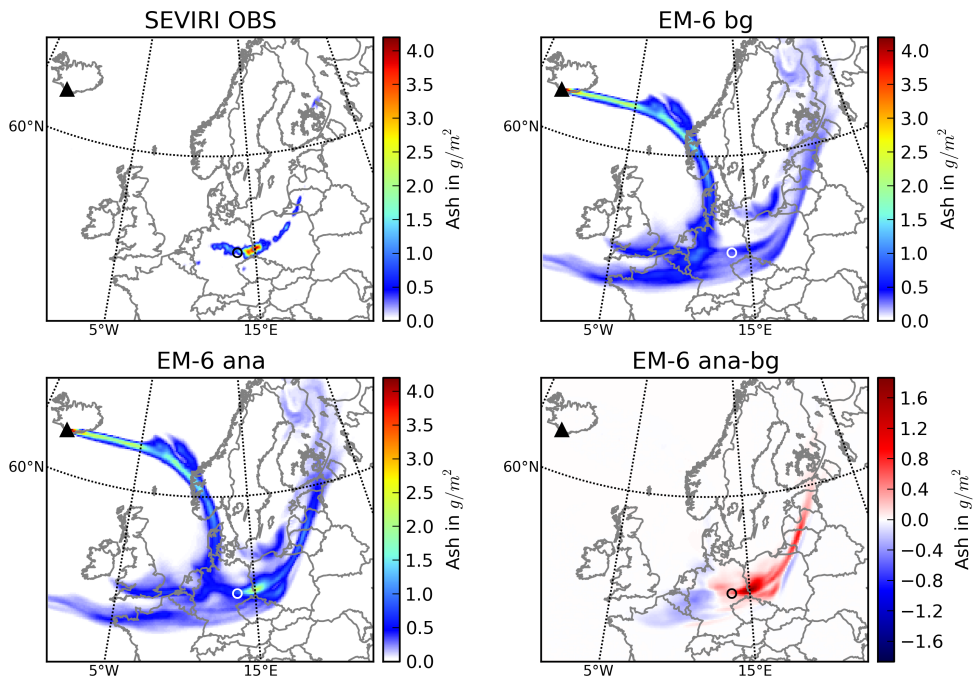


**Figure A.5:** Horizontal ash distribution above Europe on 16 April at 13 UTC as displayed in Figure 7.7 but for EM-6. The 4D-var analysis applies SEVIRI retrieval data.

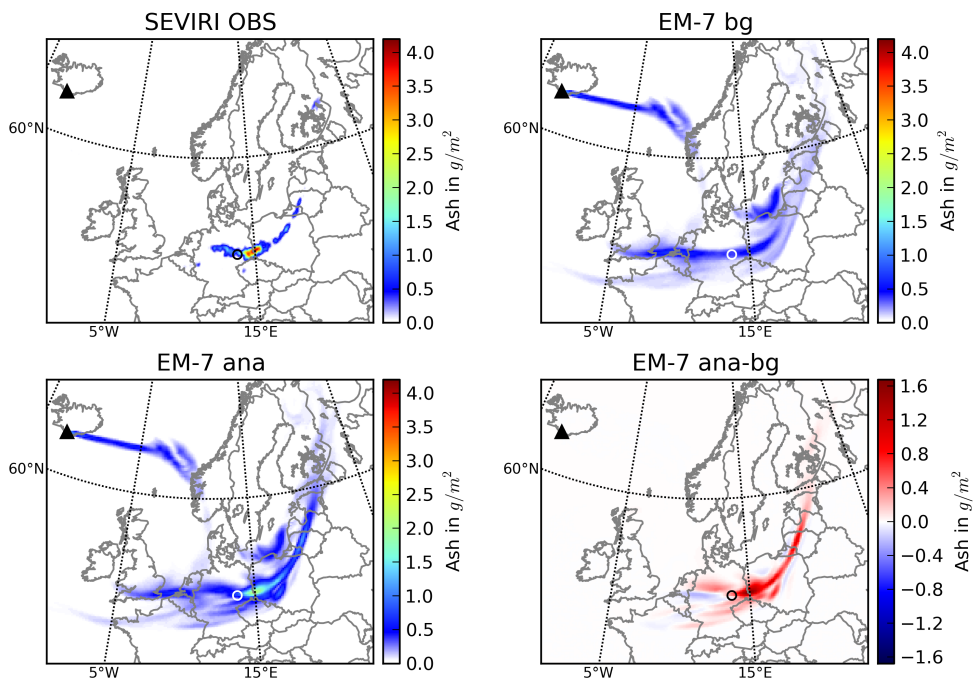


**Figure A.6:** Horizontal ash distribution above Europe on 16 April at 13 UTC as displayed in Figure 7.7 but for EM-7. The 4D-var analysis applies SEVIRI retrieval data.

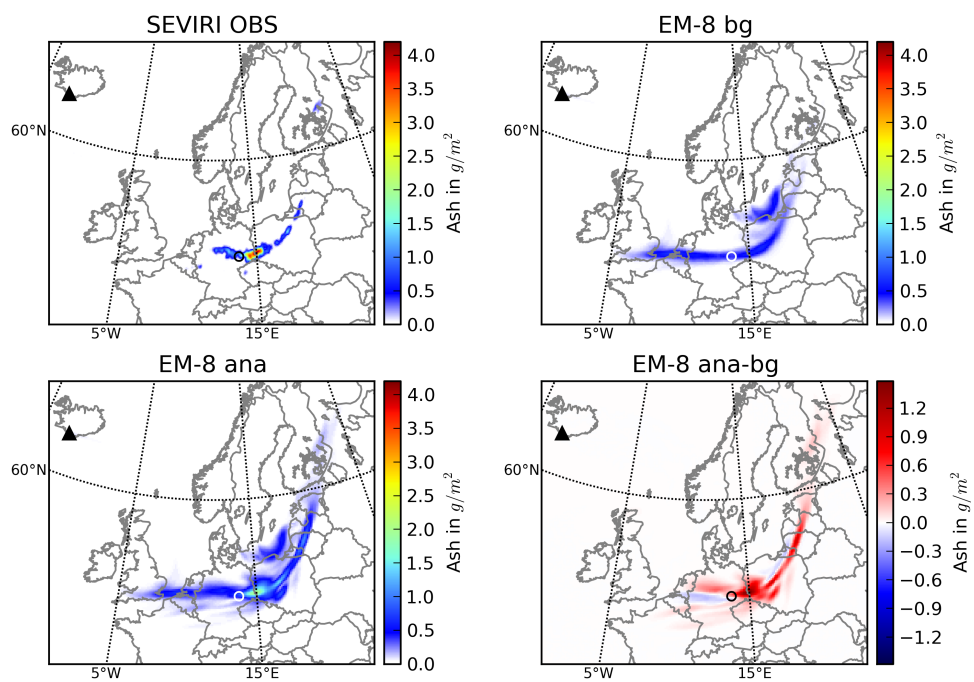


**Figure A.7:** Horizontal ash distribution above Europe on 16 April at 13 UTC as displayed in Figure 7.7 but for EM-8. The 4D-var analysis applies SEVIRI retrieval data.

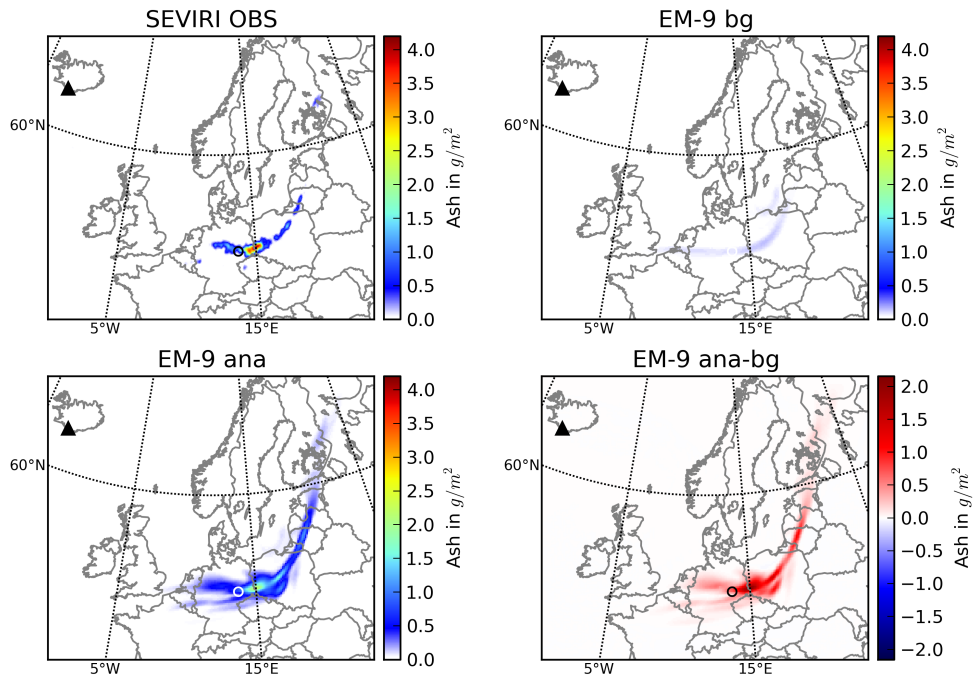


**Figure A.8:** Horizontal ash distribution above Europe on 16 April at 13 UTC as displayed in Figure 7.7 but for EM-9. The 4D-var analysis applies SEVIRI retrieval data.

## A.2 Supplements to the 4D-var ensemble analysis using SEVIRI and CALIOP retrievals

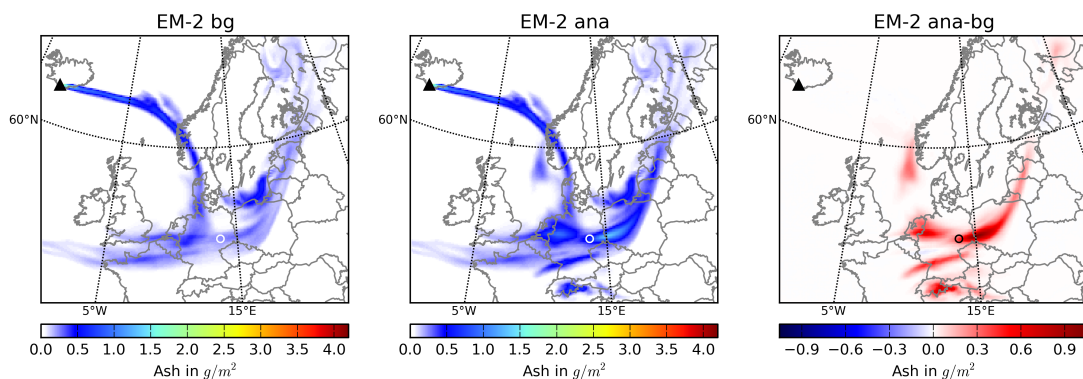


**Figure A.9:** Horizontal ash distribution above Europe on 16 April at 13 UTC as displayed in Figure 7.15 but for EM-2. The 4D-var analysis applies SEVIRI and CALIOP retrievals.

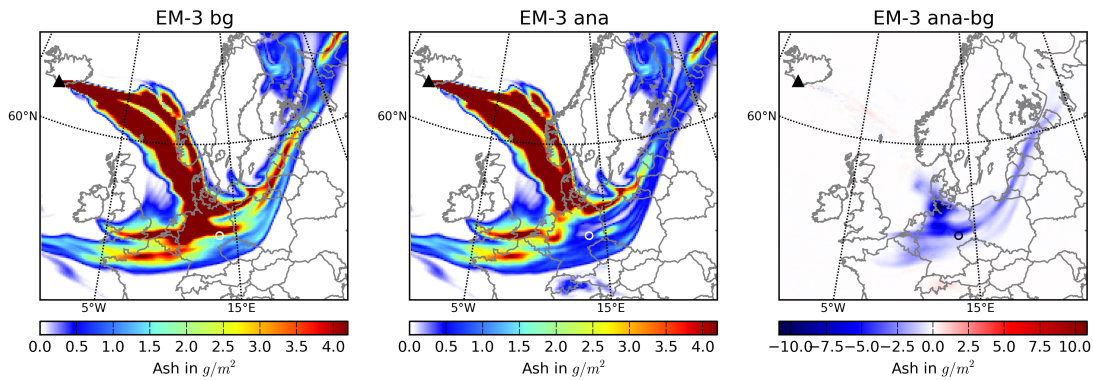


**Figure A.10:** Horizontal ash distribution above Europe on 16 April at 13 UTC as displayed in Figure 7.15 but for EM-3. The 4D-var analysis applies SEVIRI and CALIOP retrievals.

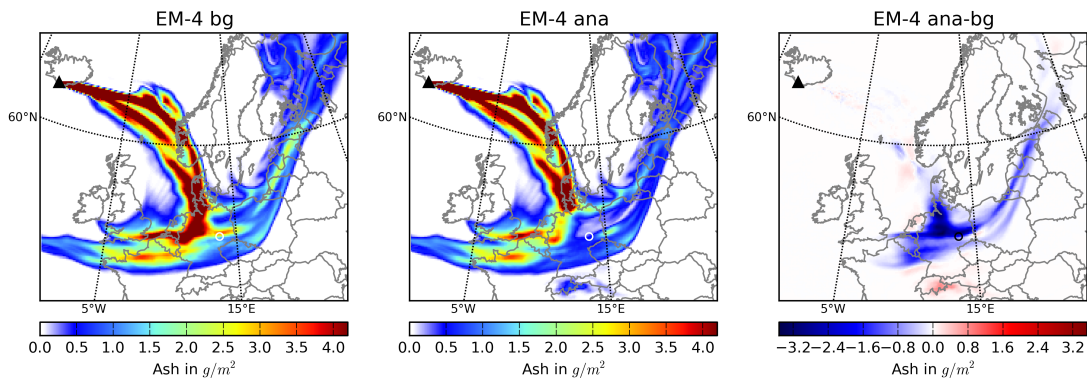


**Figure A.11:** Horizontal ash distribution above Europe on 16 April at 13 UTC as displayed in Figure 7.15 but for EM-4. The 4D-var analysis applies SEVIRI and CALIOP retrievals.

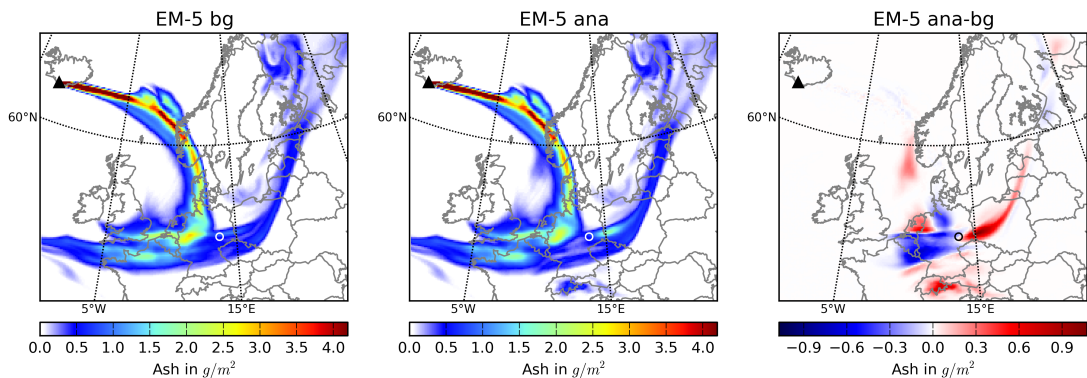


**Figure A.12:** Horizontal ash distribution above Europe on 16 April at 13 UTC as displayed in Figure 7.15 but for EM-5. The 4D-var analysis applies SEVIRI and CALIOP retrievals.

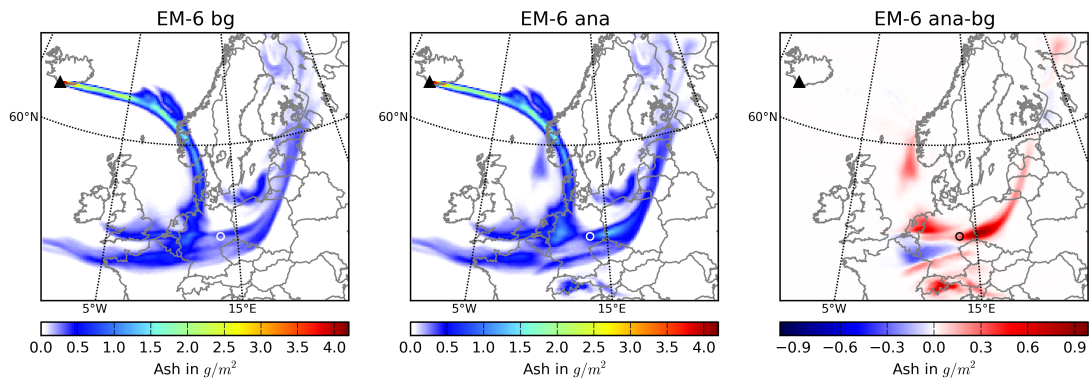


**Figure A.13:** Horizontal ash distribution above Europe on 16 April at 13 UTC as displayed in Figure 7.15 but for EM-6. The 4D-var analysis applies SEVIRI and CALIOP retrievals.

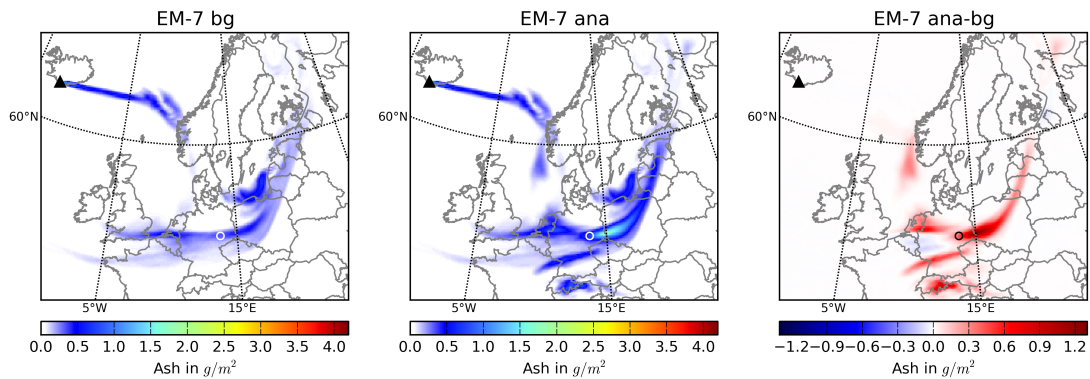


**Figure A.14:** Horizontal ash distribution above Europe on 16 April at 13 UTC as displayed in Figure 7.15 but for EM-7. The 4D-var analysis applies SEVIRI and CALIOP retrievals.

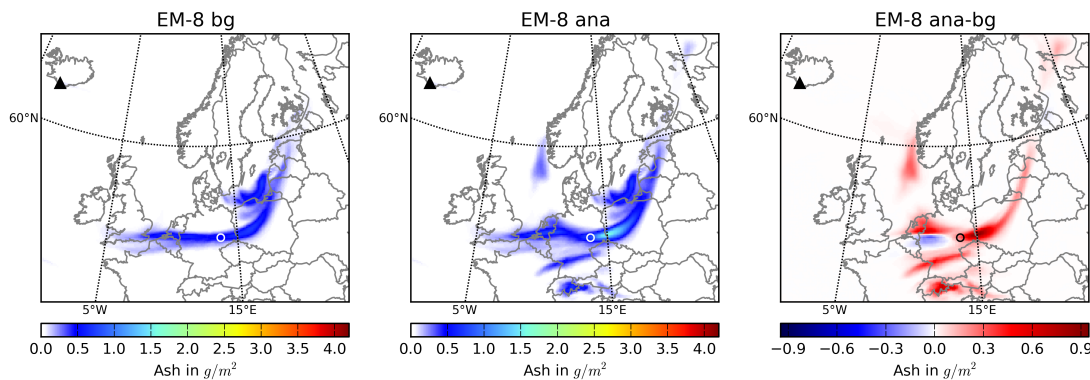


**Figure A.15:** Horizontal ash distribution above Europe on 16 April at 13 UTC as displayed in Figure 7.15 but for EM-8. The 4D-var analysis applies SEVIRI and CALIOP retrievals.

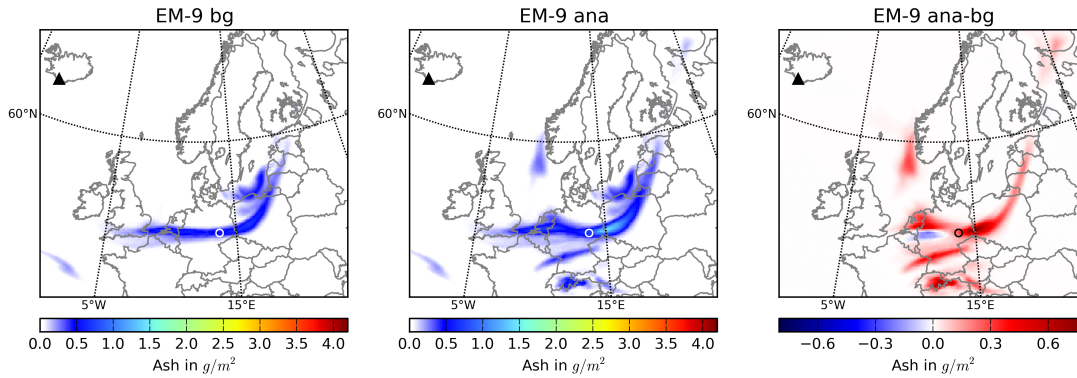


**Figure A.16:** Horizontal ash distribution above Europe on 16 April at 13 UTC as displayed in Figure 7.15 but for EM-9. The 4D-var analysis applies SEVIRI and CALIOP retrievals.

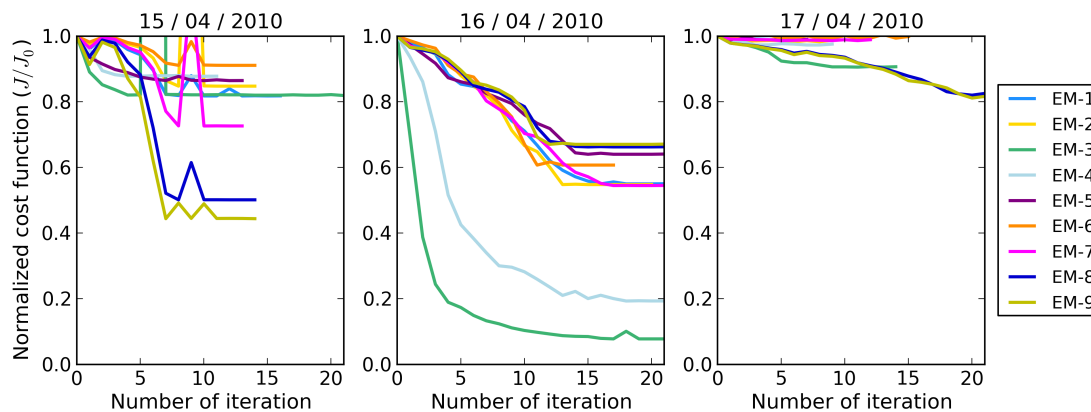


**Figure A.17:** Iterative evolution of normalized cost function (costs  $J$  divided by the initial background costs  $J_0$ ) for the nine members of the 4D-var ensemble. The observation quantity applied in the analyses on 15 April (left), 16 April (center), and 17 April (right) differ markedly, counting 20 308, 44 475, and 12 832 SEVIRI and CALIOP retrievals within the 24-hours assimilation windows, respectively.

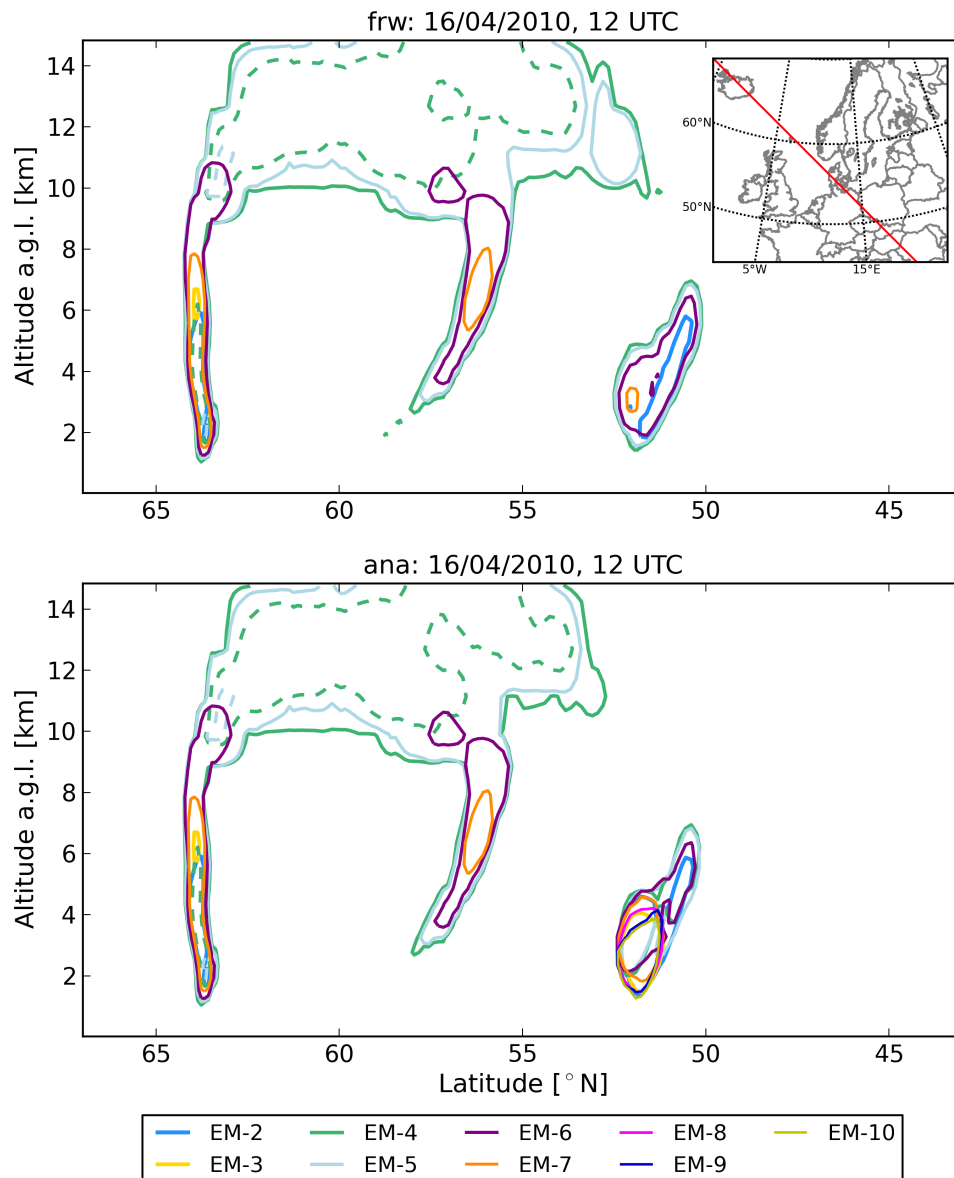


**Figure A.18:** Spaghetti plots of  $0.2 \text{ mg m}^{-3}$  (solid lines) and  $2.0 \text{ mg m}^{-3}$  (dashed lines) volcanic ash concentration isopleths as vertical cross section for all nine 4D-var ensemble members: first guess (top) and analysis (bottom) on 16 April at 12 UTC are depicted along the red line illustrated in the map inlay of the top panel. The ensemble analysis is based on the assimilation of SEVIRI and CALIOP data.

### A.3 Supplements to the ESIAS-chem ensemble analysis using SEVIRI retrievals

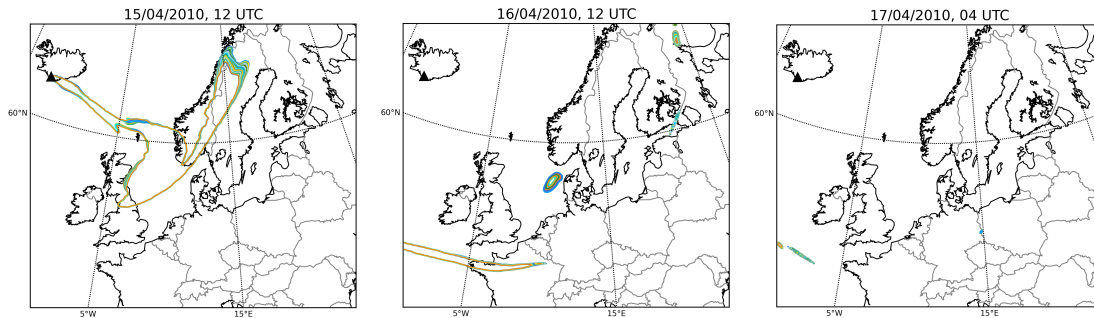


**Figure A.19:** Spaghetti plots of  $1.0 \text{ g m}^{-2}$  volcanic ash column mass loadings for the PS ensemble analysis SEVIRI-2 with 60 ensemble members on 15 April at 12 UTC, 16 April at 12 UTC, and 17 April at 04 UTC. The PS ensemble analysis is based on the assimilation of SEVIRI data  $> 0.45 \text{ g m}^{-2}$ .

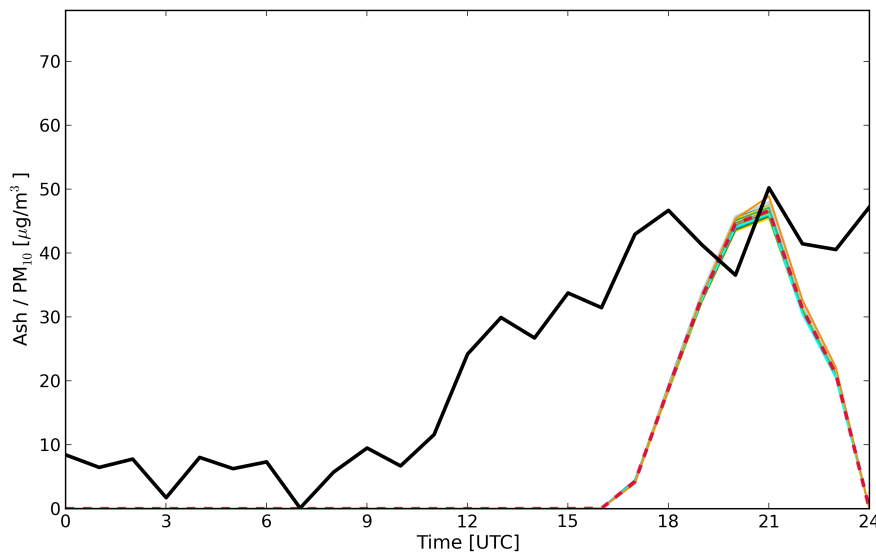


**Figure A.20:** Comparison of  $\text{PM}_{10}$  observations (black line) with the PS ensemble analysis SEVIRI-1 of volcanic ash concentrations (60 ensemble members in colored lines) at Schneefernerhaus (Zugspitze) on 17 April 2010. The ensemble mean of the SEVIRI-1 analysis is depicted as red dashed line.

# Bibliography

- Abida, R. and M. Bocquet**, Targeting of observations for accidental atmospheric release monitoring, *Atmos. Environ.*, *43*, (40), 6312 – 6327, 2009.
- Ackermann, I. J.**, *MADE: Entwicklung und Anwendung eines Aerosol-Dynamikmodells für dreidimensionale Chemie-Transport-Simulationen in der Troposphäre*, Ph.D. Thesis, Institut für Geophysik und Meteorologie der Universität zu Köln, 1997.
- Ackermann, I. J., H. Hass, M. Memmesheimer, A. Ebel, F. S. Binkowski and U. Shankar**, Modal Aerosol Dynamics model for Europe: Development and first applications, *Atmos. Environ.*, *32*, 2981–2999, 1998.
- Adachi, K., M. Kajino, Y. Zaizen and Y. Igarashi**, Emission of spherical cesium-bearing particles from an early stage of the Fukushima nuclear accident, *Scient. Reports*, *3*, 2013.
- Aminou, D. M. A.**, MSG's SEVIRI instrument, *ESA Bulletin*, *111*, 15–17, 2002.
- Andreae, M. O. and P. Merlet**, Emission of trace gases and aerosols from biomass burning, *Global Biogeochem. Cycles*, *15*, (4), 955–966, 2001.
- Ansmann, A., M. Tesche, S. Gross, V. Freudenthaler, P. Seifert, A. Hiebsch, J. Schmidt, U. Wandinger, I. Mattis, M. D. and M. Wiegner**, The 16 April 2010 major volcanic ash plume over central Europe: EARLINET lidar and AERONET photometer observations at Leipzig and Munich, Germany, *Geophys. Res. Lett.*, *37*, 2010.
- Ansmann, A., M. Tesche, P. Seifert, S. Groß, V. Freudenthaler, A. Apituley, K. M. Wilson, I. Serikov, H. Linné, B. Heinold, A. Hiebsch, F. Schnell, J. Schmidt, I. Mattis, U. Wandinger and M. Wiegner**, Ash and fine-mode particle mass profiles from EARLINET–AERONET observations over central Europe after the eruptions of the Eyjafjallajökull volcano in 2010, *J. Geophys. Res.: Atmos.*, *116*, (D20), 2011.
- Ansmann, A., P. Seifert, M. Tesche and U. Wandinger**, Profiling of fine and coarse particle mass: case studies of saharan dust and Eyjafjallajökull/Grimsvötn volcanic plumes, *Atmos. Chem. Phys.*, *12*, (20), 9399–9415, 2012.
- Arason, P., G. N. Petersen and H. Bjornsson**, Observations of the altitude of the volcanic plume during the eruption of Eyjafjallajökull, April-May 2010, *Earth Sys. Sci. Data*, *3*, (1), 9–17, 2011.

- Argyris, J., G. Faust, M. Haase and R. Friedrich**, *Die Erforschung des Chaos - Eine Einführung in die Theorie nichtlinearer Systeme*, Springer-Verlag Berlin Heidelberg, 2010.
- Baker, N. L. and R. Daley**, Observation and background adjoint sensitivity in the adaptive observation-targeting problem, *Q. J. Royal Meteorol. Soc.*, *126*, (565), 1431–1454, 2000.
- Banks, J. and H. Brindley**, Evaluation of MSG-SEVIRI mineral dust retrieval products over North Africa and the Middle East, *Remote Sens. Environ.*, *128*, (Supplement C), 58 – 73, 2013.
- Batista, P., C. Silvestre and P. Oliveira**, On the observability of linear motion quantities in navigation systems, *Systems Control Lett.*, *60*, (2), 101 – 110, 2011.
- Bauer, S. E., Y. Balkanski, M. Schulz, D. A. Hauglustaine and F. Dentener**, Global modeling of heterogeneous chemistry on mineral aerosol surfaces: Influence on tropospheric ozone chemistry and comparison to observations, *J. Geophys. Res.: Atmos.*, *109*, (D2), 2004.
- Benedetti, A., J. W. Kaiser, J.-J. Morcrette, R. Eresmaa and S. Lu**, Simulations of volcanic plumes with the ECMWF/MACC aerosol system, *ECMWF Techn. Memo.*, *653*, 2011.
- Berndt, J.**, *On the predictability of exceptional error events in wind power forecasting – an ultra large ensemble approach –*, Ph.D. Thesis, Institut für Geophysik und Meteorologie der Universität zu Köln, 2018.
- Bielli, S., M. Grzeschik, E. Richard, C. Flamant, C. Champollion, C. Kiemle, M. Dorninger and P. Brousseau**, Assimilation of water-vapour airborne lidar observations: impact study on the COPS precipitation forecasts, *Q. J. Royal Meteorol. Soc.*, *138*, (667), 1652–1667, 2012.
- Boucher, O., D. Randall, P. Artaxo, C. Bretherton, G. Feingold, P. Forster, V.-M. Kerminen, Y. Kondo, H. Liao, U. Lohmann, P. Rasch, S. K. Satheesh, S. Sherwood, B. Stevens and X. Y. Zhang**, Clouds and Aerosols, in *Climate Change 2013: The Physical Science Basis. Contribution of Working Group I to the Fifth Assessment Report of the Intergovernmental Panel on Climate Change*, edited by T. Stocker, D. Qin, G.-K. Plattner, M. Tignor, S. Allen, J. Boschung, A. Nauels, Y. Xia, V. Bex, and P. Midgley, Cambridge Univ. Press, Cambridge, UK and New York, USA, 2013.
- Bouttier, F. and P. Courtier**, Data assimilation concepts and methods, ECMWF Meteorological Training Course Lecture Series, 1999.
- Bouttier, F. and G. Kelly**, Observing-system experiments in the ECMWF 4D-var data assimilation system, *Q. J. Royal Meteorol. Soc.*, *127*, (574), 1469–1488, 2001.
- Brewer, J., Z. Huang, A. K. Singh, M. Misra and J. Hahn**, Sensor network design via observability analysis and principal component analysis, *Ind. Eng. Chem. Res.*, *46*, (24), 8026–8032, 2007.

- Buizza, R., P. L. Houtekamer, G. Pellerin, Z. Toth, Y. Zhu and M. Wei**, A comparison of the ecmwf, msc, and ncep global ensemble prediction systems, *Month. Weath. Rev.*, *133*, (5), 1076–1097, 2005.
- Buizza, R., C. Cardinali, G. Kelly and J.-N. Thépaut**, The value of observations part II: The value of observations located in singular-vector-based target areas, *Q. J. Royal Meteorol. Soc.*, *133*, (628), 1817–1832, 2007.
- Burton, M.**, Chapter 10 - Quantitative ground-based imaging of volcanic ash, in *Volcanic Ash*, edited by S. Mackie, K. Cashman, H. Ricketts, A. Rust, and M. Watson, 175 – 185, Elsevier, 2016.
- Burton, M., F. Prata and U. Platt**, Volcanological applications of so2 cameras, *J. Volcanol. Geotherm. Res.*, *300*, (Supplement C), 2 – 6, 2015.
- CALIPSO Science Team**, CALIPSO/CALIOP Level 2, Lidar Aerosol Profile Data, version 4.10, *NASA Atmospheric Science Data Center (ASDC)*, Accessed 14 July 2017, Hampton, VA, USA, 2016.
- Cardinali, C.**, Monitoring the observation impact on the short-range forecast, *Q. J. Royal Meteorol. Soc.*, *135*, (638), 239–250, 2009.
- Cashman, K. and A. Rust**, Volcanic ash: Generation and spatial variations, in *Volcanic Ash*, edited by S. Mackie, K. Cashman, H. Ricketts, A. Rust, and M. Watson, 5 – 22, Elsevier, 2016.
- Chester, D. K.**, Volcanoes, society, and culture, in *Volcanoes and the Environment*, 404–439, Cambridge Univ. Press, 2005.
- Clarisse, L., F. Prata, J.-L. Lacour, D. Hurtmans, C. Clerbaux and P.-F. Coheur**, A correlation method for volcanic ash detection using hyperspectral infrared measurements, *Geophys. Res. Lett.*, *37*, (19), 2010.
- Courtier, P., J.-N. Thépaut and A. Hollingsworth**, A strategy for operational implementation of 4D-Var, using an incremental approach, *Q. J. Royal Meteorol. Soc.*, *120*, (519), 1367–1387, 1994.
- Daley, R.**, *Atmospheric data analysis*, Cambridge Univ. Press, 1991.
- Denlinger, R. P., M. Pavolonis and J. Sieglaff**, A robust method to forecast volcanic ash clouds, *J. Geophys. Res.: Atmos.*, *117*, (D13), 2012.
- Dubuisson, P., H. Herbin, F. Minvielle, M. Compiègne, F. Thieuleux, F. Parol and J. Pelon**, Remote sensing of volcanic ash plumes from thermal infrared: a case study analysis from SEVIRI, MODIS and IASI instruments, *Atmos. Meas. Tech.*, *7*, (2), 359–371, 2014.
- Ebel, A., H. Elbern, H. Feldmann, H. J. Jakobs, C. Kessler, M. Memmesheimer, A. Oberreuter and G. Piekorz**, *Air pollution studies with the EURAD model system (3)*, vol 120, Mitteilungen aus dem Institut für Geophysik und Meteorologie der Universität zu Köln, 1997.

- Eckhardt, S., A. J. Prata, P. Seibert, K. Stebel and A. Stohl**, Estimation of the vertical profile of sulfur dioxide injection into the atmosphere by a volcanic eruption using satellite column measurements and inverse transport modeling, *Atmos. Chem. Phys.*, 8, (14), 3881–3897, 2008.
- Elbern, H. and H. Schmidt**, Ozone episode analysis by four-dimensional variational chemistry data assimilation, *J. Geophys. Res.: Atmos.*, 106, (D4), 3569–3590, 2001.
- Elbern, H. and H. Schmidt**, Chemical 4D variational data assimilation and its numerical implications for case study analyses, in *IMA volumes in Mathematics and its Applications, Atmospheric Modeling*, edited by D. P. Chock and G. R. Carmichael, vol 130, 165–184, 2002.
- Elbern, H., H. Schmidt and A. Ebel**, Variational data assimilation for tropospheric chemistry modeling, *J. Geophys. Res.*, 102, (D13), 15,967–15,985, 1997.
- Elbern, H., H. Schmidt, O. Talagrand and A. Ebel**, 4D-variational data assimilation with an adjoint air quality model for emission analysis, *Environ. Model. and Software*, 15, (6), 539–548, 2000.
- Elbern, H., A. Strunk, H. Schmidt and O. Talagrand**, Emission rate and chemical state estimation by 4-dimensional variational inversion, *Atmos. Chem. Phys.*, 7, (14), 3749–3769, 2007.
- Engelen, R. J. and A. P. McNally**, Estimating atmospheric CO<sub>2</sub> from advanced infrared satellite radiances within an operational four-dimensional variational (4D-Var) data assimilation system: Results and validation, *J. Geophys. Res.: Atmos.*, 110, (D18), 2005.
- ESA**, Artist’s view of Meteosat Second Generation (MSG), [http://www.esa.int/spaceinimages/Images/2002/07/Meteosat\\_Second\\_Generation](http://www.esa.int/spaceinimages/Images/2002/07/Meteosat_Second_Generation), accessed 29 Sep 2017, 2002.
- Evensen, G.**, *Data assimilation: the ensemble Kalman filter*, Springer Science & Business Media, 2009.
- Flemming, J. and A. Inness**, Volcanic sulfur dioxide plume forecasts based on UV satellite retrievals for the 2011 Grímsvötn and the 2010 Eyjafjallajökull eruption, *J. Geophys. Res.: Atmos.*, 118, (17), 10,172–10,189, 2013.
- Flentje, H., H. Claude, T. Elste, S. Gilge, U. Köhler, C. Plass-Dülmer, W. Steinbrecht, W. Thomas, A. Werner and W. Fricke**, The Eyjafjallajökull eruption in April 2010 - detection of volcanic plume using in-situ measurements, ozone sondes and lidar-ceilometer profiles, *Academic Press*, 10, 10085–10092, 2010.
- Folch, A., A. Costa and G. Macedonio**, FPLUME-1.0: an integral volcanic plume model accounting for ash aggregation, *Geosci. Model Dev.*, 9, (1), 431–450, 2016.
- Formenti, P., W. Elbert, W. Maenhaut, J. Haywood and M. O. Andreae**, Chemical composition of mineral dust aerosol during the Saharan Dust Experiment (SHADE) airborne campaign in the Cape Verde region, September 2000, *J. Geophys. Res.: Atmos.*, 108, (D18), 2003.

- Fourrié, N., D. Marchal, F. Rabier, B. Chapnik and G. Desroziers**, Impact study of the 2003 North Atlantic THORPEX Regional Campaign, *Q. J. Royal Meteorol. Soc.*, *132*, (615), 275–295, 2006.
- Francis, P. N., M. C. Cooke and R. W. Saunders**, Retrieval of physical properties of volcanic ash using Meteosat: A case study from the 2010 Eyjafjallajökull eruption, *J. Geophys. Res.: Atmos.*, *117*, (D20), 2012.
- Franke, P.**, *Quantitative estimation of unexpected emissions in the atmosphere by stochastic inversion techniques*, Ph.D. Thesis, Institut für Geophysik und Meteorologie der Universität zu Köln, 2018.
- Freitas, S. R., K. M. Longo, R. Chatfield, D. Latham, M. A. F. Silva Dias, M. O. Andreae, E. Prins, J. C. Santos, R. Gielow and J. A. Carvalho Jr.**, Including the sub-grid scale plume rise of vegetation fires in low resolution atmospheric transport models, *Atmos. Chem. Phys.*, *7*, (13), 3385–3398, 2007.
- Friedlander, S. K.**, *Smoke, Dust and Haze*, John Wiley and Sons, New York, 1977.
- Fu, G., A. Heemink, S. Lu, A. Segers, K. Weber and H.-X. Lin**, Model-based aviation advice on distal volcanic ash clouds by assimilating aircraft in situ measurements, *Atmos. Chem. Phys.*, *16*, (14), 9189–9200, 2016.
- Fu, G., F. Prata, H. X. Lin, A. Heemink, A. Segers and S. Lu**, Data assimilation for volcanic ash plumes using a satellite observational operator: a case study on the 2010 Eyjafjallajökull volcanic eruption, *Atmos. Chem. Phys.*, *17*, (2), 1187–1205, 2017.
- Fulle, M.**, Massive ash emission from the Eyjafjallajökull eruption, [http://www.swisseduc.ch/stromboli/perm/iceland/eyafallajokull\\_20100416-en.html?id=1](http://www.swisseduc.ch/stromboli/perm/iceland/eyafallajokull_20100416-en.html?id=1), accessed 24 Oct 2017, 2010.
- Galmarini, S., R. Bianconi, R. Bellasio and G. Graziani**, Forecasting the consequences of accidental releases of radionuclides in the atmosphere from ensemble dispersion modelling, *J. Environ. Radioact.*, *57*, (3), 203 – 219, 2001.
- Gasteiger, J., S. Gross, V. Freudenthaler and M. Wiegner**, Volcanic ash from Iceland over Munich: mass concentration retrieved from ground-based remote sensing measurements, *Atmos. Chem. Phys.*, *11*, (5), 2209–2223, 2011.
- Geiger, H., I. Barnes, I. Bejan, T. Benter and M. Spittler**, The tropospheric degradation of isoprene: an updated module for the regional atmospheric chemistry mechanism, *Atmos. Environ.*, *37*, (11), 1503 – 1519, 2003.
- Gelaro, R., R. H. Langland, S. Pellerin and R. Todling**, The THORPEX observation impact intercomparison experiment, *Month. Weath. Rev.*, *138*, (11), 4009–4025, 2010.
- Goris, N. and H. Elbern**, Singular vector decomposition for sensitivity analyses of tropospheric chemical scenarios, *Atmos. Chem. Phys.*, *13*, (9), 5063–5087, 2013.
- Goris, N. and H. Elbern**, Singular vector-based targeted observations of chemical constituents: description and first application of the EURAD-IM-SVA v1.0, *Geosci. Model Dev.*, *8*, (12), 3929–3945, 2015.

- Grattan, J. P. and F. B. Pyatt**, Acid damage to vegetation following the Laki fissure eruption in 1783 – an historical review, *Sci. Total Environ.*, 151, (3), 241–247, 1994.
- Griffin, D. W. and C. A. Kellogg**, Dust storms and their impact on ocean and human health: Dust in Earth’s atmosphere, *EcoHealth*, 1, (3), 284–295, 2004.
- Grimit, E. P. and C. F. Mass**, Measuring the ensemble spread-error relationship with a probabilistic approach: Stochastic ensemble results, *Month. Weath. Rev.*, 135, (1), 203–221, 2007.
- Groß S., J. Gasteiger, V. Freudenthaler, F. Schnell and M. Wiegner**, Characterization of the Eyjafjallajökull ash-plume by means of lidar measurements over the Munich EARLINET-site, vol 7832, 2010.
- Gudmundsson, M. T., T. Thordarson, A. Höskuldsson, G. Larsen, H. Björnsson, F. J. Prata, B. Oddsson, E. Magnússon, T. Högnadóttir, G. N. Petersen, C. L. Hayward, J. A. Stevenson and I. Jónsdóttir**, Ash generation and distribution from the April-May 2010 eruption of Eyjafjallajökull, Iceland, *Scient. Reports*, 2, (572), 2012.
- Hansell, A. L., C. J. Horwell and C. Oppenheimer**, The health hazards of volcanoes and geothermal areas, *Occup. Environ. Med.*, 63, (2), 149–156, 2006.
- Hass, H.**, *Description of the EURAD Chemistry–Transport–Model Version 2 (CTM2)*, vol 83, Mitteilungen aus dem Institut für Geophysik und Meteorologie der Universität zu Köln, 1991.
- Hendricks, J., M. Righi and V. Aquila**, Global atmospheric aerosol modeling, in *Atmospheric Physics: Background – Methods – Trends*, edited by U. Schumann, 561–576, Springer Berlin Heidelberg, Berlin, Heidelberg, 2012.
- Hoffman, R. N. and R. Atlas**, Future observing system simulation experiments, *Bull. Amer. Meteor. Soc.*, 97, (9), 1601–1616, 2016.
- Hughes, E. J., J. Yorks, N. A. Krotkov, A. M. da Silva and M. McGill**, Using CATS near-real-time lidar observations to monitor and constrain volcanic sulfur dioxide (SO<sub>2</sub>) forecasts, *Geophys. Res. Lett.*, 43, (20), 11,089–11,097, 2016.
- Huijnen, V., H. J. Eskes, A. Poupkou, H. Elbern, K. F. Boersma, G. Foret, M. Sofiev, A. Valdebenito, J. Flemming, O. Stein, A. Gross, L. Robertson, M. D’Isidoro, I. Kioutsioukis, E. Friese, B. Amstrup, R. Bergstrom, A. Strunk, J. Vira, D. Zyryanov, A. Maurizi, D. Melas, V.-H. Peuch and C. Zerefos**, Comparison of OMI NO<sub>2</sub> tropospheric columns with an ensemble of global and European regional air quality models, *Atmos. Chem. Phys.*, 10, (7), 3273–3296, 2010.
- Hunt, B. R., E. J. Kostelich and I. Szunyogh**, Efficient data assimilation for spatiotemporal chaos: A local ensemble transform Kalman filter, *Physica D: Nonlinear Phenomena*, 230, (1), 112 – 126, 2007.

- Hunt, W. H., D. M. Winker, M. A. Vaughan, K. A. Powell, P. L. Lucker and C. Weimer, CALIPSO Lidar description and performance assessment, *J. Atmos. Ocean. Technol.*, 26, (7), 1214–1228, 2009.
- Joly, A., K. A. Browning, P. Bessemoulin, J.-P. Cammas, G. Caniaux, J.-P. Chalon, S. A. Clough, R. Dirks, K. A. Emanuel, L. Eymard, R. Gall, T. D. Hewson, P. H. Hildebrand, D. Jorgensen, F. Lalaurette, R. H. Langland, Y. Lemaître, P. Mascart, J. A. Moore, P. O. Persson, F. Roux, M. A. Shapiro, C. Snyder, Z. Toth and R. M. Wakimoto, Overview of the field phase of the fronts and Atlantic Storm-Track EXperiment (FASTEX) project, *Q. J. Royal Meteorol. Soc.*, 125, (561), 3131–3163, 1999.
- Jülich Supercomputing Centre, JUQUEEN: IBM Blue Gene/Q Supercomputer System at the Jülich Supercomputing Centre, *Journal of large-scale research facilities*, 1, (A1), 2015.
- Jülich Supercomputing Centre, JURECA: General-purpose supercomputer at Jülich Supercomputing Centre, *Journal of large-scale research facilities*, 2, (A62), 2016.
- Kahn, R. A. and J. Limbacher, Eyjafjallajökull volcano plume particle-type characterization from space-based multi-angle imaging, *Atmos. Chem. Phys.*, 12, (20), 9459–9477, 2012.
- Kahnert, M., On the observability of chemical and physical aerosol properties by optical observations: inverse modelling with variational data assimilation, *Tellus*, 61, (5), 2009.
- Kalnay, E., *Atmospheric modeling, data assimilation, and predictability*, Cambridge Univ. Press, 2003.
- Kalnay, E., Y. Ota, T. Miyoshi and J. Liu, A simpler formulation of forecast sensitivity to observations: application to ensemble Kalman filters, *Tellus A*, 64, (0), 2012.
- Keiding, J. K. and O. Sigmarsson, Geothermobarometry of the 2010 Eyjafjallajökull eruption: New constraints on Icelandic magma plumbing systems, *J. Geophys. Res.: Sol. Earth*, 117, (B9), 2012.
- Khattatov, B. V., J. C. Gille, L. V. Lyjak, G. P. Brasseur, V. L. Dvortsov, A. E. Roche and J. W. Waters, Assimilation of photochemically active species and a case analysis of UARS data, *J. Geophys. Res.: Atmos.*, 104, (D15), 18715–18737, 1999.
- Kim, Y. H., H. Tong, M. Daniels, E. Boykin, Q. T. Krantz, J. McGee, M. Hays, K. Kovalcik, J. A. Dye and M. I. Gilmour, Cardiopulmonary toxicity of peat wildfire particulate matter and the predictive utility of precision cut lung slices, *Part. Fibre Toxicol.*, 11, (1), 29, 2014.
- King, S., W. Kang and L. Xu, Observability for optimal sensor locations in data assimilation, *Int. J. Dynam. Control*, 3, (4), 416–424, 2015.
- Klose, M. and Y. Shao, Large-eddy simulation of turbulent dust emission, *Aeolian Res.*, 8, (Supplement C), 49 – 58, 2013.

- König, M. and E. de Coning, The MSG global instability indices product and its use as a nowcasting tool, *Weather Forecast.*, 24, (1), 272–285, 2009.
- Kristiansen, N. I., A. Stohl, A. J. Prata, A. Richter, S. Eckhardt, P. Seibert, A. Hoffmann, C. Ritter, L. Bitar, T. J. Duck and K. Stebel, Remote sensing and inverse transport modeling of the Kasatochi eruption sulfur dioxide cloud, *J. Geophys. Res.: Atmos.*, 115, (D2), 2010.
- Kristiansen, N. I., A. Stohl, A. J. Prata, N. Bukowiecki, H. Dacre, S. Eckhardt, S. Henne, M. C. Hort, B. T. Johnson, F. Marenco, B. Neininger, O. Reitebuch, P. Seibert, D. J. Thomson, H. N. Webster and B. Weinzierl, Performance assessment of a volcanic ash transport model mini-ensemble used for inverse modeling of the 2010 Eyjafjallajökull eruption, *J. Geophys. Res.: Atmos.*, 117, (D20), 2012.
- Kylling, A., M. Kahnert, H. Lindqvist and T. Nousiainen, Volcanic ash infrared signature: porous non-spherical ash particle shapes compared to homogeneous spherical ash particles, *Atmos. Meas. Tech.*, 7, (4), 919–929, 2014.
- Kylling, A., N. Kristiansen, A. Stohl, R. Buras-Schnell, C. Emde and J. Gasteiger, A model sensitivity study of the impact of clouds on satellite detection and retrieval of volcanic ash, *Atmos. Meas. Tech.*, 8, (5), 1935–1949, 2015.
- Lahoz, W. A., B. Khattatov and R. Mâenard, *Data assimilation: making sense of observations*, Springer, 2010.
- Lahoz, W. A., V.-H. Peuch, J. Orphal, J.-L. Attié, K. Chance, X. Liu, D. Edwards, H. Elbern, J.-M. Flaud, M. Claeysman and L. E. Amraoui, Monitoring air quality from space: The case for the geostationary platform, *Bull. Amer. Meteor. Soc.*, 93, (2), 221–233, 2012.
- Langland, R. H., Issues in targeted observing, *Q. J. Royal Meteorol. Soc.*, 131, (613), 3409–3425, 2005.
- Langland, R. H. and N. L. Baker, Estimation of observation impact using the NRL atmospheric variational data assimilation adjoint system, *Tellus A*, 56, (3), 189–201, 2004.
- Langland, R. H., Z. Toth, R. Gelaro, I. Szunyogh, M. A. Shapiro, S. J. Majumdar, R. E. Morss, G. D. Rohaly, C. Velden, N. Bond and C. H. Bishop, The North Pacific Experiment (NORPEX-98): Targeted observations for improved North American weather forecasts, *Bull. Amer. Meteor. Soc.*, 80, (7), 1363–1384, 1999.
- Langmann, B., B. Duncan, C. Textor, J. Trentmann and G. R. van der Werf, Vegetation fire emissions and their impact on air pollution and climate, *Atmos. Environ.*, 43, (1), 107 – 116, 2009.
- Langmann, B., A. Folch, M. Hensch and V. Matthias, Volcanic ash over Europe during the eruption of Eyjafjallajökull on Iceland, April-May 2010, *Atmos. Environ.*, 48, (Supplement C), 1 – 8, 2012.

- Lee, K. H., Z. Li, Y. J. Kim and A. Kokhanovsky, Atmospheric aerosol monitoring from satellite observations: A history of three decades, in *Atmospheric and Biological Environmental Monitoring*, edited by Y. J. Kim, U. Platt, M. B. Gu, and H. Iwahashi, 13–38, Springer Netherlands, Dordrecht, 2009.
- Liao, W., A. Sandu, G. R. Carmichael and T. Chai, Singular vector analysis for atmospheric chemical transport models, *Month. Weath. Rev.*, *134*, (9), 2443–2465, 2006.
- Li, Y. P., H. Elbern, K. D. Lu, E. Friese, A. Kiendler-Scharr, T. F. Mentel, X. S. Wang, A. Wahner and Y. H. Zhang, Updated aerosol module and its application to simulate secondary organic aerosols during impact campaign may 2008, *Atmos. Chem. Phys.*, *13*, (13), 6289–6304, 2013.
- Li, T., S. Sun, T. P. Sattar and J. M. Corchado, Fight sample degeneracy and impoverishment in particle filters: A review of intelligent approaches, *Expert Syst. Appl.*, *41*, (8), 3944 – 3954, 2014.
- Liu, D. C. and J. Nocedal, On the limited memory BFGS method for large scale optimization, *Math. Programming*, *45*, 503–528, 1989.
- Liu, Z., M. Vaughan, D. Winker, C. Kittaka, B. Getzewich, R. Kuehn, A. Omar, K. Powell, C. Trepte and C. Hostetler, The CALIPSO lidar cloud and aerosol discrimination: Version 2 algorithm and initial assessment of performance, *J. Atmos. Ocean. Technol.*, *26*, (7), 1198–1213, 2009.
- Lorenc, A. C., Modelling of error covariances by 4d-var data assimilation, *Q. J. Royal Meteorol. Soc.*, *129*, (595), 3167–3182, 2003.
- Lorenz, E. N., Deterministic nonperiodic flow, *J. Atmospheric Sci.*, *20*, 130–141, 1963.
- Lorenz, E. N., A study of the predictability of a 28-variable atmospheric model, *Tellus*, *17*, (3), 321–333, 1965.
- Lu, S., H. X. Lin, A. W. Heemink, G. Fu and A. J. Segers, Estimation of volcanic ash emissions using trajectory-based 4D-var data assimilation, *Month. Weath. Rev.*, *144*, (2), 575–589, 2016.
- Mackie, S. and M. Watson, Probabilistic detection of volcanic ash using a Bayesian approach, *J. Geophys. Res.: Atmos.*, *119*, (5), 2409–2428, 2014.
- Majumdar, S. J., A review of targeted observations, *Bull. Amer. Meteor. Soc.*, *97*, (12), 2287–2303, 2016.
- Majumdar, S. J., S. Aberson, C. Bishop, C. Cardinali, J. Caughey, A. Doerenbecher, P. Gauthier, R. Gelaro, T. Hamill, R. Langland et al., Targeted observations for improving numerical weather prediction: an overview, *World Weath. Res. Programme/THORPEX Pub.*, *15*, 37, 2011.
- Marécal, V., V.-H. Peuch, C. Andersson, S. Andersson, J. Arteta, M. Beekmann, A. Benedictow, R. Bergström, B. Bessagnet, A. Cansado, F. Chéroux, A. Colette, A. Coman, R. L. Curier, H. A. C. Denier van der Gon, A. Drouin, H. Elbern, E. Emili, R. J. Engelen, H. J. Eskes, G. Foret, E. Friese, M. Gauss,

- C. Giannaros, J. Guth, M. Joly, E. Jaumouillé, B. Josse, N. Kadygrov, J. W. Kaiser, K. Krajsek, J. Kuenen, U. Kumar, N. Liora, E. Lopez, L. Malherbe, I. Martinez, D. Melas, F. Meleux, L. Menut, P. Moinat, T. Morales, J. Parmentier, A. Piacentini, M. Plu, A. Poupkou, S. Queguiner, L. Robertson, L. Rouil, M. Schaap, A. Segers, M. Sofiev, L. Tarasson, M. Thomas, R. Timmermans, A. Valdebenito, P. van Velthoven, R. van Versendaal, J. Vira and A. Ung, A regional air quality forecasting system over Europe: the MACC-II daily ensemble production, *Geosci. Model Dev.*, 8, (9), 2777–2813, 2015.
- Martin, J. H. and S. E. Fitzwater, Iron deficiency limits phytoplankton growth in the north-east Pacific subarctic, *Nature*, 331, (6154), 341–343, 1988.
- Mastin, L., M. Guffanti, R. Servranckx, P. Webley, S. Barsotti, K. Dean, A. Durant, J. Ewert, A. Neri, W. Rose, D. Schneider, L. Siebert, B. Stunder, G. Swanson, A. Tupper, A. Volentik and C. Waythomas, A multidisciplinary effort to assign realistic source parameters to models of volcanic ash-cloud transport and dispersion during eruptions, *J. Volcanol. Geotherm. Res.*, 186, (1), 10 – 21, 2009.
- McRae, G. J., W. R. Goodin and J. H. Seinfeld, Numerical solution of the atmospheric diffusion equation for chemically reacting flows, *J. Comp. Phys.*, 45, (1), 1 – 42, 1982.
- Memmesheimer, M., J. Tippke, A. Ebel, H. Hass, H. J. Jakobs and M. Laube, On the use of EMEP emission inventories for European scale air pollution modelling with the EURAD model, in *Proceedings of the EMEP workshop on photooxidant modelling for long range transport in relation to abatement strategies*, edited by J. Pankrath, 307–324, UBA, Berlin, 1991.
- Meng, Z., P. Yang, G. W. Kattawar, L. Bi, K. Liou and I. Laszlo, Single-scattering properties of tri-axial ellipsoidal mineral dust aerosols: A database for application to radiative transfer calculations, *J. Aerosol Sci.*, 41, (5), 501 – 512, 2010.
- Millington, S. C., R. W. Saunders, P. N. Francis and H. N. Webster, Simulated volcanic ash imagery: A method to compare NAME ash concentration forecasts with SEVIRI imagery for the Eyjafjallajökull eruption in 2010, *J. Geophys. Res.: Atmos.*, 117, (D20), 2012.
- Minikin, A., A. Petzold, B. Weinzierl and J.-F. Gayet, In situ measurement methods for atmospheric aerosol particles and cloud elements, in *Atmospheric Physics: Background – Methods – Trends*, edited by U. Schumann, 297–315, Springer Berlin Heidelberg, Berlin, Heidelberg, 2012.
- Mishchenko, M. I., L. D. Travis and D. W. Mackowski, T-matrix computations of light scattering by nonspherical particles: A review, *J. Quant. Spectr. Radiat. Transf.*, 55, (5), 535–575, 1996.
- Monteiro, A., I. Ribeiro, O. Tchepel, E. Sá, J. Ferreira, A. Carvalho, V. Martins, A. Strunk, S. Galmarini, H. Elbern, M. Schaap, P. Builtjes, A. I. Miranda and C. Borrego, Bias correction techniques to improve air quality ensemble predictions: Focus on O<sub>3</sub> and PM Over Portugal, *Environ. Model. Assess.*, 18, (5), 533–546, 2013.

- Morcrette, J.-J., O. Boucher, L. Jones, D. Salmond, P. Bechtold, A. Beljaars, A. Benedetti, A. Bonet, J. W. Kaiser, M. Razinger, M. Schulz, S. Serrar, A. J. Simmons, M. Sofiev, M. Suttie, A. M. Tompkins and A. Untch, Aerosol analysis and forecast in the European Centre for Medium-Range Weather Forecasts Integrated Forecast System: Forward modeling, *J. Geophys. Res.: Atmos.*, 114, (D6), 2009.
- Murphy, J. M., D. M. Sexton, D. N. Barnett, G. S. Jones, M. J. Webb, M. Collins and D. A. Stainforth, Quantification of modelling uncertainties in a large ensemble of climate change simulations, *Nature*, 430, (7001), 768–772, 2004.
- Nakamura, G. and R. Potthast, *Inverse Modeling*, 2053-2563, IOP Publishing, 2015.
- NASA, CALIPSO satellite image, [https://www.nasa.gov/images/content/133388main\\_Calipso4\\_print.tif](https://www.nasa.gov/images/content/133388main_Calipso4_print.tif), accessed 02 Oct 2017, 2005.
- NASA, MODIS (Terra) Corrected Reflectance (True Color), [https://worldview.earthdata.nasa.gov/?p=geographic&l=VIIRS\\_SNPP\\_CorrectedReflectance\\_TrueColor\(hidden\),MODIS\\_Aqua\\_CorrectedReflectance\\_TrueColor\(hidden\),MODIS\\_Terra\\_CorrectedReflectance\\_TrueColor,Reference\\_Labels\(hidden\),Reference\\_Features,Coastlines&t=2010-04-17&z=3&v=-61.923096976016666,14.619427789363897,73.07690302398333,82.0491152893639](https://worldview.earthdata.nasa.gov/?p=geographic&l=VIIRS_SNPP_CorrectedReflectance_TrueColor(hidden),MODIS_Aqua_CorrectedReflectance_TrueColor(hidden),MODIS_Terra_CorrectedReflectance_TrueColor,Reference_Labels(hidden),Reference_Features,Coastlines&t=2010-04-17&z=3&v=-61.923096976016666,14.619427789363897,73.07690302398333,82.0491152893639), accessed 23 Oct 2017, 2010.
- Navon, I. M., Data assimilation for numerical weather prediction: A review, in *Data Assimilation for Atmospheric, Oceanic and Hydrologic Applications*, edited by S. K. Park and L. Xu, 21–65, Springer Berlin Heidelberg, Berlin, Heidelberg, 2009.
- Nelder, J. A. and R. Mead, A simplex method for function minimization, *Comput. J.*, 7, (4), 308–313, 1965.
- Newman, S. M., L. Clarisse, D. Hurtmans, F. Marenco, B. Johnson, K. Turnbull, S. Havemann, A. J. Baran, D. O’Sullivan and J. Haywood, A case study of observations of volcanic ash from the Eyjafjalla-jökull eruption: 2. Airborne and satellite radiative measurements, *J. Geophys. Res.: Atmos.*, 117, (D20), 2012.
- Nieradzki, L. P., *Four-Dimensional Variational Assimilation of Aerosol Data From In-Situ and Remote Sensing Platforms*, Ph.D. Thesis, Institut für Geophysik und Meteorologie der Universität zu Köln, 2011.
- Omar, A. H., D. M. Winker, C. Kittaka, M. A. Vaughan, Z. Liu, Y. Hu, C. R. Trepte, R. R. Rogers, R. A. Ferrare, K.-P. Lee, R. E. Kuehn and C. A. Hostetler, The CALIPSO automated aerosol classification and lidar ratio selection algorithm, *J. Atmos. Ocean. Technol.*, 26, (10), 1994–2014, 2009.
- Orlanski, I., A rational subdivision of scales for atmospheric processes, *Bull. Amer. Meteor. Soc.*, 56, 527–530, 1975.
- Oxford Economics, The economic impacts of air travel restrictions due to volcanic ash, *A report prepared for Airbus*, 2010.

- Pappalardo, G., L. Mona, G. D'Amico, U. Wandinger, M. Adam, A. Amodeo, A. Ansmann, A. Apituley, L. Alados Arboledas, D. Balis, A. Boselli, J. A. Bravo-Aranda, A. Chaikovsky, A. Comeron, J. Cuesta, F. De Tomasi, V. Freudenthaler, M. Gausa, E. Giannakaki, H. Giehl, A. Giunta, I. Grigorov, S. Groß, M. Haeffelin, A. Hiebsch, M. Iarlori, D. Lange, H. Linné, F. Madonna, I. Mattis, R.-E. Mamouri, M. A. P. McAuliffe, V. Mitev, F. Molero, F. Navas-Guzman, D. Nicolae, A. Papayannis, M. R. Perrone, C. Pietras, A. Pietruczuk, G. Pisani, J. Preißler, M. Pujadas, V. Rizi, A. A. Ruth, J. Schmidt, F. Schnell, P. Seifert, I. Serikov, M. Sicard, V. Simeonov, N. Spinelli, K. Stebel, M. Tesche, T. Trickl, X. Wang, F. Wagner, M. Wiegner and K. M. Wilson, Four-dimensional distribution of the 2010 Eyjafjallajökull volcanic cloud over Europe observed by EARLINET, *Atmos. Chem. Phys.*, *13*, (8), 4429–4450, 2013.
- Pavolonis, M. J., W. F. Feltz, A. K. Heidinger and G. M. Gallina, A daytime complement to the reverse absorption technique for improved automated detection of volcanic ash, *J. Atmos. Ocean. Technol.*, *23*, (11), 1422–1444, 2006.
- Pavolonis, M. J., A. K. Heidinger and J. Sieglaff, Automated retrievals of volcanic ash and dust cloud properties from upwelling infrared measurements, *J. Geophys. Res.: Atmos.*, *118*, (3), 1436–1458, 2013.
- Pesin, Y. B., Characteristic Lyapunov exponents and smooth ergodic theory, *Russ. Math. Surv.*, *32*, 55, 1977.
- Petersen, G. N., A short meteorological overview of the Eyjafjallajökull eruption 14 April–23 May 2010, *Weather*, *65*, (8), 203–207, 2010.
- Petzold, A., V. Thouret, C. Gerbig, A. Zahn, C. A. M. Brenninkmeijer, M. Gallagher, M. Hermann, M. Pontaud, H. Ziereis, D. Boulanger, J. Marshall, P. Nédélec, H. G. J. Smit, U. Friess, J.-M. Flaud, A. Wahner, J.-P. Cammas, A. Volz-Thomas and IAGOS TEAM, Global-scale atmosphere monitoring by in-service aircraft - current achievements and future prospects of the european research infrastructure IAGOS, *Tellus B*, *67*, (1), 28452, 2015.
- Picchiani, M., M. Chini, S. Corradini, L. Merucci, P. Sellitto, F. Del Frate and S. Stramondo, Volcanic ash detection and retrievals using MODIS data by means of neural networks, *Atmos. Meas. Tech.*, *4*, (12), 2619, 2011.
- Prata, A. J., Observations of volcanic ash clouds in the 10–12  $\mu\text{m}$  window using AVHRR/2 data, *Int. J. Remote. Sens.*, *10*, (4–5), 751–761, 1989.
- Prata, A. and C. Bernardo, Retrieval of volcanic ash particle size, mass and optical depth from a ground-based thermal infrared camera, *J. Volcanol. Geotherm. Res.*, *186*, (1), 91 – 107, 2009.
- Prata, A. J. and I. F. Grant, Retrieval of microphysical and morphological properties of volcanic ash plumes from satellite data: Application to Mt Ruapehu, New Zealand, *Q. J. Royal Meteorol. Soc.*, *127*, (576), 2153–2179, 2001.
- Prata, A. J. and J. Kerkmann, Simultaneous retrieval of volcanic ash and  $\text{SO}_2$  using MSG-SEVIRI measurements, *Geophys. Res. Lett.*, *34*, (5), 2007.

- Prata, A. J. and A. T. Prata**, Eyjafjallajökull volcanic ash concentrations determined using spin enhanced visible and infrared imager measurements, *J. Geophys. Res.: Atmos.*, *117*, (D20), 2012.
- Prata, F. and B. Rose**, Chapter 52 - Volcanic ash hazards to aviation, in *The Encyclopedia of Volcanoes (Second Edition)*, edited by H. Sigurdsson, 911 – 934, Academic Press, Amsterdam, second edition Auflage, 2015.
- Prospero, J. M.**, Long-term measurements of the transport of African mineral dust to the southeastern United States: Implications for regional air quality, *J. Geophys. Res.: Atmos.*, *104*, (D13), 15917–15927, 1999.
- Pöschl, U.**, Atmospheric aerosols: Composition, transformation, climate and health effects, *Angew. Chem. Int. Ed.*, *44*, (46), 7520–7540, 2005.
- Rabier, F., H. Järvinen, E. Klinker, J.-F. Mahfouf and A. Simmons**, The ECMWF operational implementation of four-dimensional variational assimilation. I: Experimental results with simplified physics, *Q. J. Royal Meteorol. Soc.*, *126*, (564), 1143–1170, 2000.
- Rio, C., F. Hourdin and A. Chédin**, Numerical simulation of tropospheric injection of biomass burning products by pyro-thermal plumes, *Atmos. Chem. Phys.*, *10*, (8), 3463–3478, 2010.
- Robock, A.**, Volcanic eruptions and climate, *Rev. Geophys.*, *38*, 191–219, 2000.
- Sandu, A.**, Targeted observations for atmospheric chemistry and transport models, in *Computational Science – ICCS 2006: 6th International Conference, Reading, UK, May 28-31, 2006, Proceedings, Part I*, edited by V. N. Alexandrov, G. D. van Albada, P. M. A. Sloot, and J. Dongarra, 712–719, Springer Berlin Heidelberg, Berlin, Heidelberg, 2006.
- Schmetz, J., P. Pili, S. Tjemkes, D. Just, J. Kerkmann, S. Rota and A. Ratier**, An Introduction to Meteosat Second Generation (MSG), *Bull. Amer. Meteor. Soc.*, *83*, (7), 977–992, 2002.
- Schmetz, J., Y. Govaerts, M. König, H.-J. Lutz, A. Ratier and S. Tjemkes**, A Short Introduction to Meteosat Second Generation (MSG), *CIRA, Colorado State Univ.: Fort Collins, CO, USA*, 2005.
- Schumann, U., B. Weinzierl, O. Reitebuch, H. Schlager, A. Minikin, C. Forster, R. Baumann, T. Sailer, k. Graf, H. Mannstein, C. Voigt, S. Rahm, R. Simmet, M. Scheibe, M. Lichtenstern, P. Stock, H. Rüba, D. Schäuble, A. Tafferner, M. Rautenhaus, T. Gerz, H. Ziereis, M. Krautstrunk, C. Mallaun, J.-F. Gayet, K. Lieke, K. Kandler, M. Ebert, S. Weinbruch, A. Stohl, J. Gasteiger, S. Gross, V. Freudenthaler, M. Wiegner, A. Ansmann, A. Tesche, H. Olafsson and K. Sturm**, Airborne observations of the Eyjafjalla volcano ash cloud over Europe during air space closure in April and May 2010, *Atmos. Chem. Phys.*, *11*, 2245–2279, 2011.
- Senf, F., F. Dietzsch, A. Hünerbein and H. Deneke**, Characterization of initiation and growth of selected severe convective storms over central Europe with MSG-SEVIRI, *J. Appl. Meteor. Climatol.*, *54*, (1), 207–224, 2015.

- Shao, Y., K.-H. Wyrwoll, A. Chappell, J. Huang, Z. Lin, G. H. McTainsh, M. Mikami, T. Y. Tanaka, X. Wang and S. Yoon, Dust cycle: An emerging core theme in earth system science, *Aeolian Res.*, 2, (4), 181 – 204, 2011.
- Shiraiwa, M., K. Selzle and U. Pöschl, Hazardous components and health effects of atmospheric aerosol particles: reactive oxygen species, soot, polycyclic aromatic compounds and allergenic proteins, *Free Radic. Res.*, 46, (8), 927–939, 2012.
- Sigmundsson, F., S. Hreinsdóttir, A. Hooper, T. Árnadóttir, R. Pedersen, M. J. Roberts, N. Óskarsson, A. Auriac, J. Decriem, P. Einarsson et al., Intrusion triggering of the 2010 Eyjafjallajökull explosive eruption, *Nature*, 468, (7322), 426–430, 2010.
- Skamarock, W. C., J. B. Klemp, J. Dudhia, D. O. Gill, D. M. Barker, M. G. Duda, X.-Y. Huang, W. Wang and J. G. Powers, A description of the advanced research WRF version 3. NCAR Tech, technical report, Note NCAR/TN-4751STR, 2008.
- Snyder, C., T. Bengtsson, P. Bickel and J. Anderson, Obstacles to high-dimensional particle filtering, *Month. Weath. Rev.*, 136, (12), 4629–4640, 2008.
- Sokolik, I. N. and O. B. Toon, Incorporation of mineralogical composition into models of the radiative properties of mineral aerosol from uv to ir wavelengths, *J. Geophys. Res.: Atmos.*, 104, (D8), 9423–9444, 1999.
- Sommer, M. and M. Weissmann, Ensemble-based approximation of observation impact using an observation-based verification metric, *Tellus A*, 68, (1), 27885, 2016.
- Steensen, B. M., A. Kylling, N. I. Kristiansen and M. Schulz, Uncertainty assessment and applicability of an inversion method for volcanic ash forecasting, *Atmos. Chem. Phys.*, 17, (14), 9205–9222, 2017.
- Stephens, G. L., D. G. Vane, R. J. Boain, G. G. Mace, K. Sassen, Z. Wang, A. J. Illingworth, E. J. O’Connor, W. B. Rossow, S. L. Durden, S. D. Miller, R. T. Austin, A. Benedetti, C. Mitrescu and T. C. S. Team, The CloudSat mission and the A-Train, *Bull. Amer. Meteor. Soc.*, 83, (12), 1771–1790, 2002.
- Stohl, A., A. J. Prata, S. Eckhardt, L. Clarisse, A. Durant, S. Henne, N. I. Kristiansen, A. Minikin, U. Schumann, P. Seibert, K. Stebel, H. E. Thomas, T. Thorsteinsson, K. Tørseth and B. Weinzierl, Determination of time- and height-resolved volcanic ash emissions and their use for quantitative ash dispersion modeling: the 2010 Eyjafjallajökull eruption, *Atmos. Chem. Phys.*, 11, (9), 4333–4351, 2011.
- Strunk, A., *Tropospheric Chemical State Estimation by Four-Dimensional Variational Data Assimilation on Nested Grids*, Ph.D. Thesis, Institut für Geophysik und Meteorologie der Universität zu Köln, 2006.
- Suzuki, T. et al., A theoretical model for dispersion of tephra, in *Arc volcanism: physics and tectonics*, vol 95, 113, Terra Scientific Publishing Company (TERRAPUB), 1983.

- Szunyogh, I., Z. Toth, A. V. Zimin, S. J. Majumdar and A. Persson**, Propagation of the effect of targeted observations: The 2000 Winter Storm Reconnaissance Program, *Month. Weath. Rev.*, *130*, (5), 1144–1165, 2002.
- Talagrand, O.**, Assimilation of observations, an introduction, *J. Meteor. Soc. Japan*, *75*, (1B), 191–209, 1997.
- Tegen, I. and I. Fung**, Modeling of mineral dust in the atmosphere: Sources, transport, and optical thickness, *J. Geophys. Res.: Atmos.*, *99*, (D11), 22897–22914, 1994.
- Thomas, H. E. and A. J. Prata**, Sulphur dioxide as a volcanic ash proxy during the April–May 2010 eruption of Eyjafjallajökull volcano, Iceland, *Atmos. Chem. Phys.*, *11*, (14), 6871–6880, 2011.
- Thomas, H. E. and I. M. Watson**, Observations of volcanic emissions from space: current and future perspectives, *Natural Hazards*, *54*, (2), 323–354, 2010.
- Thordarson, T. and S. Self**, Atmospheric and environmental effects of the 1783–1784 laki eruption: A review and reassessment, *J. Geophys. Res.: Atmos.*, *108*, (D1), AAC 7–1–AAC 7–29, 2003.
- Toth, Z. and E. Kalnay**, Ensemble forecasting at nmc: The generation of perturbations, *Bull. Amer. Meteor. Soc.*, *74*, (12), 2317–2330, 1993.
- Tracton, M. S. and E. Kalnay**, Operational ensemble prediction at the national meteorological center: Practical aspects, *Weather Forecast.*, *8*, (3), 379–398, 1993.
- van Leeuwen, P. J.**, Particle filtering in geophysical systems, *Month. Weath. Rev.*, *137*, (12), 4089–4114, 2009.
- van Leeuwen, P. J.**, *Nonlinear Data Assimilation for high-dimensional systems*, 1–73, Springer International Publishing, Cham, 2015.
- Vaughan, M. A., K. A. Powell, D. M. Winker, C. A. Hostetler, R. E. Kuehn, W. H. Hunt, B. J. Getzewich, S. A. Young, Z. Liu and M. J. McGill**, Fully automated detection of cloud and aerosol layers in the CALIPSO lidar measurements, *J. Atmos. Ocean. Technol.*, *26*, (10), 2034–2050, 2009.
- Walcek, C. J.**, Minor flux adjustment near mixing ratio extremes for simplified yet highly accurate monotonic calculation of tracer advection, *J. Geophys. Res.: Atmos.*, *105*, (D7), 9335–9348, 2000.
- Wang, K.-Y., D. J. Lary, D. E. Shallcross, S. M. Hall and J. A. Pyle**, A review on the use of the adjoint method in four-dimensional atmospheric-chemistry data assimilation, *Q. J. Royal Meteorol. Soc.*, *127*, (576), 2181–2204, 2001.
- Weaver, A. and P. Courtier**, Correlation modelling on the sphere using a generalized diffusion equation, *Q. J. Royal Meteorol. Soc.*, *127*, 1815–1846, 2001.
- Webley, P., B. Stunder and K. Dean**, Preliminary sensitivity study of eruption source parameters for operational volcanic ash cloud transport and dispersion models – A case study of the August 1992 eruption of the Crater Peak vent, Mount Spurr, Alaska, *J. Volcanol. Geotherm. Res.*, *186*, (1), 108 – 119, 2009.

- Webley, P. W., T. Steensen, M. Stuefer, G. Grell, S. Freitas and M. Pavolonis**, Analyzing the Eyjafjallajökull 2010 eruption using satellite remote sensing, lidar and WRF-Chem dispersion and tracking model, *J. Geophys. Res.: Atmos.*, *117*, (D20), 2012.
- Webster, H. N., D. J. Thomson, B. T. Johnson, I. P. C. Heard, K. Turnbull, F. Marenco, N. I. Kristiansen, J. Dorsey, A. Minikin, B. Weinzierl, U. Schumann, R. S. J. Sparks, S. C. Loughlin, M. C. Hort, S. J. Leadbetter, B. J. Devenish, A. J. Manning, C. S. Witham, J. M. Haywood and B. W. Golding**, Operational prediction of ash concentrations in the distal volcanic cloud from the 2010 Eyjafjallajökull eruption, *J. Geophys. Res.: Atmos.*, *117*, (D20), 2012.
- Wen, S. and W. I. Rose**, Retrieval of sizes and total masses of particles in volcanic clouds using AVHRR bands 4 and 5, *J. Geophys. Res.: Atmos.*, *99*, (D3), 5421–5431, 1994.
- Wilkins, K. L., S. Mackie, M. Watson, H. Webster, D. Thomson and H. Dacre**, Data insertion in volcanic ash cloud forecasting, *Ann. Geophys.*, *57*, (0), 2014.
- Wilkins, K. L., A. Benedetti, N. I. Kristiansen and A. C. Lange**, Chapter 13 – Applications of satellite observations of volcanic ash in atmospheric dispersion modeling, in *Volcanic Ash*, edited by S. Mackie, K. Cashman, H. Ricketts, A. Rust, and M. Watson, 233 – 246, Elsevier, 2016a.
- Wilkins, K. L., I. M. Watson, N. I. Kristiansen, H. N. Webster, D. J. Thomson, H. F. Dacre and A. J. Prata**, Using data insertion with the NAME model to simulate the 8 May 2010 Eyjafjallajökull volcanic ash cloud, *J. Geophys. Res.: Atmos.*, *121*, (1), 306–323, 2016b.
- Wilkins, K., L. Western and I. Watson**, Simulating atmospheric transport of the 2011 Grímsvötn ash cloud using a data insertion update scheme, *Atmos. Environ.*, *141*, (Supplement C), 48 – 59, 2016c.
- Winiarek, V., M. Bocquet, O. Saunier and A. Mathieu**, Estimation of errors in the inverse modeling of accidental release of atmospheric pollutant: Application to the reconstruction of the cesium-137 and iodine-131 source terms from the Fukushima Daiichi power plant, *J. Geophys. Res.: Atmos.*, *117*, (D5), 2012.
- Winker, D. M., J. Pelon and M. P. McCormick**, The CALIPSO mission: Spaceborne lidar for observation of aerosols and clouds, in *Proc. Spie*, vol 4893, 11, 2003.
- Winker, D. M., W. H. Hunt and M. J. McGill**, Initial performance assessment of CALIOP, *Geophys. Res. Lett.*, *34*, (19), 2007.
- Winker, D. M., M. A. Vaughan, A. Omar, Y. Hu, K. A. Powell, Z. Liu, W. H. Hunt and S. A. Young**, Overview of the CALIPSO mission and CALIOP data processing algorithms, *J. Atmos. Ocean. Technol.*, *26*, (11), 2310–2323, 2009.
- Winker, D. M., Z. Liu, A. Omar, J. Tackett and D. Fairlie**, CALIOP observations of the transport of ash from the Eyjafjallajökull volcano in April 2010, *J. Geophys. Res.*, *117*, 2012.

- Woodhouse, M. J., A. J. Hogg, J. C. Phillips and R. S. J. Sparks**, Interaction between volcanic plumes and wind during the 2010 Eyjafjallajökull eruption, Iceland, *J. Geophys. Res.: Sol. Earth*, *118*, (1), 92–109, 2013.
- Wu, X., B. Jacob and H. Elbern**, Optimal control and observation locations for time-varying systems on a finite-time horizon, *SIAM J. Control Optim.*, *54*, (1), 291–316, 2016.
- Wu, X., H. Elbern and B. Jacob**, The degree of freedom for signal assessment of measurement networks for joint chemical state and emission analysis, *Geosci. Model Dev.*, *2017*, 1–29, 2017.
- Xun-Gui, L., W. Xia and H. Qiang**, Comprehensive entropy weight observability-controllability risk analysis and its application to water resource decision-making, *Water SA*, *38*, (4), 573–580, 2012.
- Young, S. A.**, Analysis of lidar backscatter profiles in optically thin clouds, *Appl. Opt.*, *34*, (30), 7019–7031, 1995.
- Young, S. A. and M. A. Vaughan**, The retrieval of profiles of particulate extinction from Cloud-Aerosol Lidar Infrared Pathfinder Satellite Observations (CALIPSO) data: Algorithm description, *J. Atmos. Ocean. Technol.*, *26*, (6), 1105–1119, 2009.
- Yu, T., W. I. Rose and A. J. Prata**, Atmospheric correction for satellite-based volcanic ash mapping and retrievals using "split window" IR data from GOES and AVHRR, *J. Geophys. Res.: Atmos.*, *107*, (D16), AAC 10–1–AAC 10–19, 2002.
- Zehner, C.**, Monitoring volcanic ash from space, in *Proceedings of the ESA-EUMET-SAT workshop on the 14 April to 23 May 2010 eruption at the Eyjafjöll volcano, South Iceland. Frascati, Italy, 26–27 May 2010*, 2010.



# Personal Acknowledgments

First of all, I would like to particularly thank my adviser PD Dr. Hendrik Elbern, who gave me the opportunity to work on this thesis with a topic that extensively coincided with my personal scientific interest. He supported me with productive discussions and ideas that I could always request due to his "open door" strategy. During the full course of this work, I very much profited from his exceptional knowledge and his steady scientific encouragement.

I am also grateful to Prof. Dr. Yaping Shao for his particular interest in my thesis, for his acceptance to act as referee, and for the evaluation of the results of this work. For the funding of this work and for multiple supports I would gratefully acknowledge the Institute for Energy and Climate Research – Troposphere (IEK-8) at Forschungszentrum Jülich, notably Prof. Dr. Andreas Wahner and Prof. Dr. Astrid Kiendler-Scharr. Being given the opportunity to experience a research stay in Norway, was most beneficial for my work and my professional career.

Further, I appreciate the financial support of the graduate schools HITEC (Helmholtz Interdisciplinary Doctoral Training in Energy and Climate Research of Forschungszentrum Jülich) and GSGS (Graduate School of Geoscience of University of Cologne), who enabled my participation at instructive summer schools.

I kindly thank my external mentor Dr. Fred Prata, who cleared the way for me to visit the Norsk Institutt for Luftforskning (NILU) and Nicarnica Aviation AS in Kjeller, Norway, and to work there as a guest scientist. I learned a lot about infrared imaging and volcanic ash hazards to aviation thanks to some fruitful discussions.

I am very grateful to the ATMOS (Department of Atmosphere and Climate) research group at NILU for welcoming me as temporary part of this team. I enjoyed this experience a lot. Likewise, I acknowledge the respective colleagues of Nicarnica Aviation.

I want to express my thanks to Dr. Angela Benedetti and Dr. Holger Baars for efficient cooperation beyond the ACTRIS-2 project.

Philipp Franke deserves my appreciation for many years of exceptional collaboration. Thanks for all discussions, for always paying attention to my questions, and for the great support.

In the last months my colleague Jonas Berndt shared the same final phase of PhD studies. In many hours in the institute, he was always supportive for short discussions, arranging ideas, and finding optimized formulations. Many thanks!

Dr. Elmar Friese, who knows the EURAD-IM like barely someone else, helped with

his profound modeling knowledge in many cases. Regarding computer technical problems at the Rhenish Institute for Environmental Research (RIU), Georg Piekorz was always supportive to find a quick solution. To both I would like to express my gratitude.

Dr. Luise Fröhlich, Tamari Janelidze, and Paraskevi Vourlioti assisted among other things by proofreading this thesis. Working in the same office, Dr. Isabel Ribeiro and Dr. Johannes Klimpt, both were open for exchanging knowledge. Many thanks to all these personalities and likewise to all other present and former colleagues, which could not be specifically mentioned here, for the great time together.

Thanks a million to Dr. Rebecca Jayne Thorne for passing the written thesis through a final English revision and for all your motivating words.

At the end, a very special appreciation is donated to my family. Many thanks to my siblings Cathrin and Timo for always believing in me and my skills. I am deeply grateful to my dear parents Ute and Joachim for their love, all encouragements, their endless care and support. Thank you so much!

# Erklärung

Ich versichere, dass ich die von mir vorgelegte Dissertation selbständig angefertigt, die benutzten Quellen und Hilfsmittel vollständig angegeben und die Stellen der Arbeit – einschließlich Tabellen, Karten und Abbildungen –, die anderen Werken im Wortlaut oder dem Sinn nach entnommen sind, in jedem Einzelfall als Entlehnung kenntlich gemacht habe; dass diese Dissertation noch keiner anderen Fakultät oder Universität zur Prüfung vorgelegen hat; dass sie – abgesehen von unten angegebenen Teilpublikationen – noch nicht veröffentlicht worden ist, sowie, dass ich eine solche Veröffentlichung vor Abschluss des Promotionsverfahrens nicht vornehmen werde. Die Bestimmungen der Promotionsordnung sind mir bekannt. Die von mir vorgelegte Dissertation ist von PD Dr. Hendrik Elbern betreut worden.

## **Teilpublikation:**

Wilkins, K. L., Benedetti, A., Kristiansen, N. I. und Lange, A. C. (2016). Chapter 13 – Applications of satellite observations of volcanic ash in atmospheric dispersion modeling. In S. Mackie, K. Cashman, H. Ricketts, A. Rust, und M. Watson (Hrsg.), *Volcanic Ash* (233 – 246), Elsevier.

---

Datum, Anne Caroline Lange

